
Both *pztc* and *pzfc* provide different information of the Pt(hkl)|solution interface but with the same fundamental relevance.

The *pztc* of platinum single crystal electrodes can be approached by using the CO displacement technique, technique which was implemented in this research group. In turn, the *pzfc* can be estimated by using *laser induced temperature jump technique or laser induced potential transient (LIPT)*. This technique applies short laser pulses that cause the sudden increase of the interfacial temperature. The technique measures the time scale change of the potential electrode caused by this thermal perturbation under coulstatic conditions. The change of the electrode potential is mainly related with solvent network structuration or orientation along the electric field on surface. Therefore, the response towards the laser perturbation can be considered to be dependent of the free charge on the surface. In the situation of maximum disorder in the solvent network, the potential of maximum entropy (*pme*) of double layer formation is reached, value which is closely related with the *pzfc*.

So, the laser technique was employed to study M(hkl)|[Emmim][Tf₂N]. However, before investigating the M(hkl)|[Emmim][Tf₂N], work was carried in Pt(111) and Ir(111) in contact with more familiar aqueous electrolytes: HClO₄/KClO₄ solutions and NaF/HClO₄ buffer solutions. These last buffer solutions allowed studying at pH values near the neutrality (pH from 3 to 6). In spite of the chemical and physical similitudes that Pt(111) and Ir(111) share, the laser technique demonstrated that, actually, their interfacial properties change with pH in a very different way and results cannot be understood without considering the solvent influence.

With these results in mind, the laser technique was employed to interrogate the Pt(111)|[Emmim][Tf₂N] and Au(hkl)|[Emmim][Tf₂N] interfaces. These experiments were performed in order to get more insight about double layer restructuring in ILs media and its dependence with both surface material and orientation. Later, Au(hkl)|DES interface was evaluated with cyclic voltammetry. LIPT experiments for Au(hkl)|DES was not included due to the laser response was mainly dominated by the excess of chloride in DES.

In addition to the study of Au(hkl)|DES interface, the Cu deposition process was investigated, paying special attention on the first steps, that involves underpotential deposition (UPD). Later, mechanistic studies of the electrodeposition of copper and silver

on glassy carbon were performed in the DES and, taking advantage from the fact that DES contains around 5M of chloride, the results were compared to those obtained in aqueous electrolytes, with and without chloride excess as complexing agent. The goal of this research was to understand the way that the DES species affect the metal deposition mechanism, paying special attention to chloride which stabilizes the metal precursor by complex formation. Here, these two metals are models to investigate the nucleation and growth deposition mechanism when the whole process involves one charge transfer (in case of Ag(I) and Cu(I) deposition) or two (for Cu(II)). For this study, a glassy carbon electrode substrate was conveniently used because the low metal-substrate interaction allows the analysis of nucleation processes.

Finally, the applicability of the above-mentioned ILs to modify high active surfaces, such as Pt with Ni (a metal that is hardly deposited in aqueous electrolytes), was investigated. The motivation of this study lays on the increasing necessity to design new catalysts that incorporate abundant and cheap materials in detriment of Pt, but with the same good catalytic properties of the Pt. In particular, this part focuses more on investigating the viability of the DES to modify a Pt surface electrode with Ni, and the surface sensitivity of Ni deposition in DES. Previously, a strategy to pre-treat and ensure surface ordering on Pt(111) was investigated. For that, the use of CO adsorbed on Pt(111) as protective layer was proposed to allow investigating Pt(111)|IL interface.

1.2) Publications and chapter distribution

According to abovementioned sections, the present thesis was organized in order to fulfil the proposed objectives.

At first, the interfacial properties of the Electrode|IL interface were investigated using well-oriented surfaces, i.e, single crystal electrodes M(hkl) on two different ILs:

- 1) A Room Temperature Ionic Liquid (RTIL): [Emmim][Tf₂N].
- 2) A Deep Eutectic Solvent (DES): the choline chloride/urea mixture, 1ChCl:2urea molar ratio.

The *laser induced temperature jump technique* (LIPT) was employed to obtain information related to the double layer structure. Pt(hkl) and Au(hkl) surfaces were used as models of non-polarizable and polarizable surfaces respectively. Finally, the

Au(hkl)|DES was investigated. To deep inside into this topic, the following works were performed:

- Study of the interfacial properties of both Pt(111) and Ir(111) in contact with aqueous electrolytes at different pH by LIPT.
- Study of Pt(111) interfacial properties with the [Emmim][Tf₂N] by LIPT.
- Study of the Au(hkl)|[Emmim][Tf₂N] interface by LIPT.
- Study of the Au(hkl)|DES interface by cyclic voltammetry.

1. Group of publications (chapters):

WORK A (chapter 4, section 4.1): Study of the Pt(111)|electrolyte interface in the region close to neutral pH solutions by the laser induced temperature jump technique. *Electrochimica Acta* **2017**, 228, 667-676.

WORK B (chapter 4, section 4.2): On the pH Dependence of the Potential of Maximum Entropy of Ir(111) Electrodes. *Scientific Reports* **2017**, 7 (1), 1246.

WORK C (chapter 4, section 4.3): Study of the interface Pt(111)|[Emmim][NTf₂] using laser-induced temperature jump experiments. *Electrochemistry Communications* **2015**, 55, 39-42.

WORK D (chapter 4, section 4.4): Characterization of the interfaces between Au(hkl) single crystal basal plane electrodes and [Emmim][Tf₂N] ionic liquid. *Electrochemistry Communications* **2016**, 62, 44-47.

WORK E (chapter 4, section 4.5): Copper underpotential deposition at gold surfaces in contact with a deep eutectic solvent: New insights. *Electrochemistry Communications* **2017**, 78, 51-55.

The second part of the thesis focuses on the study of the electrodeposition of Ag and Cu on glassy carbon (GC) using DES as solvent to elucidate the nucleation and growth mechanisms. The weak interaction between glassy carbon and the deposited metal, jointly with the stabilization of the ions in solution by chloride complexation was considered useful to understand the nucleation and growth processes. Previously, copper underpotential deposition on Au(hkl) was studied in DES, to compare the particular features of metal deposition on a metallic substrate (Au):

- Study of copper electrodeposition in DES on Au(hkl).
- Mechanistic study of copper electrodeposition in DES on GC.
- Mechanistic study of the silver electrodeposition in DES on GC.

2. Group of publications (chapters):

WORK F (chapter 4, section 4.6): *Copper electrodeposition in a deep eutectic solvent. First stages analysis considering Cu(I) stabilization in chloride.* *Electrochimica Acta* **2014**, 123, 285-295.

WORK G (chapter 4, section 4.7): *Advances in Copper Electrodeposition in Chloride Excess. A Theoretical and Experimental Approach.* *Electrochimica Acta* **2015**, 164, 187-195.

WORK H (chapter 4, section 4.8): *Three-dimensional nucleation with diffusion controlled growth: A comparative study of electrochemical phase formation from aqueous and deep eutectic solvents.* *Journal of Electroanalytical Chemistry* **2017**, 793, 119-125.

Next, the electrodeposition of inert metal on an electrocatalytic metal substrate using both [Emmim][Tf₂N] and DES were studied.

- Ni electrodeposition on Pt(111) in [Emmim][Tf₂N].
- Ni electrodeposition on GC and Pt(poly) in DES.
- Ni electrodeposition on Pt(111) in DES.

These works are proposed in order to obtain new routes that allow modifying a catalyst metal with different Ni structures. The purpose of these works is to evaluate the applicability of these two novel solvents to modify a high catalytic surface such as Pt with Ni, investigating the surface sensitivity of the process.

3. Group of publications (chapters):

WORK I (chapter 5, other results): *The use of CO as cleaning tool of highly active surfaces in contact with ionic liquids. Ni deposition on Pt(111) surfaces in IL media.* Submitted.

WORK J (chapter 4, section 4.9): *Surface Sensitive Nickel Deposition in Deep Eutectic Solvent.* ACS Applied Energy Materials **2018**, 1, 1016-1028.

1.3) REFERENCES

- (1) Frank Endres, D. M. A. A., *Electrodeposition from ionic liquids.*Wiley 2008



Universitat d'Alacant
Universidad de Alicante

Chapter 2

State of the art

Universitat d'Alacant
Universidad de Alicante

STATE OF THE ART

This chapter is a brief review of the main research performed in the ionic liquid field through last years related to the scope of this thesis.

2.1) Ionic liquids. Definition and classification

The use of ionic liquids (ILs) as solvents has attracted considerably the attention of the electrochemical community during the past three decades. Their particular nature makes them promising solvents in Electrochemistry¹. Since the discovery of the ethylammonium nitrate (EAN) by Walden in 1914², a pure salt that was liquid at room temperature, the number of publications related with ionic liquids has experienced an exponential increase (Figure 2.1)³. Especially, from 2000 until nowadays, thousands of articles (>50.000 papers in total) have been published in this topic³, thus evidencing the high interest in the ionic liquid science field. The research in ionic liquids covers a large variety of important topics. Some of them are more focused on their potential applications: especially in organic synthesis⁴ and electrochemistry⁵⁻⁷. Other studies focus on more fundamental aspects and try to understand their structure and describe both their chemical and physical properties⁸⁻¹⁰. Their intrinsic conductivity and good thermal stability besides their relative ease incorporation in different systems explain why these novel solvents are presented as feasible alternative for many purposes, becoming part of interdisciplinary research area.

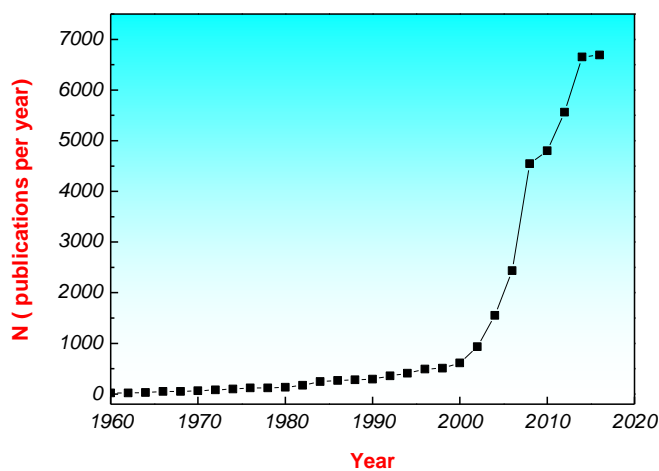


Figure 2.1: Relation of the papers published per year in the field of ILs, since 1960. Graph adapted from Scopus data base.

The definition of an ionic liquid (IL) was firstly coined from Walden's work published in 1914². However, it is important to mention that before Walden reported the synthesis of EAN, an organic solution consisting on ethanol-ammonium nitrate with a $T_m < 53^\circ\text{C}$ was reported by Gabriel and Weiner in 1888¹¹. According to Walden's work, an ionic liquid was referred to compounds formed entirely by its ions and fluid at $T_m < 100^\circ\text{C}$. The definition of an IL was arbitrarily adopted in order to differentiate them from molten salts¹². On the other hand, some authors have preferred to differentiate room temperature ionic liquids (RTILs) from the rest of ILs because the former are already liquid at temperatures lower than 25°C ⁹. This definition is inaccurate because only considers one physical property, the melting point. The fact that most of the ILs are liquids at room temperature is attributed to their structure^{9,13}. There are many possibilities to combine anions and cations but any specific rule to do it, the cation is normally a non-symmetric organic ion with a large size and the positive charge non-uniformly distributed but well stabilized, whereas the anion can be an inorganic or organic anion with variable size and symmetry⁹. The properties of the ionic liquids such as the melting point, viscosity or conductivity will be determined by the different interactions between the ions¹³. In conclusion, many factors must be taken into account to understand the nature of ionic liquids. Despite the high number of ILs reported in the literature, ionic liquids are usually classified in several generations, which have emerged over the years in order to cover the needs that have been appearing.

In the 50s a group of RTILs composed by mixtures of pyridinium halide salts with aluminum chloride (III) were discovered¹⁴. Later, during 80s, Wilkens and Hussey used alkylimidazolium halogenoaluminates¹⁵. Compared with the former ones, these new RTILs based on the imidazolium cation showed better electrochemical stability (in terms of the reduction of the cation). These room temperature ionic liquids consisting on the eutectic mixture between a Lewis acid (AlCl_3) and an organic salt [cation]X formed the first generation of reported RTILs. However, these RTILs were still outside the focus of interest because they showed several inconveniences to handle: the difficulty to control acidity/basicity and their non-stability to the air and water (due to the imminent formation of aluminum oxides) caused that these RTILs were soon replaced by the second generation of ionic liquids¹⁶.

The second generation of RTILs involved ionic liquids composed solely by ions unlike the eutectic mixtures from the first generation, and was discovered around 90s.

Wilkes and Zaworoko were working with alkyylimidazolium salts when they found that a room temperature ionic liquid could be synthesized by replacing chloro-aluminates salts by discrete anions such as tetrafluoroborate ($[\text{BF}_4]^-$) or acetate anions ($[\text{CH}_3\text{COO}]^-$)¹⁷. With them, the second generation of ionic liquids had been born and then ILs had been started to attract the attention in the field of the Electrochemistry (Figure 2.1). Although these ionic liquids had better stability in air and water than the former ones, they still showed high moisture sensitivity, especially those that contained hydrophilic anions such as: $[\text{BF}_4]^-$, methanesulfonate ($[\text{MeSO}_3]^-$), nitrate $[\text{NO}_3]^-$... being capable to adsorb high amounts of water ($>10.000\text{ppm}$)^{13, 18}. Other anions like $[\text{PF}_6]^-$, classified as hydrophobic, showed slight instability under certain conditions, producing little amounts of compounds like PO_4^{3-} or even the hazardous HF^5 . By using more hydrophobic and less reactive anions such as bis(trifluoromethylsulfonyl)imide, $[\text{Tf}_2\text{N}]^-$ the stability of the RTIL towards moisture was improved slightly¹⁹. Spite the improvement achieved with these RTILs in terms of stability, they were still hygroscopic²⁰. And it is relatively difficult to prevent RTIL from hydration without the use of inert atmosphere. In this context, more robust RTILs based on quaternary phosphonium, nitrogen or sulfur salts have been synthesized, broadening the spectrum of RTILs²¹⁻²³.

Other benefits of this new generation of ILs is that the synthesis was optimized in terms of time and costs in comparison with the previous ones ($\text{AlCl}_3 + [\text{cation}]\text{Cl}$). However, the synthesis is still expensive and introduced low amounts of contaminants, mainly halides and organic molecules^{4, 24-26}. High pure RTILs are too expensive, limiting their application for practical purposes. Table 2.1 summarizes the most common cations and anions employed in RTILs^{3, 23, 25}.

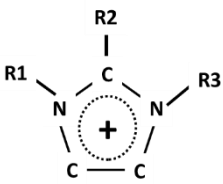
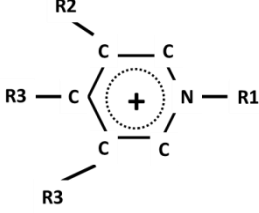
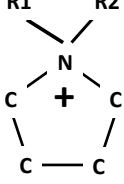
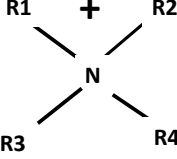
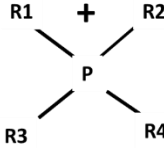
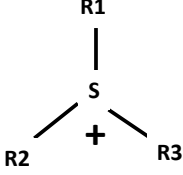
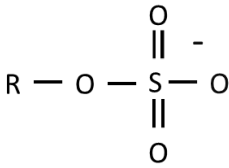
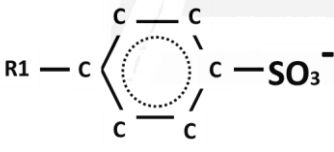
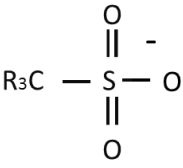
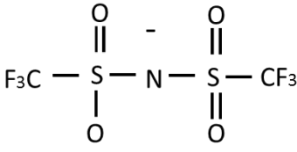
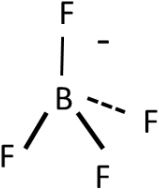
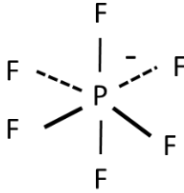
CATION		
		
Imidazolium	Pyridinium	Pyrrolidinium
		
Ammonium	Phosponium	Sulfonium
ORGANIC ANION		
		
Alkyl sulfate	Tosylate	Methanesulfonate
INORGANIC ANION		
		
Bis(trifluoromethylsulfonyl)imide	Tetrafluoroborate	Hexafluoro- phosphate
		[Cl-] [Br-] Halides [X-]

Table 2.1: Molecular structures of some of the cations and anions employed in RTILs. Rx represents an organic functional group.

Literature also provides other classifications of ILs focused on their structure characteristics^{9, 27}. The structure of RTILs is not straightforward. The cation usually contains several functional groups with variable polarity which modify the ion-ion interactions and change the properties of the IL. The ILs could show the ability to dissolve both polar and non-polar molecules as long as they contain molecular structures with several functionalities, showing this amphiphilic behavior. Regarding to structure, the most general classification of RTILs divides them in two groups: Protic ionic liquids (PILs) and aprotic ionic liquids (AILs)⁹:

- Protic ionic liquids (PILs) are formed by mixing a Brønsted acid and a Brønsted base (normally an amine) in the 1:1 molar ratio. The proton transfer leads the formation of the ionic species and, sometimes, a small fraction of neutral species as a result of chemical equilibrium. This fraction is usually negligible and thus PILs are considered as ILs formed by discrete ions. PILs show proton bond donor behavior. The ability to supply protons explains their different catalytic role and also different mass transport properties. Compared with aprotic ionic liquids, PILs are more unstable electrochemically and usually displays shorter electrochemical windows²⁷.
- Aprotic ionic liquids (AILs) involve the rest of ionic liquids and they can be bond proton donor or not. AILs can show many different structures. Their synthesis is much more complex and expensive than PILs synthesis. However, they usually show better thermal and electrochemical stability than PILs⁹.

2.2) Properties of the RTILs

RTILs have a set of properties not observed in other solvents. Among these properties, people usually point out their extremely high viscosity (30-600 mPas), being at least two or even three orders of magnitude more viscous than traditional organic solvents and aqueous electrolytes⁵. But, contrary to organic solvents, they have enough conductivity without the need to add any inorganic salt. Moreover, RTILs show low vapor pressure as well as high thermal stability. Another remarkable benefit from RTILs is their wide electrochemical window (3-5V), i.e, they show high electrochemical stability^{23, 25}. These properties are very variable considering the broad spectrum of RTILs.

How these properties vary from one RTIL to another could be sometimes rationalized in terms of ion-ion interactions^{13, 28, 29}.

The complex structures of the cation and the anion introduce several non-covalent interactions that compete with the coulombic forces. These non-covalent interactions are mainly van der Waals and hydrogen bond formation. Van der Waals interactions increase by increasing the length of the alkyl chains located on the functional groups²⁹⁻³⁰. The increase of the alkyl chain length affects the viscosity of the RTILs, the longer the alkyl chain of the cation higher viscosity of the RTIL is. Table 2.2 contains the viscosity of four RTILs based on the 1,3-dialkyl imidazolium cation.

RTIL	Number of C in R ₃	Viscosity [mPas]
[Emim][Tf ₂ N]	2	≈30
[Bmim][Tf ₂ N]	4	≈45
[C ₆ mim][Tf ₂ N]	6	≈60
[C ₈ mim][Tf ₂ N]	8	≈75

Table 2.2: Viscosities of several [Rmim][Tf₂N]. R = -CH₃^{5,30}.

The increase of the length of the alkyl chain also affects the melting point of the RTILs, but in a different way than the viscosity¹⁰. By increasing the number of carbons, the melting point decreases until it plateaus at a specific length (C=4-9). Afterwards, by increasing the number of carbons, the melting point also rises⁹. The lesser symmetry in the cation allows lowering the melting point but, finally, the increase of the van der Waals interactions has a dominant effect and changes the trend.

Hydrogen bonds also play a determinant role in the structure of the solvent network and influence the properties of the RTILs. Hydrogen bonds are mainly present in RTILs that have fluorine-containing anions ([BF₄]⁻), ([PF₆]⁻), ([Tf₂N]⁻) or oxygen containing anions ([CH₃COO]⁻, [TfO]⁻). RTILs that have halides anions (Cl⁻, Br⁻ or I⁻)

also can form weak hydrogen bonds³¹. For cations based on the imidazolium ring, hydrogen bonds are formed between the groups $-\text{CH}$ of the ring and the fluorine or oxygen atoms from the anion: $\text{C}-\text{H}\cdots\text{F}$, $\text{C}-\text{H}\cdots\text{O}$, as detected by X-Ray studies, NMR and Neutron diffraction^{18, 32-34}. In particular, the proton located at the position C2 in the imidazolium ring (Figure 2.2) has a strong participation in the hydrogen bond formation. The methylation of C2 decreases the hydrogen bond interactions, reinforcing the coulombic interactions between the ionic species in the RTILs, fact that influences both the physical and chemical properties. For instance, the methylation of C2 in the [Emmim][Tf₂N] increases dramatically the melting point and the viscosity compared with its protonated homologous: [Emim][Tf₂N], as seen in Table 2.3^{13, 34}.

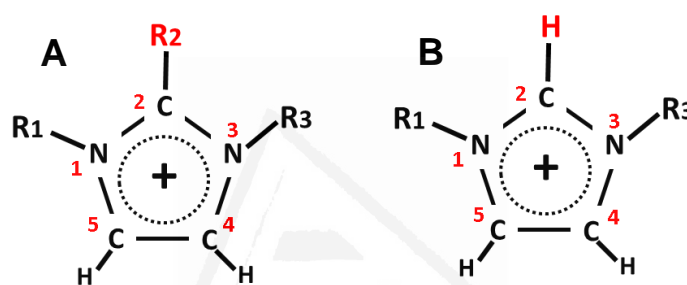


Figure 2.2: Scheme of the imidazolium ring. A) The position C2 is functionalized.

A) The position C2 contains the acid proton.

RTIL	Melting point	Viscosity
[Emim][Tf ₂ N]	-3°C	34 mPas
[Emmim][Tf ₂ N]	20°C	88 mPas

Table 2.3: Data of the melting point and viscosities values for [Emmim][Tf₂N] and [Emim][Tf₂N]¹³.

The incorporation of hydrogen bonds in the RTIL structure disturbs the coulombic network thus increasing the mobility of the species and decreasing lattice effects. This fact causes the decrease of both melting point and viscosity in [Emim][Tf₂N].

The specific nature of the anion also contributes to the viscosity parameter. RTILs based on $[\text{PF}_6]^-$ or $[\text{BF}_4]^-$ anions show higher viscosity than those containing $[\text{Tf}_2\text{N}]^-$. The shape and size of the anions seems to influence this parameter. Smaller and more symmetric anions show high viscosity values, whereas the biggest ones, with the negative charge well delocalized such as $[\text{Tf}_2\text{N}]^-$, favor lower viscosities³⁵.

The viscosity is linked to the mobility of the species in the RTILs: the high viscous character of RTILs, the low mobility in RTILs influences mass transport properties. The calculated values of diffusion coefficients range between 10^{-7} and $10^{-8} \text{cm}^2 \text{s}^{-1}$, two or three orders of magnitude lower than diffusion coefficients measured in aqueous solutions and in some organic solvents³⁶. Moreover, the classical Stokes-Einstein equation used to describe diffusion phenomena in classical aqueous electrolytes (equation 2.1) does not describe accurately the diffusion in RTILs³⁷:

$$D^0 = kT / 6\pi\eta r \quad (2.1)$$

where D^0 is the diffusion coefficient, k is the Boltzmann constant, η is the viscosity value and r is the radius of the ion.

Although a linear correlation between the diffusion coefficients and the inverse of the viscosities were found for different RTILs plus ferrocene solutions, the slopes of the plots did not provide a reliable value of the ionic radius of ferrocene. Moreover, this value changed with temperature, evidencing that these systems do not obey the Stokes-Einstein equation. The deviation of the Stokes-Einstein equation is not surprising because a RTIL has a slightly flexible glass-like structure so a different motion mechanism is predicted³⁸. In order to explain this deviation, Abbott et al. proposed a model where ionic species move through the ionic liquid jumping from one to another available hole, i.e., it explains the diffusivity phenomena in terms of the free volume in the bulk structure of the IL. In his model, the calculated value of r would be a measure of the size of these holes instead of the radius of the dissolved ions³⁷.

The intrinsic conductivity of RTILs is of crucial importance in electrochemistry. Measured conductivities are quite below the expected values in spite of the high density of charge carries in these media. The lower mobility of the ions in the RTILs can explain their low conductivities. Viscosity and conductivity are linked: an increase of the viscosity causes a decrease in the conductivity. Walden rule relates the conductivity of the electrolyte (Λ) with its viscosity (η) through a thermal constant as follows^{39,40}.

$$\Lambda\eta=k \quad (2.2)$$

Although this rule was initially applied to study aqueous dilute solutions, later it was used to make predictions about the ionicity of other solvents. By plotting the $\log(\Lambda)$ in front of the $\log(1/\eta)$ at different temperatures for a 0.01M KCl solution, a straight line is obtained (Walden's plot). This line is used as the reference to compare with other electrolytes. Under the basis of Walden's rule, many RTILs were analyzed finding that most of them fall quite below this line. Several factors explain the deviation from ideality: 1) The density of the ions is extremely high in these media, so ion pairs that do not contribute in the conductivity are formed; 2) The motion of the ions produces internal electric fields that reduce the effect of the applied electric field affecting the motion of the ions and reducing the conductivity value^{40,41}.

RTILs are desirable electrolytes in electrochemistry due to their wide electrochemical window in which carrying out different processes without the solvent reaction interference. The potential limits in a RTIL depend on the stability of both the cation and the anion. While the anion has low influence in the oxidation limit, the reduction limit depends on the nature of the cation. Imidazolium cation based ionic liquids shows less potential window (1V less) than N,N-dialkyl-pyrrolidinium and tetra-alkyl ammonium ionic liquids^{5, 23, 25}.

2.3) Deep eutectic solvents

A new but totally different class of ionic liquids at room temperature was proposed, named deep eutectic solvents (DESs)⁴¹⁻⁴³. DESs are prepared by the eutectic mixture between a quaternary ammonium salt (for instance a choline chloride, ChCl) and a proton bond donor neutral molecule. Figure 2.3 contains a phase diagram of two components that explains briefly the phenomena of the formation of a DES. Unlike the convectional RTILs that were only composed by discrete ions, DESs contain neutral polar molecules as well as the ions provided by the ammonium quaternary salt dissociation. This explains why DESs must be well differentiated from the rest of ILs. The first published work related to DES was reported by Abbot in 2001⁴³ and since then the increase of interest in using DES for several electrochemical applications was evidenced. DESs are frequently presented as cheap and green alternative due to the commercial availability of the chemicals, the feasibility to synthesize them and finally the low environmental impact⁴⁴. There are many possibilities to synthesize a DES with several available types of bond donor neutral molecules, evidencing their tunability, similar to RTILs. Table 2.4 contains the most typical bond donor molecules employed to produce DESs.

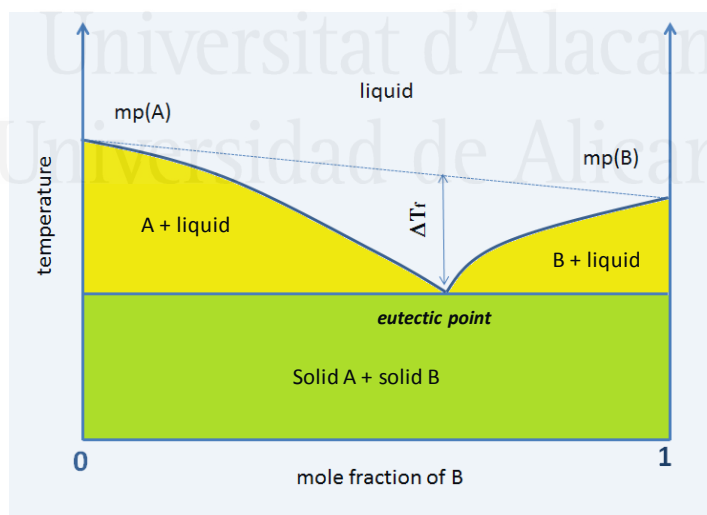


Figure 2.3: Representation of the eutectic point of binary salt. Adapted from reference⁴².

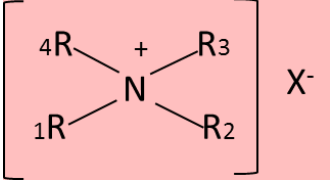
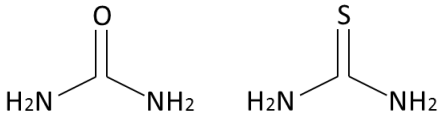
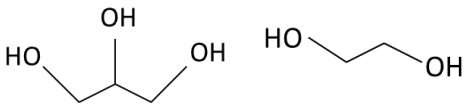
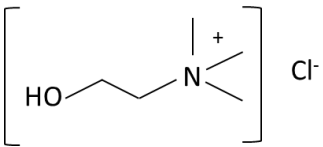
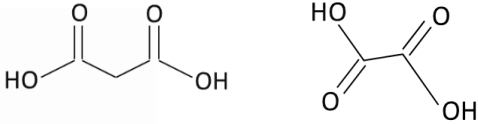
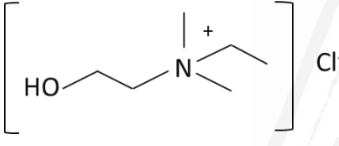
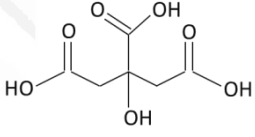
HALIDE SALTS	HYDROGEN BOND DONORS
	 <p style="text-align: center;">Urea Thiourea</p>
<p style="text-align: center;">Ammonium quaternarium salt</p>	 <p style="text-align: center;">Glycerol Ethylene glycol</p>
	<p style="text-align: center;">Carboxylic acids</p>
<p style="text-align: center;">Choline chloride</p>	
	<p style="text-align: center;">Malonic acid Oxalic acid</p>
<p style="text-align: center;">Ethyl(2-hydroxyethyl) dimethylammonium chloride</p>	 <p style="text-align: center;">Citric acid</p>

Table 2.4: Molecular structure of some of the more commonly hydrogen bond donors and halide salts employed in the synthesis of DESs.

DESs share many physical properties with ionic liquids: high viscosities, low melting points, intrinsic conductivity, low diffusion coefficients... But they have many chemical differences. DESs are more viscous and less conductive than convectional RTILs likely due to the less free volume available. The electrochemical window is shorter (1.5-2V) but it is still larger than protic solvents. DESs are quite less thermally stable than RTILs, fact evidenced by the decrease of the potential window as the temperature is increased. However, the tunneability of these solvents and the availability of the chemicals make them also attractive for several field of application, especially in metal electrodeposition⁴².

2.4) Electrodeposition: Field of application of ILs

Among other applications, metal electrodeposition is one of the fields of application where ILs have attracted more the attention^{45, 46}.

Electrodeposition is the science studying the deposition of materials onto a surface through the application of an electric field⁴⁷⁻⁴⁹. The group of materials that can be electrodeposited involves several metals, metal alloys, semiconductors, metal oxides, nanomaterials or even conductive polymers^{45, 49}. The final structure and morphology of the deposits will depend strongly on: 1) the employed substrate, because electrodeposition is a surface process, 2) the electrochemical environment, i.e., the composition of the electrolyte and 3) electrodeposition conditions (applied potential, current density...). Electrodeposition is very demanded in material science due to its simplicity and the fact that it uses low amounts of energy (it can be performed at room temperature). One of the main benefits of the electrodeposition technique is that it allows tuning the properties and structure of the final deposit by changing the electrochemical parameters such as current density and/or applied potential. The composition of the baths also influences the properties of the deposit, and variable morphology or structure can be obtained through the addition of different inorganic or organic additives. Depending on the application, different aspects of the deposits are evaluated: corrosion resistance, adherence, brightness or porosity⁴⁷.

Traditionally, electrodeposition was carried out in aqueous electrolytes, however, electrodeposition in aqueous electrolytes shows some disadvantages that deserves consideration: the main limitation is the narrow potential window of the solvent. The electrodeposition of several metals takes place coupled with the solvent reduction, especially if those metals show a low overpotential for the hydrogen evolution reaction (HER) (Ni, Pt, Co, Fe,...)^{49, 50}. The co-deposition with the reduction of the solvent implies low current efficiencies and the emission of hydrogen gas bubbles that increases the porosity of the deposit and the local pH value, affecting negatively the quality of the coatings. Other inconvenient of aqueous electrolytes is that the temperature is limited to values lower than 100°C. In addition, for many metals deposition requires the use of hazardous baths to provide smooth and compact deposits. One typical example is the cyanide bath for silver electrodeposition⁵¹.

In this sense, the use of ionic liquids for metal electrodeposition is a feasible alternative to aqueous baths: the wide electrochemical window allows the deposition of some metals that cannot be easily deposited in aqueous solution because of the overlapping with the solvent reduction. The lower diffusivity in these media allows the calibration of the metal deposits. The low vapor pressure and thermal stability allows increasing the temperature to enhance mass transport properties. The large number of possibilities to combine cations and anions creates multiple electrochemical environments that can produce new deposits with different both crystalline structures and properties^{49, 52}. Finally, it must be pointed out their relative low toxicity^{47, 51, 53}.

At the beginning, the motivation to use ionic liquids as solvents for electrodeposition appeared with the discovery of the halo-aluminates room temperature ionic liquids (the first generation of ILs). Halo-aluminates RTILs (usually formed by mixing a metal chloride salt like AlCl_3 and an organic chloride salt), were initially employed for the electrodeposition of Al (being the active specie: Al_2Cl_7^-). As the pair $\text{Al}/\text{Al}^{(\text{III})}$ redox equilibrium potential is located at -1.67V vs NHE^{50} , the electrodeposition in aqueous solution is hindered by overlapping with the hydrogen evolution reaction. Despite halo-aluminates are instable towards moisture, they are still used for electroplating. In fact, other metals like Zn, Cu or Co were also successfully deposited in these ILs besides Al⁴⁵.

The introduction of the second generation of RTILs based on the alkyl-imidazolium or alkyl-pyrrolydinium cation allowed extending the range of metals electrodeposited in an ionic liquid. The morphology of the deposit will also depend on the nature of the components of the RTILs, especially on the cation that will be more active in the interfacial region during the electrodeposition process. The species of the ionic liquid can act as surfactant agents providing more homogeneous morphologies⁴⁹. Many metals have been successfully deposited including those that are hardly deposited in aqueous electrolytes, as the magnetic metals such as Ni, Co and Fe⁵⁴⁻⁵⁹. Noble metals like Ag, Cu or Pt were easily deposited in RTILs without the addition of additives⁶⁰⁻⁶²; also semiconductors metals such as Bi or Si and several alloys were also deposited^{45, 52}.

One of the main drawbacks of air and water stable ionic liquids is the relatively low solubility of some metal salts. The solubility parameter depends on the ability to stabilize the cation of the metal salt by complexation with the anion of the RTIL⁵⁶. In

order to improve solubility of some metallic salts in RTILs, new IL formulas are proposed. These new liquids contain a considerable fraction of metallic complexes in the cationic counterpart that contribute to increase the concentration of the electroactive species on the substrate, therefore enhancing the deposition rate. The incorporation of these new ILs containing metal-complexes as cations favors the access of the electroactive species to the substrate and avoids the interference caused by the presence of the cation in the RTILs. In these liquids, the main factor to optimize is the choice of the complexing agent. The complexing agent has two functions: 1) favoring the electrodeposition and 2) balancing the charge to make possible the presence of the anion. Different ligands and structures are currently being proposed looking forward hydrophobic systems. Recently, simple neutral amides (acetamide and urea) mixed with AlCl_3 to form room-temperature ILs have been reported for aluminum electrodeposition. However, these ILs are still moisture sensitive. Alternatively, new proposals involving complexing agents which contain aromatic rings are being checked with the idea that the ring presence could minimize the moisture sensitivity. The development of these ILs by using readily available and relatively hydrophobic neutral ligands could be of great interest for electroplating^{63, 64}.

Relative to deep eutectic solvents employed for electrodeposition, they show good solubility for several metals and mostly better than RTILs. However, their usually narrower electrochemical window compared with the air-stable RTILs can limit the deposition of some metals depending on the catalytic properties of employed substrate. Their different chemical and physical nature provides new structures⁶⁵⁻⁶⁹. One of the benefits that DESs offer is that are less influenced by the presence of small amounts of water⁷⁰, unlike RTILs which properties change dramatically by increasing the water concentration (>100ppm levels)^{71, 72}.

The electrodeposition process is always complex because it involves several steps^{48, 73}: 1) mass transport, 2) removal of the solvation sphere, 3) electron transfer and 4) the formation of a new phase over the substrate. Different deposition mechanisms and crystalline structures are possible due to the different both mass transport and kinetics properties. The whole understanding of the metal deposition process requires a deep analysis of the first stages, which involves nucleation followed by the growth of the nucleus. There are a few attempts that try to analyze the first stages of metal electrodeposition in both DES and RTIL media, most of them onto polycrystalline metal

surfaces or glassy carbon. The nucleation and growth mechanism is usually analyzed according to Scharifker and Hills (S-H) model^{58, 74, 75}. These equations consider two limiting cases where the nucleation can be:

- 1) Instantaneous nucleation (all nucleus formed at the same time):

$$N=N_0 \quad (2.3)$$

- 2) Progressive nucleation (different nucleus formed at different times)^{76, 77}:

$$N=N_0At \quad (2.4)$$

where N is the number of nucleus formed, N_0 is the maximum number of nucleus that can be formed, A the steady state nucleation constant and t is the time at the applied potential.

In ILs, the mechanism usually involves nucleation followed by a 3D growth mechanism diffusion controlled and much higher overpotentials are required to observe significant changes in the mechanism⁴⁹.

Despite the efforts devoted to understanding metal electrodeposition in ILs, there is still some lack of information about how the IL presence modifies the first stages and this question needs clarification. In addition, the use of polycrystalline or not orientated substrates introduces another complexity to the study due to different facets or active sites could contribute differently to the electrochemical response. In this sense, the use of metal single crystal electrodes could improve the analysis of the first stages in metal electrodeposition.

Over some metallic substrates, the monolayer deposition of the metal precursor at potential values more positive than its bulk deposition potential (i.e, its thermodynamic equilibrium potential) can take place. This phenomenon is known as underpotential deposition (UPD) and it is fundamental in the understanding of the first steps of the metal electrodeposition mechanism. UPD formation depends on both the surface orientation and nature of the interfacial region, especially on the anion adsorption. The particular nature of the anion will influence the final structure of the UPD adlayers as long as they interact with the metal precursor or the surface. In ILs media in which a strong surface-ion and ion-metal interactions is expected, the analysis of the UPD formation previous to the overpotential deposition (OPD) could provide relevant information about the metal electrodeposition mechanism in ILs⁷⁸.

UPD is a phenomenon extensively studied in aqueous solution for some metals onto several M(hkl) surfaces in presence of different electrolytes⁷⁸. However, there are only, from now, a few reports that focus on metal UPD in ionic liquids. In this line, some relevant reports in the field deserve attention: UPD of different metals onto Au(hkl) were studied using several techniques: Cyclic voltammetry, Scanning Tunneling microscopy (STM), Atomic Force Microscopy (AFM) or Quartz microbalance^{46, 79}. Endres et al. reported Al UPD on Au(111) using both [Emim][Tf₂N] and [BMP][Tf₂N], and found that Al UPD was strongly influenced by the cation. While UPD was observed under the presence of [Emim], no UPD was detected in [BMP][Tf₂N] due to the strong adsorption of [BMP] on the gold surface⁸⁰. Freyland et al. investigated the UPD deposition of Ni, Co and Zn using chloroaluminate ionic liquids. The initial stages involved Ni and Co island formation, but three monolayers were required for Zn⁸¹⁻⁸³. Mao et al. studied UPD deposition of Sb and Bi. While in aqueous solution the metal precursors Bi(III) and Sb(III) are hydrolyzed, the oxide formation was suppressed in RTIL media. Mao et Al. observed supramolecular aggregation of BiCl₃ and SbCl₃ in [BMI][BF₄], showing different arrangement at different potentials as a result of the balancing between the different competing interactions⁸⁴. The subsequent UPD formation of the bared metals showed atomic structures that displayed “zipper like double chains” patterns. Coinage metals UPD such as Cu UPD were also investigated in ILs media, finding different supramolecular arrangement⁸⁵.

As the metal electrodeposition takes place at the electrified interface, a deep knowledge of the properties that govern the interface Metal|IL is required, in order to increase understanding on the metal electrodeposition in IL medium.

2.5) The electrified metal|IL interface

ILs are high-dense coulombic systems and, consequently, double layer structure in IL media is different than classical double layer in aqueous electrolytes. Among several arrangements, ions tend to organize in multilayers, as proven by AFM measurements, due to the existence of a lattice saturation parameter^{86, 87}. In addition, the non-symmetry between the cation and the anion is an additional factor that complicates the rationalization of the metal|IL interface⁸. These factors, especially both the presence of a lattice saturation parameter and the difference in size and shape between the cation and

the anion, explain that the classical double layer models could no longer incorporate ILs (Gouy-Chapman-Stern). The models that describe inorganic molten salts do not apply for ILs either^{12, 88-90}. The main deviation appears on the capacitance curves (differential capacitance vs applied E) in which the potential of zero charge, pzc , appears located near a maximum instead of appearing centered in the minimum predicted by Gouy-Chapman-Stern (GCS) model. Capacitive curves for molten salts at different temperatures are also different than those reported for IL. Molten salts capacitive curves usually show a parabolic profile with the pzc located at a minimum position in the curve¹². It is worth to mention that Oldham et al. found a simple way to describe the double layer structure of the electrode|IL interface under the principles of GCS model⁹¹. However, this approximation was only valid whether both anion and cation were spheres of the same size, fact that is quite unrealistic. Definitely, several parameters must be considered to properly describe the electric double layer in electrode|ILs interfaces.

The modeling of the double layer electrode|IL is traditionally attributed to Kornyshev, who used Monte Carlo and statistic simulations in his formulation⁹⁰. While Gouy-Chapman-Stern can describe the change of the potential value across the interface by considering that the ions (in dilute aqueous solutions) distribute randomly across the interface (they follow Boltzmann distribution), in IL the short range interactions between the ions are too strong that invalidates GCS to describe them. To solve the mathematical problem, Kornyshev introduces the lattice saturation parameter γ in his formulation. This parameter relates the total number of ions and the number of available sites.

$$\gamma = N_0/N \quad (2.5)$$

Where N_0 is the total number of ions and N is the number of available sites

In terms of concentration, the γ was defined as follows:

$$\gamma = 2c_0/c_{max} \quad (2.6)$$

Where $(2c_0)$ is the total concentration of both anion and cations, and c_{max} is the maximal possible local concentration of ions, considering that the volume of the system does not change with the applied potential. This parameter can vary from 1 (that means there are not free voids and the liquid is completely incompressible) to 0 (ions could occupy any position and Boltzmann distribution is applicable). Depending on the γ value, different shapes in the capacitive curves are obtained: Capacitive curves can show bell-

shaped (for higher γ values) or camel shaped profile (γ lower than $1/3$), where the pzc is located in the maximum of the curve in the former case or between two maxima in the last case. In every case, the capacitance decreases due to strong polarization of the electrode, behavior that is unexpected in the GCS model. This decrease of capacitance value is due to an increase of the double layer thickness because charge of the counterions in the interfacial region are compensated (lattice saturation). Figure 2.4 contains the typical profile of the capacitive curves recorded in aqueous electrolytes.

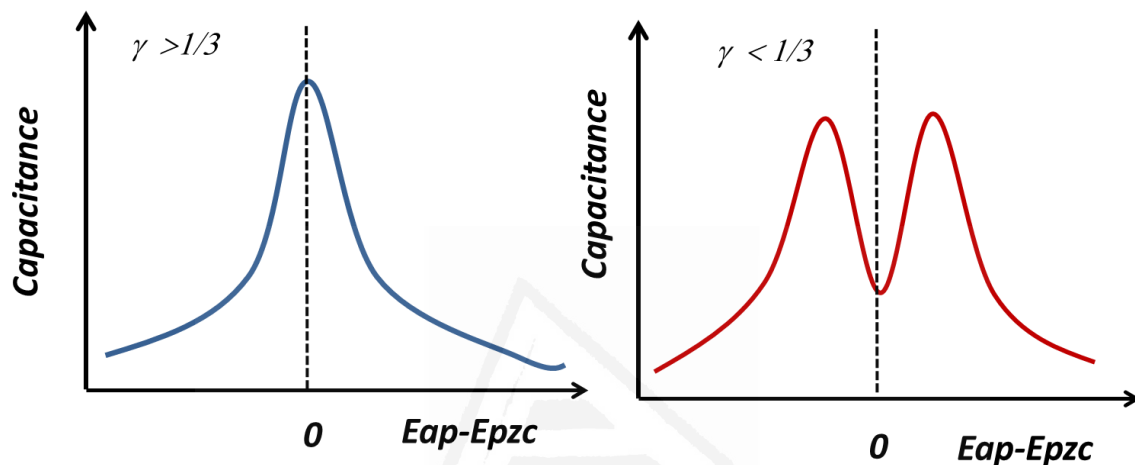


Figure 2.4: Capacitance curves for the Electrode/RTIL interface predicted by Kornyshev as a function of the lattice parameter γ .

However, experimental capacitive curves usually show a profile that is not symmetric around the position of the pzc ^{88, 89, 92}. The explanation to pzc position is that the above formulation only considers the simplest case in which the whole set of short range interactions are similar in energy and both the cation and anion have similar size. The way that Kornyshev found to describe IL with different size-ions was by defining two γ , one for the cation γ_+ and one for the anion γ_- . In the case that the cation was bigger than the anion, one would expect less available voids for the cation and γ_+ should be larger than γ_- . In the new formalism, γ is a function of the applied potential and both γ_+ and γ_- parameters. Different capacitance values are obtained, depending on whether the interface is rich in anions ($E \gg pzc$) or it is rich in cations ($E \ll pzc$). The introduction of γ as a function of the applied potential provides more realistic results. But there is still an uncertainty since the formalism does not take into account the geometry of the ions,

considering them as spheres. Despite modeling the electrode|metal interface is not straightforward, Kornyshev's equations provide results that approach to capacitance curves experimentally obtained⁹²⁻⁹⁶.

Different techniques have been employed to deeply analyze the electrode|IL interface, i.e., at a molecular lever. These techniques include electron microscopies such as Scanning Tunneling Microscopy (STM) or Atomic Force Microscopy (AFM), and several spectroscopies. Infrared Spectroscopy (IR)^{97, 98}, Raman Spectroscopy⁹⁹⁻¹⁰¹ and Sum Frequency Generation (SFG)¹⁰²⁻¹⁰⁴ are some of the commonly spectroscopic techniques used. Besides the different camel-shape or bell-shaped capacitance curves, the double layer in ionic liquids showed other particularities. Specifically, their response through the applied potential showed non-reversible behavior and dependence with the direction of the applied potential. Osawa et al. demonstrated that the restructuration of the IL network in the proximities of the electrode was potential dependent and showed a hysteresis behavior⁹⁷. This behavior was specifically reported for [Bmim][Tf₂N] on polycrystalline gold electrode. Baldelli et al.^{102, 103} found that some RTILs showed the same potential dependence trend, but they used polycrystalline platinum electrode as the substrate. These works evidenced that the dynamics of double layer restructuration in IL media are slow and potential dependent, but also the interactions involving ions and the selected substrate influence the interfacial properties, especially if the employed substrate is platinum^{104, 105}.

The use of polycrystalline electrodes complicates the interpretation of the results. Most of the works that use single crystal electrodes to investigate the interfacial region M(hkl)|IL, employ non-polarizable surfaces such as Au or Ag. For instance, Mao et al. combined capacitance and STM measures using gold single crystal electrodes. So, they investigated the interfaces Au(111) and Au(100) in contact with [Bmim][BF₄] and [Bmim][PF₆] respectively^{86, 92}. STM technique provide images of the ordered anion or cation arrays at applied potentials far from the maximum potential value in the capacitance curve, then supporting that the *pzc* was located near this maximum. This work provided good correlation between capacitance curves and molecular arrangement onto the single crystal electrodes. On the other hand, the reorganization of the species of the ionic liquid (specifically the cation) were sensitive to the gold surface orientation, showing worm-like structures on Au(111), and zig-zag or straight arrangements over Au(100). Behm et al. also used single crystal electrodes to analyze the interfacial region

between an IL and a metal electrode, combining STM measurements with Density Functional Theory (DFT) calculations to analyze the type of interactions that stabilize the different structures¹⁰⁶. On the other hand, several works that used AFM confirmed that interfacial ions arrange in multilayers. The first layer is dominated by the presence of either the cation or the anion, depending on the surface polarization, and the subsequent layers contain the counter ions^{107, 108}. At potentials close to the pzc , the ions may arrange randomly similar to bulk structure⁸⁶. Figure 2.5 contains a scheme of the distribution of the ions in the double layer, as predicted by AFM and spectroscopic measurements:

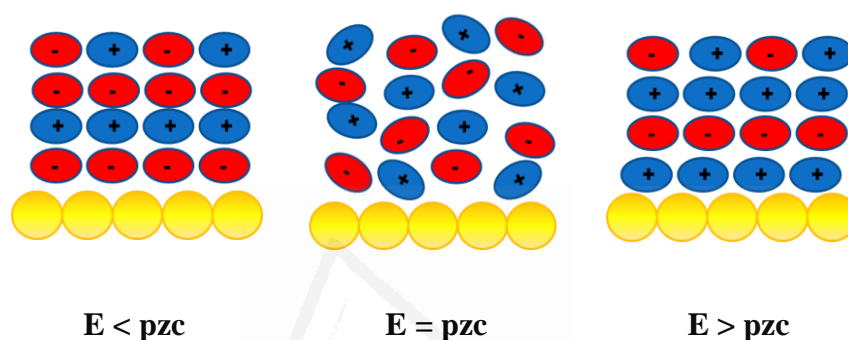


Figure 2.5: Double layer restructuring as a function of the applied potential.

Several ionic structures near the surface electrode have been proposed more recently: These structures vary from self-assembled structures, checkerboard, lamellar, coil-like, worm-like, micelle-like adsorbed ion structures to “island” type arrangements, monolayer, bilayer as well as multilayer structures¹⁰⁹.

Finally, the effect of the temperature on the double layer was also analyzed. By increasing the temperature, the general trend is a decrease of the capacitance value. The explanation is that the increase in temperature increases the mobility of the ions, causing a disordering in the interfacial region. Then the density of ions in the electrified interface decreases and thus the differential capacitance decreases¹¹⁰.

DES interfacial properties have been less investigated than RTILs. It is worth to say that different studies that combine capacitive measures and cyclic voltammetry are reported^{93, 111}. Some of these studies that employed DES based on chloride choline plus a bond donor molecule have reported capacitive curves that show important dissimilarities with those ascribed for RTILs. One important difference is that, at high negative applied

potentials the capacitance does not decrease like in RTIL media (Figure 2.3)¹¹⁰. The main chemical difference between an RTIL and a DES is that RTILs are formed by discrete anions whereas DESs contain a salt (such as ChCl) dissolved in a neutral molecule environment. Their particular chemical structure has made that some authors supported the idea that the double layer in DES approaches to a Helmholtz double layer type at enough negative applied potentials. However, the description of the DES double layer is not trivial. In this line, Abbott et al. proposed that DES behaves more like to RTIL when the charge transport of ions in DES takes places through the holes, while they behave more like classical solvents when the ion charge transport is dominated by the movement of the ions, which can happen if the ratio between the salt/bond donor is lower in the eutectic mixture⁴².

2.6) The influence of the impurities in the double layer properties. The purification of ILs

One of the main inconveniences to deal with ILs is the relative high amount of impurities that normally contain. These impurities change the nature and properties of the metal|IL properties. For instance, they are responsible of the decrease in the electrochemical window among other effects. These impurities also affect the physical and chemical properties such as the melting point or viscosity. Obviously, the change in the properties is linked with a change in the distribution of the ions in the ionic network, since these impurities disrupt the network⁴⁶.

Within the possible impurities that can be found in IL, halides and small organic molecules like acetone are the most common^{46, 112}. While halides decrease the electrochemical window and increase the viscosity, the presence of acetone gives a yellow color to the DES. These impurities, especially halides, come from the synthesis procedures. The synthesis of RTILs involves the metathesis between the halide of the corresponding cation, called precursor, and a salt of the anion, as showed in Figure 2.6⁴.

RTIL SYNTHESIS: METATHESIS

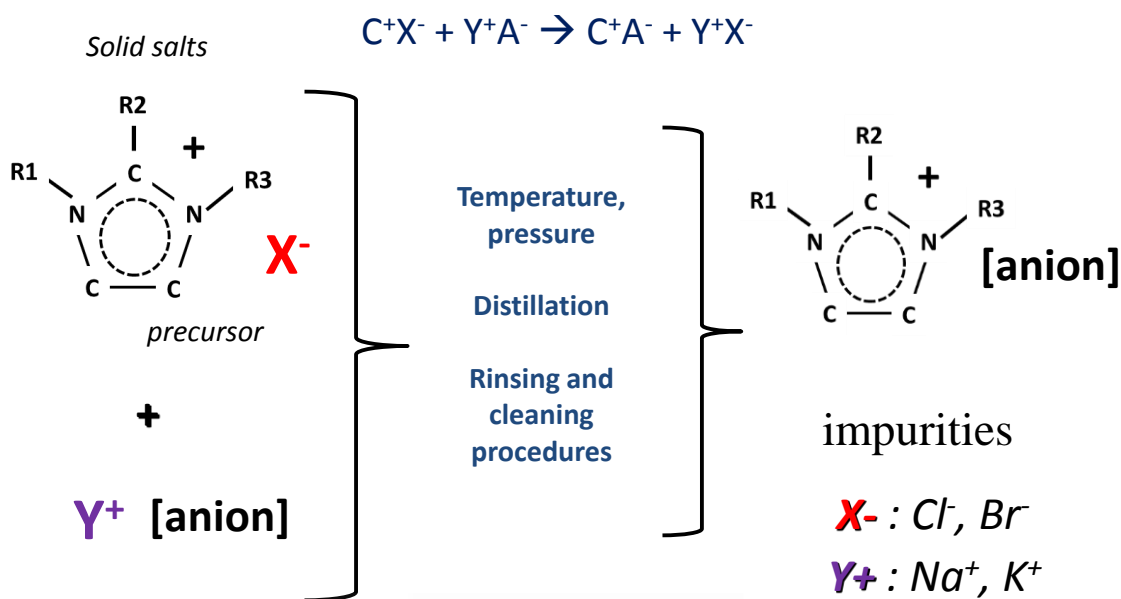


Figure 2.6: Scheme of the synthesis procedure of an RTIL.

Literature provides several procedures to remove the impurities in an RTIL: rinsing and extraction with water to separate the soluble compounds in the aqueous phase; using activated carbon followed by alumina column; chromatography to separate the impurities according to their polarity; distillation or rotating vapor to evaporate small organic molecules of higher vapor pressure^{46, 97}. The final concentration of impurities usually ranges between 1-60ppm in high quality RTILs.

Among other impurities, water is, in particular, quite difficult to remove from the RTIL due to the general hygroscopic character of these solvents. High vacuum conditions in combination with temperature and stirring conditions are the methods usually employed to remove water in RTIL⁴⁶. On the other hand, Kolb et al. reported a procedure to purify a RTIL that, besides reducing the initial water concentration, it also removes some impurities that are electrochemically active. This method consists on using active molecular sieves. According to the author, the size of the molecular sieves must not be higher than 3Å, otherwise the method does not work properly according to the voltammetric evidence²⁰.

It is of paramount importance to control and reduce the levels of water inside the IL because the presence of low water amounts (>50ppm) modify dramatically the

interfacial properties of electrode|RTILs interface. For that reason, the use of a Karl Fischer titration is needed in order to evaluate the water content. Different works focused on the effect of water in the properties of ILs found that, by increasing the water concentration, the multilayer arrangement of IL tends to disappear and instead of that the molecules in the double layer arrangement approach to Gouy-Chapman-Stern double layer framework^{71, 72, 113}. The intrusion of the small molecules of water would break the multilayer ionic network. These changes in the double layer region also cause a shift in the potential of zero charge to less positive potentials⁷². In addition, the change in the applied potential causes that the population of water molecules on the surface increases until they form a monolayer on the surface, in a similar way that happens in some organic solvents such as acetonitrile¹¹⁴, likely because of both the polarizability and the small size of the water molecules. High water concentrations cause a decrease of the electrochemical window due to water reduction or oxidation reaction. On the other side, the presence of water decreases the viscosity parameter and increases the conductivity which is, in fact, desirable¹¹⁵. At moderate applied potentials (near to the *pzc*) the water molecules distribute occupying the available voids or spaces in the ionic network instead of laying on the surface, according to simulations performed by Kornishev et al.¹¹⁶. Kornishev argued that the presence of a high dense ionic atmosphere in the RTIL creates inhomogeneous electric fields that compete with the applied electric field on the surface and avoids that the water molecules concentrate on the surface¹¹⁶.

DESs are more affordable than RTILs from the point of view of impurities content or influence. DESs are easier to prepare than RTILs, and the procedure does not introduce other agents different than the two components from the eutectic mixture. On the other hand, DESs are less sensitive to the presence of water^{44, 70, 117-119}. Both the electrochemical response and potential window do not change significantly until the percentage of water raises up to 9%⁷⁰. Despite DESs usually contain higher percentages of water than RTILs, in the DESs the water could be well stabilized by hydrogen bond formation. It is worth to say that most of the works that investigate DESs use non-polarizable surfaces like gold or glassy carbon which are not highly active to water reduction/oxidation. In this line, it would be interesting to investigate high active surfaces (for instance, Pt) in order to confirm the sensitivity of both RTILs and DESs to the presence of water.

In summary, the performed research until nowadays has provided considerable information from ILs. In fact, many RTILs have been well characterized especially those that contains the $[\text{Tf}_2\text{N}]^-$, $[\text{BF}_4]^-$ or $[\text{PF}_6]^-$ anions. However, related to the interfacial properties, some lack of information remains because most of the experimental works are performed on poly-orientated surfaces or well defined non-polarizable electrodes such as Au(hkl) or Ag(hkl). Then, investigation related with how these solvents behave in contact with high active orientated surfaces is required, especially for catalysis in order to extend their field of application. Platinum single crystal electrodes are good candidates and a model electrocatalyst. But little work focused on the study of Pt(hkl)|IL interfaces¹²⁰⁻¹²³ is provided in the literature. The main reason lays on the fact that Pt(hkl) is strongly sensitive to contamination by exposure to the environment¹²⁴.

2.7) REFERENCES

- (1) Armand, M.; Endres, F.; MacFarlane, D. R.; Ohno, H.; Scrosati, B., Ionic-liquid materials for the electrochemical challenges of the future. *Nature Materials* **2009**, *8* (8), 621-629.
- (2) Walden, P., Molecular weights and electrical conductivity of several fused salts. *Bulletin of the Russian Academy of Sciences* **1914**, 405-422.
- (3) Sebastiao, E.; Cook, C.; Hu, A.; Murugesu, M., Recent developments in the field of energetic ionic liquids. *Journal of Materials Chemistry A* **2014**, *2* (22), 8153-8173.
- (4) Hallett, J. P.; Welton, T., Room-temperature ionic liquids: Solvents for synthesis and catalysis. 2. *Chemical Reviews* **2011**, *111* (5), 3508-3576.
- (5) Buzzeo, M. C.; Evans, R. G.; Compton, R. G., Non-haloaluminate room-temperature ionic liquids in electrochemistry, a review. *ChemPhysChem* **2004**, *5* (8), 1106-1120.
- (6) MacFarlane, D. R.; Tachikawa, N.; Forsyth, M.; Pringle, J. M.; Howlett, P. C.; Elliott, G. D.; Davis, J. H.; Watanabe, M.; Simon, P.; Angell, C. A., Energy applications of ionic liquids. *Energy & Environmental Science* **2014**, *7* (1), 232-250.
- (7) Gebresilassie Eshetu, G.; Armand, M.; Scrosati, B.; Passerini, S., Energy storage materials synthesized from ionic liquids. *Angewandte Chemie International Edition* **2014**, *53* (49), 13342-13359.
- (8) Fedorov, M. V.; Kornyshev, A. A., Ionic liquids at electrified interfaces. *Chemical Reviews* **2014**, *114* (5), 2978-3036.
- (9) Hayes, R.; Warr, G. G.; Atkin, R., Structure and nanostructure in ionic liquids. *Chemical Reviews* **2015**, *115* (13), 6357-6426.
- (10) Zhang, S.; Sun, N.; He, X.; Lu, X.; Zhang, X., Physical properties of ionic liquids: Database and evaluation. *Journal of Physical and Chemical Reference Data* **2006**, *35* (4), 1475-1517.
- (11) Gabriel, S.; Weiner, J., Ueber einige abkömmlinge des propylamins. *Berichte der deutschen chemischen Gesellschaft* **1888**, *21* (2), 2669-2679.

-
- (12) Conway, B. E.; Liu, J.; Qian, S. Y., Structure of interphases of low melting point salts and protonic hydrates with mercury and gold in relation to double-layer capacitance behaviour. *Journal of Electroanalytical Chemistry* **1992**, *329* (1), 201-223.
- (13) Dong, K.; Zhang, S. J., Hydrogen bonds: A structural insight into ionic liquids. *Chemistry-a European Journal* **2012**, *18* (10), 2748-2761.
- (14) Hurley, F. H.; Wier, T. P., Jr., The electrodeposition of aluminum from nonaqueous solutions at room temperature. *Journal of the Electrochemical Society* **1951**, *98* (5), 207-212.
- (15) Wilkes, J. S.; Levisky, J. A.; Wilson, R. A.; Hussey, C. L., Dialkylimidazolium chloroaluminate melts: A new class of room-temperature ionic liquids for electrochemistry, spectroscopy and synthesis. *Inorganic Chemistry* **1982**, *21* (3), 1263-1264.
- (16) Hussey, C. L., In *Chemistry of nonaqueous solutions*, G. Mamantov, A. I. P., Ed. 1994; 227-275.
- (17) Wilkes, J. S.; Zaworotko, M. J., Air and water stable 1-ethyl-3-methylimidazolium based ionic liquids. *Journal of the Chemical Society, Chemical Communications* **1992**, (13), 965-967.
- (18) Cammarata, L.; Kazarian, S. G.; Salter, P. A.; Welton, T., Molecular states of water in room temperature ionic liquids. *Physical Chemistry Chemical Physics* **2001**, *3* (23), 5192-5200.
- (19) Bonhôte, P.; Dias, A. P.; Papageorgiou, N.; Kalyanasundaram, K.; Grätzel, M., Hydrophobic, highly conductive ambient-temperature molten salts. *Inorganic Chemistry* **1996**, *35* (5), 1168-1178.
- (20) Gnahn, M.; Kolb, D. M., The purification of an ionic liquid. *Journal of Electroanalytical Chemistry* **2011**, *651* (2), 250-252.
- (21) Matsumoto, H.; Yanagida, M.; Tanimoto, K.; Nomura, M.; Kitagawa, Y.; Miyazaki, Y. Highly conductive room temperature molten salts based on small trimethylalkylammonium cations and bis (trifluoromethylsulfonyl) imide. *Chemistry Letters* **2000**, *29* (8), 922-923.
- (22) Matsumoto, H.; Matsuda, T.; Miyazaki, Y., Room temperature molten salts based on trialkylsulfonium cations and bis (trifluoromethylsulfonyl) imide. *Chemistry Letters* **2000**, *29* (12), 1430-1431.
- (23) Sun, J.; Forsyth, M.; MacFarlane, D. R., Room temperature molten salts based on the quaternary ammonium ion. *The Journal of Physical Chemistry B* **1998**, *102* (44), 8858-8864.
- (24) Appetecchi, G. B.; Scaccia, S.; Tizzani, C.; Alessandrini, F.; Passerini, S., Synthesis of hydrophobic ionic liquids for electrochemical applications. *Journal of the Electrochemical Society* **2006**, *153* (9), A1685-A1691.
- (25) MacFarlane, D. R.; Meakin, P.; Sun, J.; Amini, N.; Forsyth, M., Pyrrolidinium imides: A new family of molten salts and conductive plastic crystal phases. *The Journal of Physical Chemistry B* **1999**, *103* (20), 4164-4170.
- (26) D. Holbrey, J.; R. Seddon, K., The phase behaviour of 1-alkyl-3-methylimidazolium tetrafluoroborates; ionic liquids and ionic liquid crystals. *Journal of the Chemical Society, Dalton Transactions* **1999**, (13), 2133-2140.
-

-
- (27) Greaves, T. L.; Drummond, C. J., Protic ionic liquids: Properties and applications. *Chemical Reviews* **2008**, *108* (1), 206-237.
- (28) Tokuda, H.; Tsuzuki, S.; Susan, M. A. B. H.; Hayamizu, K.; Watanabe, M., How ionic are room-temperature ionic liquids? An indicator of the physicochemical properties. *Journal of Physical Chemistry B* **2006**, *110* (39), 19593-19600.
- (29) Dzyuba, S. V.; Bartsch, R. A., Influence of structural variations in 1-alkyl(aralkyl)-3-methylimidazolium hexafluorophosphates and bis(trifluoromethylsulfonyl)imides on physical properties of the ionic liquids. *ChemPhysChem* **2002**, *3* (2), 161-166.
- (30) Tokuda, H.; Hayamizu, K.; Ishii, K.; Susan, M. A. B. H.; Watanabe, M., Physicochemical properties and structures of room temperature ionic liquids. 2. Variation of alkyl chain length in imidazolium cation. *The Journal of Physical Chemistry B* **2005**, *109* (13), 6103-6110.
- (31) Hitchcock, P. B.; Seddon, K. R.; Welton, T., Hydrogen-bond acceptor abilities of tetrachlorometalate(ii) complexes in ionic liquids. *Journal of the Chemical Society, Dalton Transactions* **1993**, (17), 2639-2643.
- (32) Holbrey, J. D.; Reichert, W. M.; Nieuwenhuyzen, M.; Sheppard, O.; Hardacre, C.; Rogers, R. D., Liquid clathrate formation in ionic liquid-aromatic mixtures. *Chemical Communications* **2003**, (4), 476-477.
- (33) Deetlefs, M.; Hardacre, C.; Nieuwenhuyzen, M.; Padua, A. A. H.; Sheppard, O.; Soper, A. K., Liquid structure of the ionic liquid 1,3-dimethylimidazolium bis((trifluoromethyl)sulfonyl)amide. *The Journal of Physical Chemistry B* **2006**, *110* (24), 12055-12061.
- (34) Fumino, K.; Wulf, A.; Ludwig, R., Strong, localized, and directional hydrogen bonds fluidize ionic liquids. *Angewandte Chemie International Edition* **2008**, *47* (45), 8731-8734.
- (35) Tokuda, H.; Hayamizu, K.; Ishii, K.; Susan, M. A. B. H.; Watanabe, M., Physicochemical properties and structures of room temperature ionic liquids. 1. Variation of anionic species. *Journal of Physical Chemistry B* **2004**, *108* (42), 16593-16600.
- (36) Silvester Debbie, S.; Compton Richard, G., Electrochemistry in room temperature ionic liquids: A review and some possible applications. In *Zeitschrift für Physikalische Chemie*, 2006; Vol. 220, p 1247.
- (37) Taylor, A. W.; Licence, P.; Abbott, A. P., Non-classical diffusion in ionic liquids. *Physical Chemistry Chemical Physics* **2011**, *13* (21), 10147-10154.
- (38) Abbott, A. P.; Harris, R. C.; Ryder, K. S., Application of hole theory to define ionic liquids by their transport properties. *Journal of Physical Chemistry B* **2007**, *111* (18), 4910-4913.
- (39) Walden, P. Z. *Physik chem* **1906**, *55*, 207-246.
- (40) MacFarlane, D. R.; Forsyth, M.; Izgorodina, E. I.; Abbott, A. P.; Annat, G.; Fraser, K., On the concept of ionicity in ionic liquids. *Physical Chemistry Chemical Physics* **2009**, *11* (25), 4962-4967.
- (41) Abbott, A. P.; Boothby, D.; Capper, G.; Davies, D. L.; Rasheed, R. K., Deep eutectic solvents formed between choline chloride and carboxylic acids: Versatile alternatives to ionic liquids. *Journal of the American Chemical Society* **2004**, *126* (29), 9142-9147.
- (42) Smith, E. L.; Abbott, A. P.; Ryder, K. S., Deep eutectic solvents (DESS) and their applications. *Chemical Reviews* **2014**, *114* (21), 11060-11082.
-

-
- (43) Abbott, A. P.; Capper, G.; Davies, D. L.; Munro, H. L.; Rasheed, R. K.; Tambyrajah, V., Preparation of novel, moisture-stable, lewis-acidic ionic liquids containing quaternary ammonium salts with functional side chains. *Chemical Communications* **2001**, (19), 2010-2011.
- (44) Florindo, C.; Oliveira, F. S.; Rebelo, L. P. N.; Fernandes, A. M.; Marrucho, I. M., Insights into the synthesis and properties of deep eutectic solvents based on cholinium chloride and carboxylic acids. *ACS Sustainable Chemistry and Engineering* **2014**, 2 (10), 2416-2425.
- (45) Zhang, Q.; Wang, Q.; Zhang, S.; Lu, X.; Zhang, X., Electrodeposition in ionic liquids. *ChemPhysChem* **2016**, 17 (3), 335-351.
- (46) Su, Y. Z.; Fu, Y. C.; Wei, Y. M.; Yan, J. W.; Mao, B. W., The electrode/ionic liquid interface: Electric double layer and metal electrodeposition. *ChemPhysChem* **2010**, 11 (13), 2764-2778.
- (47) Dini, J. W., *Electrodeposition. The material science of coatings and substrates*. Noyes Publications, 1993, 367pp.
- (48) Gileadi, E., The enigma of metal deposition. *Journal of Electroanalytical Chemistry* **2011**, 660 (2), 247-253.
- (49) Frank Endres, D. R. M., Andrew Abbott, *Electrodeposition from ionic liquids*. 2nd ed.; Wiley: 2017; p 486..
- (50) Lide, C. R., *Crc handbook of chemistry and physics*. 79 ed.; CRC Press: Boca Raton, 1998.
- (51) Bomparola, R.; Caporali, S.; Lavacchi, A.; Bardi, U., Silver electrodeposition from air and water-stable ionic liquid: An environmentally friendly alternative to cyanide baths. *Surface and Coatings Technology* **2007**, 201 (24), 9485-9490.
- (52) Katayama, Y., Electrodeposition of metals in ionic liquids. In *Electrochemical aspects of ionic liquids*, 2005; 111-131.
- (53) El Abedin, S. Z.; Pölleth, M.; Meiss, S. A.; Janek, J.; Endres, F., Ionic liquids as green electrolytes for the electrodeposition of nanomaterials. *Green Chemistry* **2007**, 9 (6), 549-553.
- (54) Zhu, Y. L.; Katayama, Y.; Miura, T., Effects of acetonitrile on electrodeposition of Ni from a hydrophobic ionic liquid. *Electrochimica Acta* **2010**, 55 (28), 9019-9023.
- (55) Zhu, Y. L.; Katayama, Y.; Miura, T. In *Electrochemical preparation of nickel and iron nanoparticles in a hydrophobic ionic liquid*, *ECS Transactions*, 2010; pp 537-541.
- (56) Zhu, Y. L.; Katayama, Y.; Miura, T., Electrochemical co-deposition of iron and nickel from a hydrophobic ionic liquid. *Journal of the Electrochemical Society* **2015**, 162 (8), D371-D375.
- (57) Meenatchi, B.; Renuga, V.; Manikandan, A., Electrodeposition of nickel on glassy carbon electrode from protic ionic liquids with imidazolium cation. *Journal of Inorganic and Organometallic Polymers and Materials* **2016**, 1-8.
- (58) Katayama, Y.; Fukui, R.; Miura, T., Electrodeposition of cobalt from an imide-type room-temperature ionic liquid. *Journal of the Electrochemical Society* **2007**, 154 (10), D534-D537.
- (59) Liu, Z.; Cui, T.; Pulletikurthi, G.; Lahiri, A.; Carstens, T.; Olschewski, M.; Endres, F., Dendrite-free nanocrystalline zinc electrodeposition from an ionic liquid containing
-

-
- nickel triflate for rechargeable zn-based batteries. *Angewandte Chemie - International Edition* **2016**, *55* (8), 2889-2893.
- (60) Katayama, Y.; Dan, S.; Miura, T.; Kishi, T., Electrochemical behavior of silver in 1-ethyl-3-methylimidazolium tetrafluoroborate molten salt. *Journal of the Electrochemical Society* **2001**, *148* (2), C102-C105.
- (61) Bando, Y.; Katayama, Y.; Miura, T., Electrodeposition of palladium in a hydrophobic 1-n-butyl-1-methylpyrrolidinium bis(trifluoromethylsulfonyl)imide room-temperature ionic liquid. *Electrochimica Acta* **2007**, *53* (1), 87-91.
- (62) Katayama, Y.; Endo, T.; Miura, T.; Toshima, K., Electrodeposition of gold in an amide-type ionic liquid. *Journal of the Electrochemical Society* **2014**, *161* (3), D87-D91.
- (63) Endo, A.; Miyake, M.; Hirato, T., Electrodeposition of aluminum from 1,3-dimethyl-2-imidazolidinone/ AlCl_3 baths. *Electrochimica Acta* **2014**, *137*, 470-475.
- (64) Fang, Y.; Yoshii, K.; Jiang, X.; Sun, X.-G.; Tsuda, T.; Mehio, N.; Dai, S., An AlCl_3 based ionic liquid with a neutral substituted pyridine ligand for electrochemical deposition of aluminum. *Electrochimica Acta* **2015**, *160*, 82-88.
- (65) Abbott, A. P.; Ttaib, K. E.; Frisch, G.; Ryder, K. S.; Weston, D., The electrodeposition of silver composites using deep eutectic solvents. *Physical Chemistry Chemical Physics* **2012**, *14* (7), 2443-2449.
- (66) Tsuda, T.; Boyd, L. E.; Kuwabata, S.; Hussey, C. L., Electrochemistry of copper(I) oxide in the 66.7-33.3 mol % urea-choline chloride room-temperature eutectic melt. *Journal of the Electrochemical Society* **2010**, *157* (8), F96-F103.
- (67) Gu, C.; Tu, J., One-step fabrication of nanostructured ni film with lotus effect from deep eutectic solvent. *Langmuir* **2011**, *27* (16), 10132-10140.
- (68) Abbott, A. P.; Ballantyne, A.; Harris, R. C.; Juma, J. A.; Ryder, K. S., A comparative study of nickel electrodeposition using deep eutectic solvents and aqueous solutions. *Electrochimica Acta* **2015**, *176*, 718-726.
- (69) Li, M.; Wang, Z.; Reddy, R. G., Cobalt electrodeposition using urea and choline chloride. *Electrochimica Acta* **2014**, *123*, 325-331.
- (70) Du, C.; Zhao, B.; Chen, X.-B.; Birbilis, N.; Yang, H., Effect of water presence on choline chloride-2urea ionic liquid and coating platings from the hydrated ionic liquid. *Scientific Reports* **2016**, *6*, 29225.
- (71) Cui, T.; Lahiri, A.; Carstens, T.; Borisenko, N.; Pulletikurthi, G.; Kuhl, C.; Endres, F., Influence of water on the electrified ionic liquid/solid interface: A direct observation of the transition from a multilayered structure to a double-layer structure. *The Journal of Physical Chemistry C* **2016**, *120* (17), 9341-9349.
- (72) Zhong, Y.; Yan, J.; Li, M.; Chen, L.; Mao, B., The electric double layer in an ionic liquid incorporated with water molecules: Atomic force microscopy force curve study. *ChemElectroChem* **2016**, *3* (12), 2221-2226.
- (73) Pinto, L. M. C.; Spohr, E.; Quaino, P.; Santos, E.; Schmickler, W., Why silver deposition is so fast: Solving the enigma of metal deposition. *Angewandte Chemie International Edition* **2013**, *52* (30), 7883-7885.
- (74) Tułodziecki, M.; Tarascon, J. M.; Taberna, P. L.; Guéry, C., Importance of the double layer structure in the electrochemical deposition of Co from soluble Co^{2+} - based precursors in ionic liquid media. *Electrochimica Acta* **2014**, *134*, 55-66.
-

- (75) Tułodziecki, M.; Tarascon, J. M.; Taberna, P. L.; Guéry, C., Non-equilibrium ionic liquid-electrode interface at elevated temperature and its influence on Co^{2+} reduction process. *Journal of the Electrochemical Society* **2016**, *163* (8), D355-D365.
- (76) Gunawardena, G.; Hills, G.; Montenegro, I.; Scharifker, B., Electrochemical nucleation. Part i. General considerations. *Journal of Electroanalytical Chemistry* **1982**, *138* (2), 225-239.
- (77) Scharifker, B.; Hills, G., Theoretical and experimental studies of multiple nucleation. *Electrochimica Acta* **1983**, *28* (7), 879-889.
- (78) Herrero, E.; Buller, L. J.; Abruna, H. D., Underpotential deposition at single crystal surfaces of Au, Pt, Ag and other materials. *Chemical Reviews* **2001**, *101* (7), 1897-1930.
- (79) Carstens, T.; Ispas, A.; Borisenko, N.; Atkin, R.; Bund, A.; Endres, F., In situ scanning tunneling microscopy (STM), atomic force microscopy (AFM) and quartz crystal microbalance (EQCM) studies of the electrochemical deposition of tantalum in two different ionic liquids with the 1-butyl-1-methylpyrrolidinium cation. *Electrochimica Acta* **2016**, *197*, 374-387.
- (80) Moustafa, E. M.; El Abedin, S. Z.; Shkurankov, A.; Zschippang, E.; Saad, A. Y.; Bund, A.; Endres, F., Electrodeposition of Al in 1-butyl-1-methylpyrrolidinium bis(trifluoromethylsulfonyl)amide and 1-ethyl-3-methylimidazolium bis(trifluoromethylsulfonyl)amide ionic liquids: In situ STM and EQCM studies. *Journal of Physical Chemistry B* **2007**, *111* (18), 4693-4704.
- (81) Dogel, J.; Freyland, W., Layer-by-layer growth of zinc during electrodeposition on Au(111) from a room temperature molten salt. *Physical Chemistry Chemical Physics* **2003**, *5* (12), 2484-2487.
- (82) Mann, O.; Freyland, W., Electrocrystallization of distinct Ni nanostructures at the ionic liquid|Au(111) interface: An electrochemical and in-situ STM investigation. *Journal of Physical Chemistry C* **2007**, *111* (27), 9832-9838.
- (83) Zell, C. A.; Freyland, W., In situ STM and STS study of Co and Co-Al alloy electrodeposition from an ionic liquid. *Langmuir* **2003**, *19* (18), 7445-7450.
- (84) Fu, Y.-C.; Su, Y.-Z.; Wu, D.-Y.; Yan, J.-W.; Xie, Z.-X.; Mao, B.-W., Supramolecular aggregation of inorganic molecules at Au(111) electrodes under a strong ionic atmosphere. *Journal of the American Chemical Society* **2009**, *131* (41), 14728-14737.
- (85) Endres, F.; Schweizer, A., The electrodeposition of copper on Au(111) and on HOPG from the 66/34 mol% aluminium chloride/1-butyl-3-methylimidazolium chloride room temperature molten salt: An EC-STM study. *Physical Chemistry Chemical Physics* **2000**, *2* (23), 5455-5462.
- (86) Zhang, X.; Zhong, Y. X.; Yan, J. W.; Su, Y. Z.; Zhang, M.; Mao, B. W., Probing double layer structures of Au(111) [Bmi][Pf₆] ionic liquid interfaces from potential-dependent AFM force curves. *Chemical Communications* **2012**, *48* (4), 582-584.
- (87) Zhong, Y. X.; Yan, J. W.; Li, M. G.; Zhang, X.; He, D. W.; Mao, B. W., Resolving fine structures of the electric double layer of electrochemical interfaces in ionic liquids with an AFM tip modification strategy. *Journal of the American Chemical Society* **2014**, *136* (42), 14682-14685.
- (88) Fedorov, M. V.; Kornyshev, A. A., Towards understanding the structure and capacitance of electrical double layer in ionic liquids. *Electrochimica Acta* **2008**, *53* (23), 6835-6840.

-
- (89) Fedorov, M. V.; Kornyshev, A. A., Ionic liquid near a charged wall: Structure and capacitance of electrical double layer. *Journal of Physical Chemistry B* **2008**, *112* (38), 11868-11872.
- (90) Kornyshev, A. A., Double-layer in ionic liquids: Paradigm change? *Journal of Physical Chemistry B* **2007**, *111* (20), 5545-5557.
- (91) Oldham, K. B., A Gouy-Chapman-Stern model of the double layer at a (metal)/(ionic liquid) interface. *Journal of Electroanalytical Chemistry* **2008**, *613* (2), 131-138.
- (92) Su, Y. Z.; Yan, J. W.; Li, M. G.; Zhang, M.; Mao, B. W., Electric double layer of Au(100)/imidazolium-based ionic liquids interface: Effect of cation size. *Journal of Physical Chemistry C* **2013**, *117* (1), 205-212.
- (93) Figueiredo, M.; Gomes, C.; Costa, R.; Martins, A.; Pereira, C. M.; Silva, F., Differential capacity of a deep eutectic solvent based on choline chloride and glycerol on solid electrodes. *Electrochimica Acta* **2009**, *54* (9), 2630-2634.
- (94) Gomes, C.; Costa, R.; Pereira, C. M.; Silva, A. F., The electrical double layer at the ionic liquid/Au and Pt electrode interface. *RSC Advances* **2014**, *4* (55), 28914-28921.
- (95) Gnahn, M.; Pajkossy, T.; Kolb, D. M., The interface between Au(111) and an ionic liquid. *Electrochimica Acta* **2010**, *55* (21), 6212-6217.
- (96) Gnahn, M.; Muller, C.; Repanszki, R.; Pajkossy, T.; Kolb, D. M., The interface between Au(100) and 1-butyl-3-methyl-imidazolium-hexafluorophosphate. *Physical Chemistry Chemical Physics* **2011**, *13* (24), 11627-11633.
- (97) Motobayashi, K.; Minami, K.; Nishi, N.; Sakka, T.; Osawa, M., Hysteresis of potential-dependent changes in ion density and structure of an ionic liquid on a gold electrode: In situ observation by surface-enhanced infrared absorption spectroscopy. *Journal of Physical Chemistry Letters* **2013**, *4* (18), 3110-3114.
- (98) Yang, Y. Y.; Zhang, L. N.; Osawa, M.; Cai, W. B., Surface-enhanced infrared spectroscopic study of a co-covered Pt electrode in room-temperature ionic liquid. *Journal of Physical Chemistry Letters* **2013**, *4* (10), 1582-1586.
- (99) Zhang, M.; Yu, L. J.; Huang, Y. F.; Yan, J. W.; Liu, G. K.; Wu, D. Y.; Tian, Z. Q.; Mao, B. W., Extending the shell-isolated nanoparticle-enhanced Raman spectroscopy approach to interfacial ionic liquids at single crystal electrode surfaces. *Chemical Communications* **2014**, *50* (94), 14740-14743.
- (100) Yuan, Y.-X.; Niu, T.-C.; Xu, M.-M.; Yao, J.-L.; Gu, R.-A., Probing the adsorption of methylimidazole at ionic liquids/Cu electrode interface by surface-enhanced Raman scattering spectroscopy. *Journal of Raman Spectroscopy* **2010**, *41* (5), 516-523.
- (101) Santos, V. O.; Alves, M. B.; Carvalho, M. S.; Suarez, P. A. Z.; Rubim, J. C., Surface-enhanced Raman scattering at the silver electrode/ionic liquid [Bmi][Pf₆] interface. *The Journal of Physical Chemistry B* **2006**, *110* (41), 20379-20385.
- (102) Baldelli, S., Surface structure at the ionic liquid-electrified metal interface. *Accounts of Chemical Research* **2008**, *41* (3), 421-431.
- (103) Baldelli, S., Probing electric fields at the ionic liquid-electrode interface using sum frequency generation spectroscopy and electrochemistry. *Journal of Physical Chemistry B* **2005**, *109* (27), 13049-13051.
-

- (104) Rivera-Rubero, S.; Baldelli, S., Surface spectroscopy of room-temperature ionic liquids on a platinum electrode: A sum frequency generation study. *Journal of Physical Chemistry B* **2004**, *108* (39), 15133-15140.
- (105) Zhou, W.; Inoue, S.; Iwahashi, T.; Kanai, K.; Seki, K.; Miyamae, T.; Kim, D.; Katayama, Y.; Ouchi, Y., Double layer structure and adsorption/desorption hysteresis of neat ionic liquid on Pt electrode surface - an in-situ IR-visible sum-frequency generation spectroscopic study. *Electrochemistry Communications* **2010**, *12* (5), 672-675.
- (106) Buchner, F.; Forster-Tonigold, K.; Uhl, B.; Alwast, D.; Wagner, N.; Farkhondeh, H.; Gross, A.; Behm, R. J., Toward the microscopic identification of anions and cations at the ionic liquid | Ag(111) interface: A combined experimental and theoretical investigation. *ACS Nano* **2013**, *7* (9), 7773-7784.
- (107) Atkin, R.; El Abedin, S. Z.; Hayes, R.; Gasparotto, L. H. S.; Borisenko, N.; Endres, F., AFM and STM studies on the surface interaction of [Bmp][TFSA] and [Emim][TFSA] ionic liquids with Au(111). *Journal of Physical Chemistry C* **2009**, *113* (30), 13266-13272.
- (108) Carstens, T.; Hayes, R.; El Abedin, S. Z.; Corr, B.; Webber, G. B.; Borisenko, N.; Atkin, R.; Endres, F., In situ STM, AFM and dts study of the interface 1-hexyl-3-methylimidazolium tris(pentafluoroethyl)trifluorophosphate/Au(111). *Electrochimica Acta* **2012**, *82*, 48-59.
- (109) Foulston, R.; Gangopadhyay, S.; Chiu, C.; Moriarty, P.; Jones, R. G., Mono and multi-layer adsorption of an ionic liquid on Au(110). *Physical Chemistry Chemical Physics* **2012**, *14* (17), 6054-6066.
- (110) Vatamanu, J.; Xing, L.; Li, W.; Bedrov, D., Influence of temperature on the capacitance of ionic liquid electrolytes on charged surfaces. *Physical Chemistry Chemical Physics* **2014**, *16* (11), 5174-5182.
- (111) Costa, R.; Pereira, C. M.; Silva, A. F., Structural ordering transitions in ionic liquids mixtures. *Electrochemistry Communications* **2015**, *57*, 10-13.
- (112) Bonta, M.; Anderl, T.; Cognigni, A.; Hejazifar, M.; Bica, K.; Limbeck, A., Determination of residual chloride content in ionic liquids using LA-ICP-MS. *RSC Advances* **2016**, *6*, 90273-90279.
- (113) Cheng, H.-W.; Stock, P.; Moeremans, B.; Baimpos, T.; Banquy, X.; Renner, F. U.; Valtiner, M., Characterizing the influence of water on charging and layering at electrified ionic-liquid/solid interfaces. *Advanced Materials Interfaces* **2015**, *2* (12), 1500159-n/a.
- (114) Figueiredo, M. C.; Ledezma-Yanez, I.; Koper, M. T. M., In situ spectroscopic study of CO₂ electroreduction at copper electrodes in acetonitrile. *ACS Catalysis* **2016**, *6* (4), 2382-2392.
- (115) Aranowski, R.; Cichowska-Kopczyńska, I.; Dębski, B.; Jasiński, P., Conductivity and viscosity changes of imidazolium ionic liquids induced by H₂O and CO₂. *Journal of Molecular Liquids* **2016**, *221*, 541-546.
- (116) Feng, G.; Jiang, X. K.; Qiao, R.; Kornyshev, A. A., Water in ionic liquids at electrified interfaces: The anatomy of electroadsorption. *ACS Nano* **2014**, *8* (11), 11685-11694.
- (117) Zhekenov, T.; Toksanbayev, N.; Kazakbayeva, Z.; Shah, D.; Mjalli, F. S., Formation of type iii deep eutectic solvents and effect of water on their intermolecular interactions. *Fluid Phase Equilibria* **2017**, *441*, 43-48.
- (118) Dai, Y.; Witkamp, G. J.; Verpoorte, R.; Choi, Y. H., Tailoring properties of natural deep eutectic solvents with water to facilitate their applications. *Food Chemistry* **2015**, *187*, 14-19.

-
- (119) Durand, E.; Lecomte, J.; Baréa, B.; Dubreucq, E.; Lortie, R.; Villeneuve, P., Evaluation of deep eutectic solvent-water binary mixtures for lipase-catalyzed lipophilization of phenolic acids. *Green Chemistry* **2013**, *15* (8), 2275-2282.
- (120) Sandoval, A. P.; Suarez-Herrera, M. F.; Feliu, J. M., Hydrogen redox reactions in 1-ethyl-2,3-dimethylimidazolium bis(trifluoromethylsulfonyl)imide on platinum single crystal electrodes. *Electrochemistry Communications* **2014**, *46*, 84-86.
- (121) Navarro-Suarez, A. M.; Hidalgo-Acosta, J. C.; Fadini, L.; Feliu, J. M.; Suarez-Herrera, M. F., Electrochemical oxidation of hydrogen on basal plane platinum electrodes in imidazolium ionic liquids. *Journal of Physical Chemistry C* **2011**, *115* (22), 11147-11155.
- (122) Hanc-Scherer, F. A.; Sanchez-Sanchez, C. M.; Ilea, P.; Herrero, E., Surface-sensitive electrooxidation of carbon monoxide in room temperature ionic liquids. *ACS Catalysis* **2013**, *3* (12), 2935-2938.
- (123) Hanc-Scherer, F. A.; Montiel, M. A.; Montiel, V.; Herrero, E.; Sanchez-Sanchez, C. M., Surface structured platinum electrodes for the electrochemical reduction of carbon dioxide in imidazolium based ionic liquids. *Physical Chemistry Chemical Physics* **2015**, *17* (37), 23909-23916.
- (124) Clavilier, J., The role of anion on the electrochemical behaviour of a {111} platinum surface; an unusual splitting of the voltammogram in the hydrogen region. *Journal of Electroanalytical Chemistry* **1979**, *107* (1), 211-216.

Chapter 3
Methods and
experimental protocol

Universitat d'Alacant
Universidad de Alicante

METHODS AND EXPERIMENTAL PROTOCOL

In this chapter, the main fundamentals of both the methodologies and the materials used in this thesis are explained in detail. At first, the chapter introduces the single crystal electrodes topic: their characterization, preparation and treatment. Then, the different strategies employed to prepare the materials and ensuring the reproducibility of the experiments are described. Next the chemicals were introduced. Particularly, the most relevant properties of the employed ILs are detailed. Finally, the different used in-situ and ex-situ characterization techniques are described, at first to analyse the properties of the interfacial region Metal|solution, and later to deeply investigate the metal deposits over the different conductive surfaces. Classical electrochemical techniques such as cyclic voltammetry and chronoamperometry are described in the context of the single crystal electrodes field and metal electrodeposition. Afterwards, more specific techniques to analyse the M(hkl)|solvent interface are described: CO displacement and laser induced temperature jump techniques. Before introducing these techniques, the main concepts of the classical electrified double layer region are briefly explained. Finally, the characterization techniques employed to analyse the metal deposits are introduced: Scanning Electron Microscopy, Electron Dispersive Spectroscopy, X-Ray Diffraction Spectroscopy and X-Ray Photoelectron Spectroscopy. These techniques provide morphological, chemical and structural information. Atomic Force Microscopy is also introduced due to the topographical and morphological information provided at low coverages.

3.1) Single crystal electrodes

3.1.1) Introduction

The use of single crystal electrodes is strongly recommended to study the interfacial properties of the Metal|solution interfaces. A single crystal electrode is a well orientated surface with a regular distribution of active sites. Single crystals are especially useful in electrocatalysis because many reactions involve the formation of intermediates that adsorb on specific sites of the surface. The adsorption energy of the intermediates is dependent on the geometry of the active site. A single crystal electrode relates the

interaction of a compound (ion, molecule...) in solution with a limited single type of active site. Thus, the obtained electrochemical response can be rationalized and quantified (in terms of charge) as a function of the electro-active area. This explains why single crystals electrodes are preferred rather than polycrystalline surfaces, since a polycrystalline material has several domains with different crystalline facets of variable area. The response provided by a polycrystalline surface is the average of all the facets contribution and the interactions between the neighbour parts in the polycrystalline surface can also influence the electrochemical response. Because of that, the replacement of the polycrystalline surfaces by well orientated electrodes has represented a development in the Surface Science field¹⁻³.

The study of single crystals was firstly focused on the coinage metals: Au, Ag or Cu. But later, during 80s, the attention moved to the platinum group metals: Pt, Ir, Pd or Rh⁴ after Clavilier developed the proper and clean strategies to clean platinum. These metals have in common that they crystallize in a face centred cubic crystal (fcc). This means that the unit cell, which is the minimum regular distribution of atoms that repeats periodically in the bulk network, is a cube where the atoms are located at the centre and vertices of the faces (fcc). Figure 3.1 shows the bulk metal structure and the atoms distribution in the unit cell.

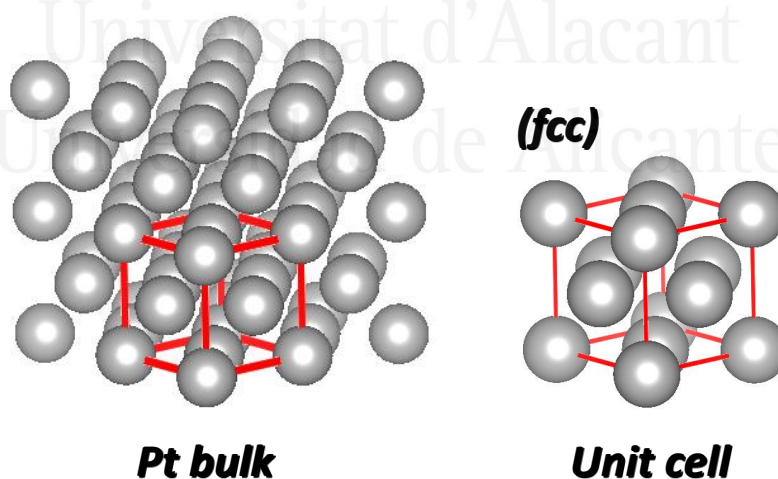


Figure 3.1: Pt bulk structure and unit cell.

Well-ordered surfaces in fcc metals are obtained by cutting the metal in a specific direction parallel to a crystallographic plane. In the crystal lattice this plane is defined by the Miller indices, three numbers: $\langle hkl \rangle$ which are proportional to the reciprocal values

of the a, b and c axes. These three axes intersect with the selected crystallographic plane. The vector $(1/a, 1/b, 1/c)$ is orthogonal to the plane, as the Figure 3.2 shows:

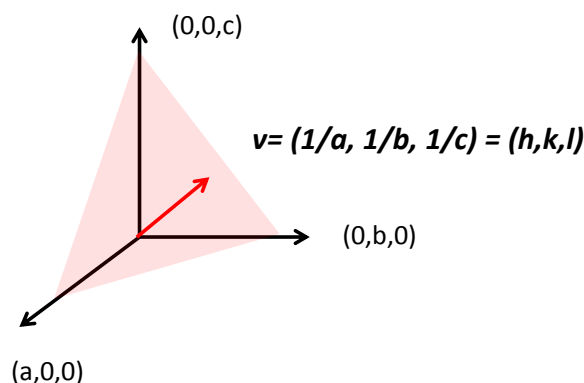


Figure 3.2: Scheme of the plane defined by the Miller index $\langle hkl \rangle$.

Miller numbers $(h\ k\ l)$ are the smallest integer proportional to $(1/a, 1/b, 1/c)$.

The most employed surfaces in Electrochemistry are the basal planes. Basal planes are the lowest-Miller index crystal faces. There are three basal planes notated as: $\langle 111 \rangle$, $\langle 100 \rangle$ and $\langle 110 \rangle$ and they can be obtained by cutting the metals along the planes showed below, (Figure 3.3). While the $\langle 111 \rangle$ and $\langle 100 \rangle$ orientations correspond to flat terraces, in the $\langle 110 \rangle$ orientation two planes of atoms are identified in the surface: on top (a) and below (b). In fact, the $\langle 110 \rangle$ orientations can be considered as a stepped surface of $\langle 111 \rangle$ terraces of 1 atom-row and $\langle 111 \rangle$ steps: $(111) \times (111)$. The $\langle 111 \rangle$ orientation contains the highest number of coordination ($n=9$), while in $\langle 100 \rangle$ the atoms are surrounded by 8 atoms and $\langle 110 \rangle$ is the most open structure, the atoms are coordinated by 6 atoms.

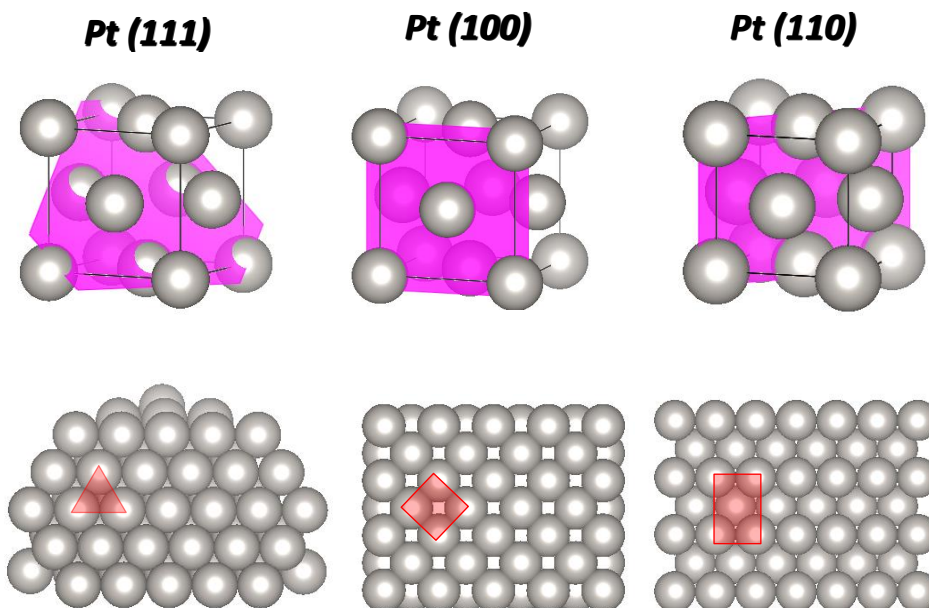


Figure 3.3: Pt basal planes and active side distribution of the corresponding orientations.

Nevertheless, in the practical sense a catalyst normally contains defects and different active sites. So, for a better approach to a real catalyst under controlled conditions, stepped surfaces are preferred. These surfaces are composed by n-atoms rows terraces separated by monoatomic steps (Figure 3.4):

$$M(hkl) = M(S)[n(h'k'l')x(h''k''l'')] \quad (3.1)$$

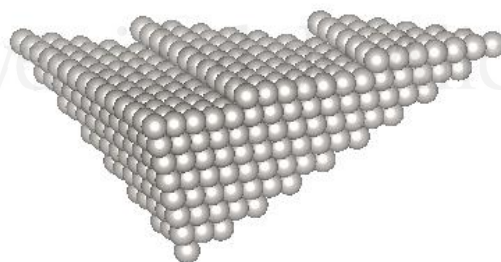


Figure 3.4: Stepped surface draw.

From an atomistic approach, it is possible to calculate the theoretical charge surface density related to any specific orientation and for a full monolayer ($\theta = 1$), i.e., by considering one transferred electron per one metallic atom. For that, the diameter of the metal (d) is required, value that is determined by X-Ray Diffraction⁵. Figure 3.5 shows the relation between the charge surface density of the basal planes and the geometry of the active site (d).

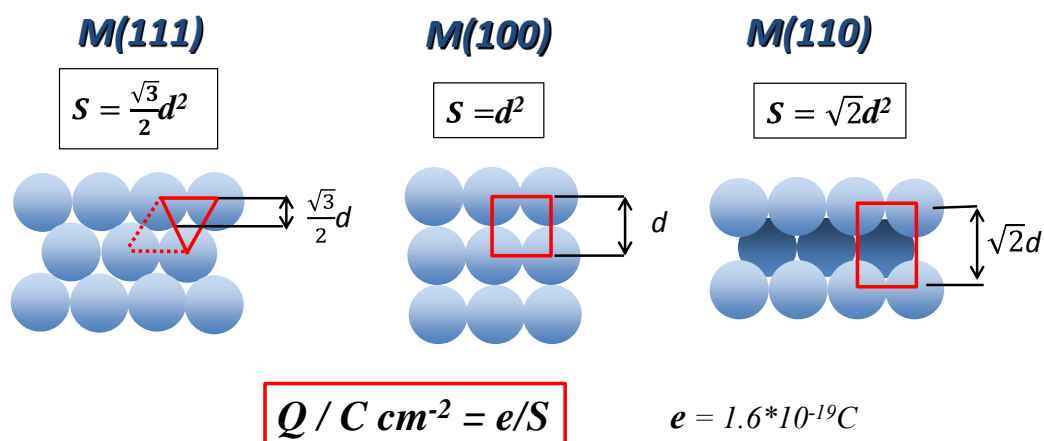


Figure 3.5: Atomic distribution of the basal planes with the corresponding electro-active areas.

The magnitude e/S in Figure 3.5 (the surface charge density value) is of paramount importance in surface science due to it relates the charge measurable value with the specific active site. So, preliminary information about the nature of the processes that take place on the surface, either capacitive or faradaic, is obtained by the charge value involved in the processes. Table 3.1 summarizes the e/S values for the basal planes of the employed metals: **Pt, Au and Ir**^{1, 2, 6-8}.

<i>Metal/ionic radius</i>	<i><hkl></i>	<i>e/S vs $\mu\text{C cm}^{-2}$</i>
Pt /r = 0.139 nm	<110>	150 $\mu\text{C cm}^{-2}$
	<100>	209 $\mu\text{C cm}^{-2}$
	<111>	240 $\mu\text{C cm}^{-2}$
Au /r = 0.144 nm	<110>	137 $\mu\text{C cm}^{-2}$
	<100>	193 $\mu\text{C cm}^{-2}$
	<111>	223 $\mu\text{C cm}^{-2}$
Ir /r = 0.136 nm	<110>	153 $\mu\text{C cm}^{-2}$
	<100>	217 $\mu\text{C cm}^{-2}$
	<111>	250 $\mu\text{C cm}^{-2}$

Table 3.1: e/S values for the $M(hkl)$ basal planes. $M = \text{Pt, Au or Ir}$. (from Vesta data bases)⁹.

3.1.2) $M(hkl)$ preparation

Pt(hkl) surfaces are prepared by taking a high pure Pt wire (99.995%) of 0.5 mm diameter exposed to a O_2 -fuel torch until melting slightly the ending part. The Pt wire is hold and fixed and the position of the torch is moved from the bottom to the top part of the melting bead. Since the melting point of the Pt is around $1769^\circ C$, the torch temperature is enough. During the process a small spherical bead of around 2.5 mm diameter is slowly grown. When the bead is cooled down, different crystallographic facets are formed, mainly $\langle 111 \rangle$ and $\langle 100 \rangle$ orientations.

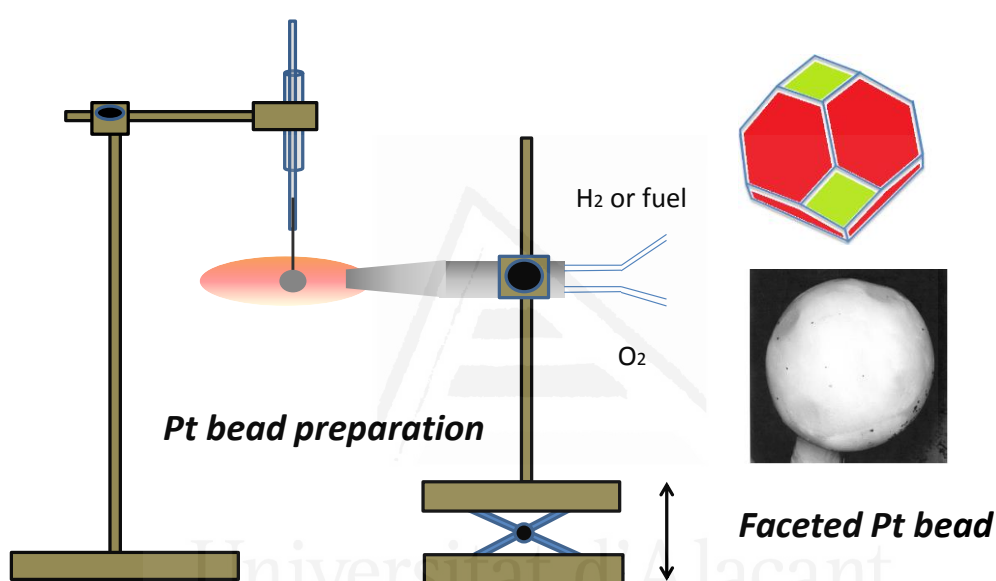


Figure 3.6: Scheme of the faceted bead preparation.

Then, the formed polycrystalline bead is positioned in the goniometer (Figure 3.6). The Pt bead is lighted with a laser beam which is reflected producing spots. The location of the spots in the screens depends on the crystallographic facet. The goniometer allows the measure of the angles between two spots. Comparing the measured angles to those expected for planes of a face-centred-cubic (fcc) lattice provides verification of the single crystal (Figure 3.7). Identified the crystallographic plane, the bead is mechanically polished with alumina or diamond paste. To ensure that the position of the bead is well-fixed in the goniometer, the metal bead is embedded in an epoxy resin. Later, this epoxy resin is removed with the proper organic solvent and flame-annealed in a fuel-air flame during 20 minutes.

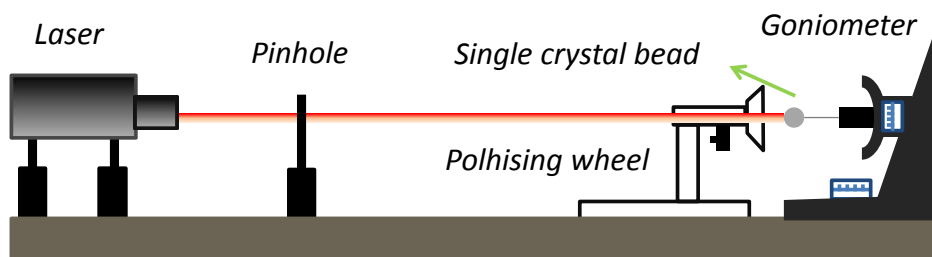


Figure 3.7: Single crystal preparation set-up.

This methodology is also employed for Au(hkl) single crystal preparation, although a lower temperature is needed to form the Au bead due to the Au melting point is 1063°C. Other metals such as Ir have a considerable high melting point. Moreover, Ir(hkl) electrodes are very oxophilic. So, for Ir preparation, the use of an inductive oven is highly recommended. Table 3.2 summarizes the melting point of these metals^{2,4}.

Metal	Melting point/°C
Ir	2443
Pt	1769
Au	1063

Table 3.2: Melting points of some of the metals employed in this thesis¹⁰.

3.1.3) Surface pre-treatment and characterization

3.1.3.1) Platinum single crystals, Pt(hkl)

There are innumerable compounds that adsorb on the platinum surface, i.e., platinum surfaces are easily poisoned. Nowadays, the most used methodology to pre-treat the Pt electrodes and keep the surface ordering was firstly proposed by Clavilier during 80s¹¹. The Clavilier's pre-treatment consists on: 1) flame annealing the electrode under a H₂/O₂ flame. The rise of the temperature also increases the surface mobility of the atoms and contributes to reach the atomic surface ordering. 2) Cooling down under a reductive atmosphere of H₂/Ar in a molar ratio 1:3 (approximately) to prevent both the surface contamination and oxidation. Platinum is oxophilic, i.e, it is easily oxidized by the atmospheric oxygen causing the appearance of defects sites, especially on Pt(100), Pt(110) and stepped surfaces. After flame-annealing, the electrode is quickly moved to a

glass recipient (ball) that contains ultra-pure water saturated with H_2/Ar . So, finally 3) the cold electrode is protected by a drop of water. The electrode (a Pt bead joined to a Pt wire), is fixed in a glass dipstick hold by a Teflon holder piece. This configuration allows moving the electrode up and down in order to perform the protection with water. Figure 3.8 shows a scheme of the platinum electrode flame-annealing and cooling down^{4, 8}.

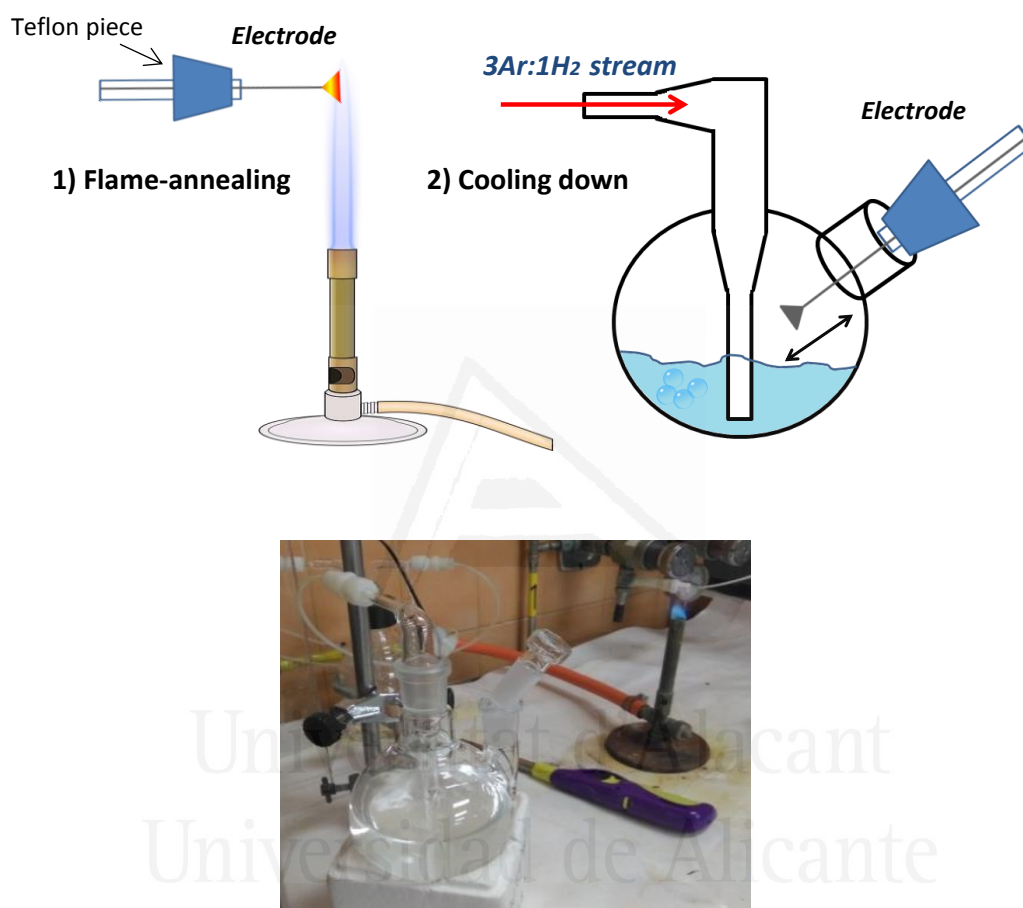


Figure 3.8: Scheme and picture of the Pt(hkl) pre-treatment set-up.

This surface cleaning procedure is simple and less expensive than the previous proposed methodologies involving vacuum techniques which, in addition, didn't avoid the introduction of contaminants either. The Clavilier's methodology was used to pre-treat the Pt(hkl) electrodes when the experiments were carried out in aqueous electrolytes. When the employed solvent was an Ionic Liquid (IL), ultrapure water was replaced by clean dried IL. The IL was also saturated by H_2/Ar and used to protect the electrode.

Cyclic voltammetry is the most convenient technique for both characterizing Pt(hkl) electrodes surfaces and evaluating the cleanness of the system. This technique is described in detail in section 3.4.1.1. Figure 3.9 displays the typical cyclic voltammograms recorded for Pt(111) in contact with two different aqueous electrolytes: 0.1M HClO₄ (red line) and 0.5M H₂SO₄ (black line).

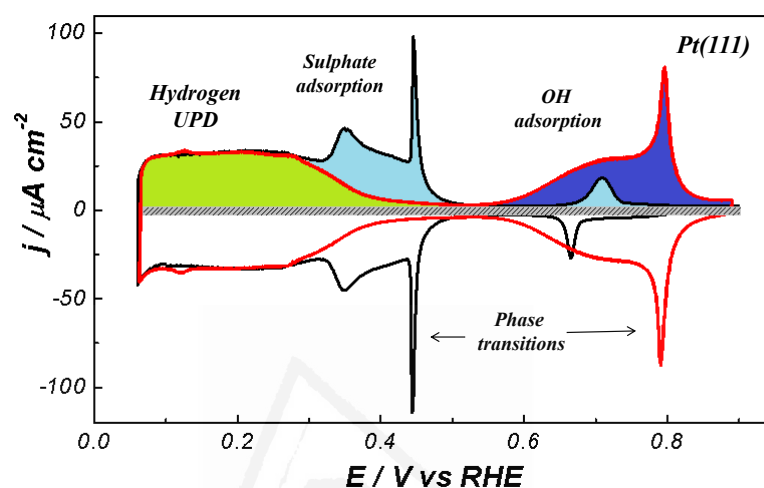


Figure 3.9: Cyclic voltammograms of: red line) Pt(111)/0.1M HClO₄ and black line) Pt(111)/0.5M H₂SO₄. Scan rate: 50mV/s.

The profile of the cyclic voltammogram shows that perchlorate anion (ClO₄⁻) does not adsorb or adsorbs weakly on Pt(111), and HSO₄⁻/SO₄²⁻ adsorbs specifically on the surface. The lowest potential region in the voltammogram (between 0.05-0.40V vs RHE) is determined by the hydrogen UPD region (Figure 3.9 green zone). The overall charge calculated after subtracting the capacitive current, approaches to 160 μC cm⁻², value that corresponds to 2/3 of surface coverage. In 0.5 M H₂SO₄ solution, the voltammogram displays a faradaic current up to 0.40V vs RHE which is suppressed around 0.55V vs RHE, showing the sulphate adsorption overlapped with the hydrogen desorption process. This result is later confirmed by the CO displacement technique (section 3.4.2.3), technique that provides relevant information about how the total charge reorganizes along the interfacial region, providing information about the nature of the species adsorbed on the surface.

In 0.1M HClO₄ solution, as perchlorate anions do not adsorb on the surface, the anion adsorption is attributed to hydroxide adsorption (from water dissociation). The hydroxide adsorption onset occurs at around 0.55V vs RHE, well separated from the hydrogen adsorption/desorption region by a narrow double layer region between 0.35-0.55V vs RHE. Using Pt(111), the voltammograms also display, in both electrolytes, sharp spikes. These spikes are typical features observed on single crystal surfaces and correspond to order-disorder phase transitions, mainly related with the anion adsorption. Cyclic voltammograms for M(hkl) substrates are the fingerprint of the M(hkl)|solution interface and reveal the influence of the specific nature of the electrolyte on the interfacial properties^{2, 6}. How the electrolyte (aqueous solution, DES, RTIL...) influences the M(hkl)|solution interfacial region will be one of the main focus in foregoing sections.

Figure 3.10 shows the cyclic voltammograms recorded for the three basal planes in contact with the two aqueous electrolytes, showing the surface sensitivity of the interfacial processes in the Pt(hkl)|solution region⁶.

In this thesis, Pt(111) was investigated in several aqueous electrolytes (at different pHs) and in ILs media.

Other methodology employed to pre-treat Pt(hkl) single crystal electrodes consists on covering the electrode with a carbon monoxide monolayer (CO). The Pt electrode is flame annealed and cooled down under a CO atmosphere. The CO adsorbs strongly on the surface and protects it while the electrode is moved to the cell. The corresponding set-up is similar to that showed in Figure 3.8, but the H₂/Ar flow is replaced by a CO stream. In this case, the protection with a drop of water is not necessary since the CO avoids that other species adsorb on the surface. Afterwards, the CO is electrochemically oxidized to CO₂ leading the surface free and clean, displaying the typical voltammetric features for the Pt(hkl) (Figure 3.11)¹²:

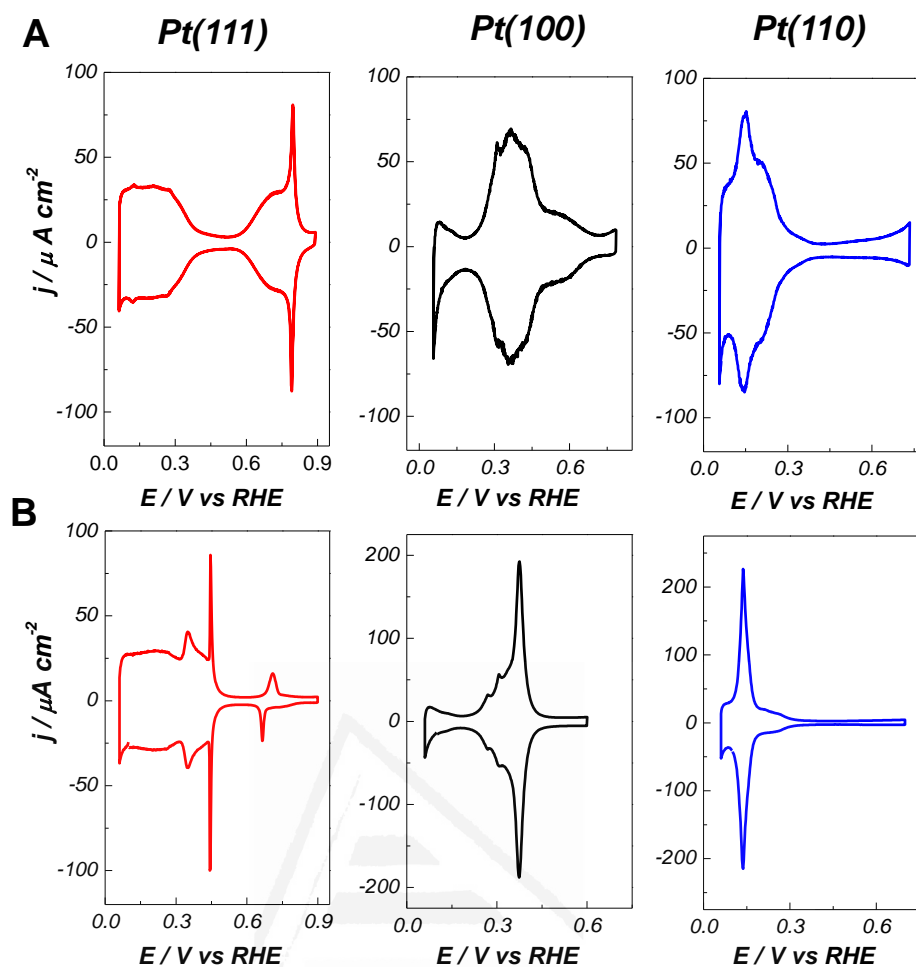


Figure 3.10: Cyclic voltammograms of Pt(hkl) in contact with: A) 0.1M HClO₄ and B) 0.5M H₂SO₄ solutions. Scan rate: 50mV/s.

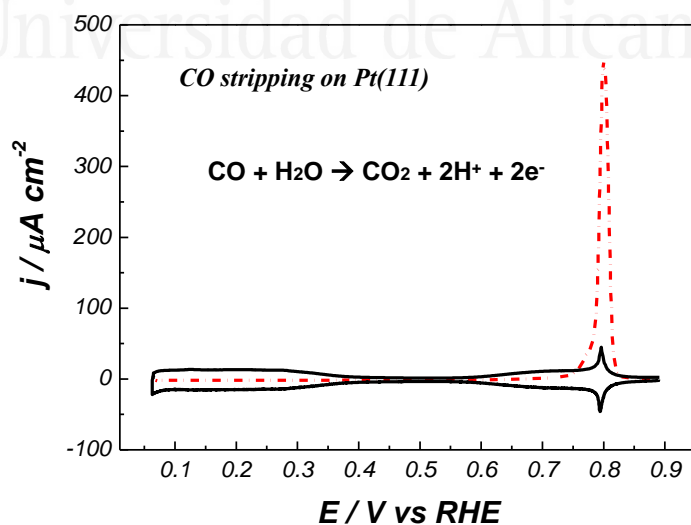
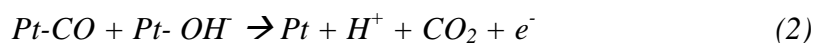
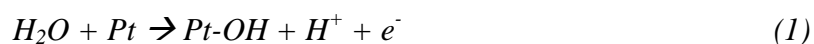


Figure 3.11: Cyclic voltammograms of CO stripping (red dashed line) on Pt(111) and of Pt(111)|0.1M HClO₄ interface (black line). Scan rate: 20mV/s.

The CO pre-treatment avoid introducing water to the cell because of the electrode does not require the water drop protection, methodology desirable when the electrolyte was an ionic liquid.

The proposed CO oxidation mechanism in aqueous electrolytes is as follows ¹:



ILs always contains a small fraction of interfacial water which is hardly to remove. Some authors have demonstrated that the CO oxidation mechanism in IL involves this interfacial water. In this thesis, CO oxidation on Pt(111) in contact with both [Emmim][Tf₂N] and the DES was studied as a way to protect Pt(hkl) in IL media¹³⁻¹⁵.

3.1.3.2) Ir(hkl) single crystals

The Ir(hkl) single crystal surfaces pre-treatment also involves thermal treatment under reductive atmosphere such as H₂/Ar. CO protection on Ir surfaces can be also carried out. The set-up required to perform the surface treatment is different than the previous one showed in Figure 3.8. To pre-treat Ir electrodes, the glass ball must be replaced by a system that allows both the annealing and the cooling down steps under inert atmosphere in order to prevent the Ir surface oxidation. For that, the electrode was kept in a quartz tube that has an inlet and output part (Figure 3.12). Constant Ar/H₂ gas stream flows through the quartz tube to ensure whole deoxygenation. The tube also contains ultrapure water saturated with Ar/H₂. The annealing of the electrode was performed inside the tube by using an induction furnace. For that, the quartz tube was positioned within an induction coil. Then, the working electrode is kept at the height of this coil. The inductive coil was connected to a power supply. The increase of the temperature in the metal disk was carried by electromagnetic induction. In this case, for the Ir surface flame annealing, the temperature usually ranges between 1600-1900°C. Finally, the electrode is cooled down under the inert atmosphere and protected by a drop of water¹⁶.

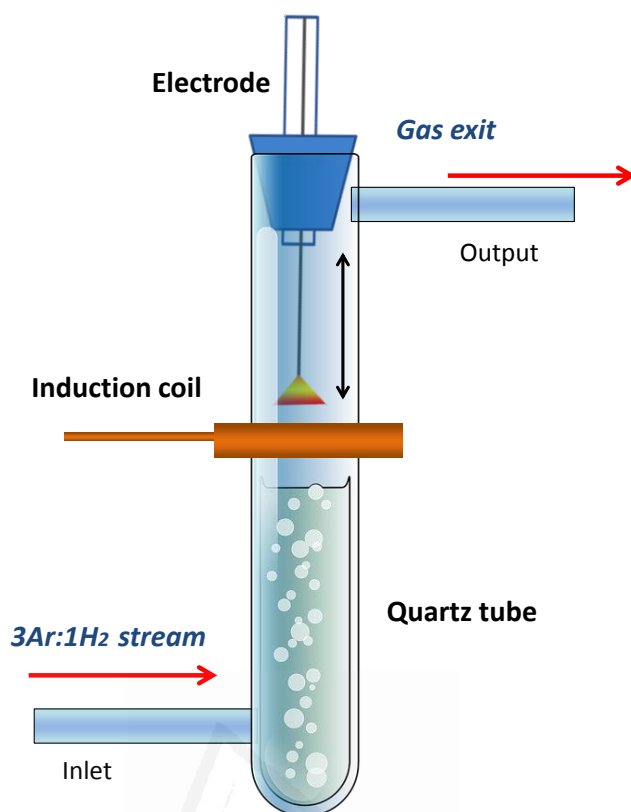


Figure 3.12: Scheme of the $Ir(hkl)$ pre-treatment set-up, showing the quartz tube and induction coil.

3.1.3.3) $Au(hkl)$ single crystals

The pre-treatment of the $Au(hkl)$ electrodes is easier than the previous ones. Gold is considerably less sensitive to oxygen than Pt or Ir, and then it can be flame-annealed and cooled down in air without affecting dramatically the surface ordering. When the electrolyte is an aqueous solution, the electrode is usually flame-annealed and sometimes quenched in ultra-pure water to prevent from surface poisoning.

Sulphuric acid is one of the typically employed electrolytes to characterize Au single surfaces. Figure 3.13 contains the characteristic cyclic voltammograms of $Au(111)$ and $Au(100)$ in 0.5M H_2SO_4 solution.

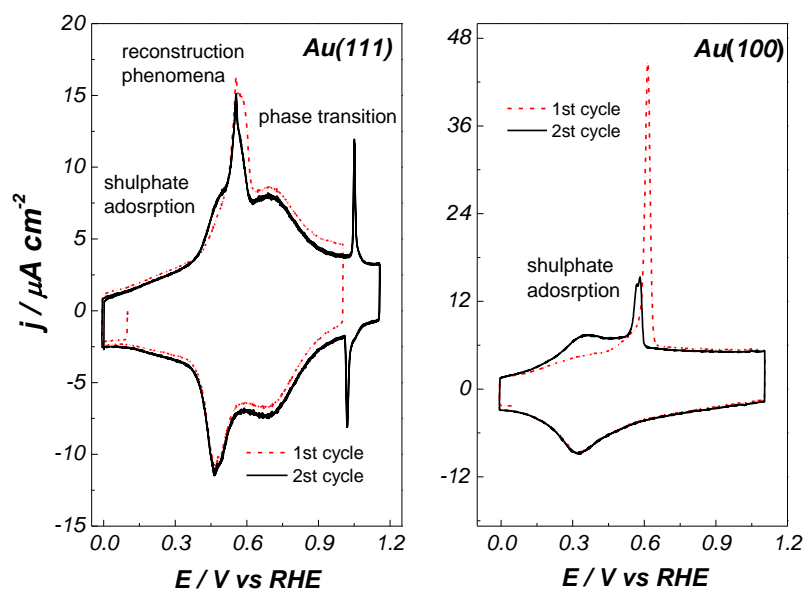


Figure 3.13: Cyclic voltammograms of Au(hkl)/0.5M H₂SO₄. Scan rate: 50mV/s.

Au is a polarizable electrode, non-catalytic to the hydrogen evolution and then no hydrogen UPD region is observed in the voltammetric window. Instead of that, a capacitive region is recorded, which profile shows surface sensitivity. Both cyclic voltammograms show a prominent feature which changes by successively cycling, feature centred at 0.50V vs RHE on Au(111), and at 0.60V vs RHE on Au(100). This feature is related with a phenomenon known as *surface reconstruction*. The reconstruction phenomenon consists on a redistribution of the surface atoms that leads a more packed configuration than the expected from the (fcc) crystallographic geometry. This arrangement is driven in order to lowering the surface energy, and it is favoured by thermic treatment related to increase of the atomic mobility. The reconstruction phenomenon is hindered when the anion is adsorbed specifically on the surface. The anion adsorption supplies charge density thus forcing the rearrangement of the atoms to accommodate the new energetic surface state, i.e., the anion adsorption eliminates the reconstructed form¹⁷.

Sometimes, the voltammetric feature related with the reconstruction elimination is followed by a sharp spike. This sharp spike, similar to those recorded on Pt(hkl) surfaces (Figure 3.10), is related to phase transition involving the anion structuration. The potential location of this feature is dependent on both the surface orientation and the anion nature. In this line, Au(hkl) surfaces are suitable electrodes to explore new

interfaces involving novel solvents (ILs) because the Au(hkl) is polarizable and the cyclic voltammograms are expected to be sensitive to the species of the solvent^{18, 19}. In this thesis, Au(hkl) were deeply investigated in both [Emmim][Tf₂N] and DES.

Figure 3.14 shows, the reconstructed and unreconstructed configurations for the three basal planes:

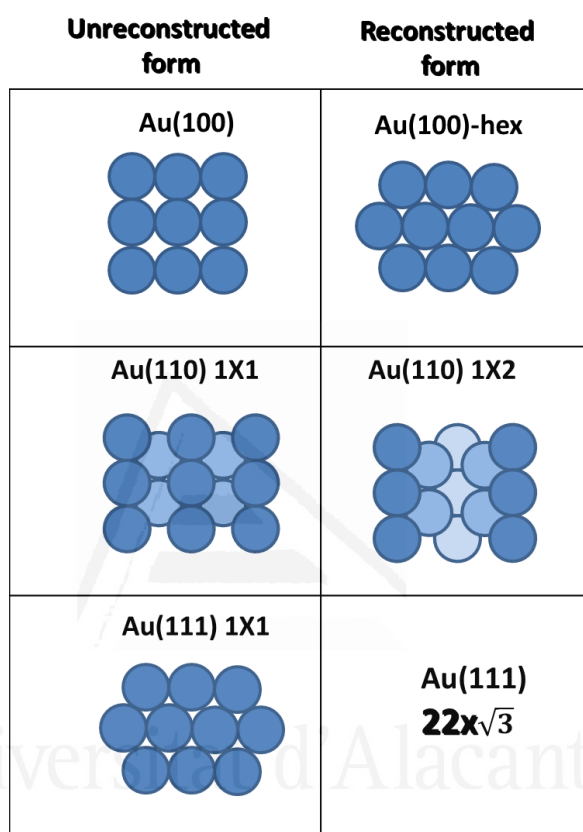


Figure 3.14: Atomistic models of the reconstructed and unreconstructed forms on Au(hkl).

3.1.3.4) Non-metallic surfaces. Glassy carbon

Glassy carbon is a carbon form electrode commonly used in Electrochemistry. Glassy carbon is an active surface slightly sensitive to organic contamination, but considerable less sensitive than the previous mentioned metallic surfaces. It is considered as a polarizable electrode displaying a wider electrochemical window. Kinetics of the reactions are usually slow. Blank cyclic voltammograms recorded on glassy carbon electrode display usually low capacitive currents without characteristic features unlike M(hkl) electrodes. In the field of the metal electrodeposition, glassy carbon is used to

evaluate nucleation and growth mechanisms due to weak interaction with the metal precursor, favouring the nucleation study. The bulk structure of glassy carbon is amorphous. The main benefits of glassy carbon as electrode are: resistance to high temperature, low density (1.5g/cm^3), good resistance to etching by acids or bases and good conductivity. On the other hand, glassy carbon shows both fragility and hardness that complicates their handling and limits the production to small shapes. One of these typical shapes is the rod form, (Figure 3.15). Glassy carbon rods of 2 mm diameter were employed to analyse the mechanism of the electrodeposition of several species (Ag(I), Cu(I), Cu(II) and Ni(II)) in both aqueous and IL media^{3, 20}. The electrode was mechanically polished until mirror finishing, using alumina powder of two grades: 3.75 and $1.87\ \mu\text{m}$ respectively.



Figure 3.15: glassy carbon rod.

3.2) Glassware cleaning

To avoid any source of contamination and ensure the reproducibility of the experiments, glassware (electrochemical cell) is exhaustively cleaned. Different cleaning procedures are used depending on the objective. One of these procedures, and the most employed in this thesis, uses an acidic solution saturated with potassium permanganate (KMnO_4 + few drops of H_2SO_4) (Figure 3.16). The cleaning procedure involves the following steps:

- 1) The glassware is kept inside KMnO_4 + H_2SO_4 solution overnight. The organic materia is oxidized by the permanganate solution, producing MnO_2 waste in the following reaction: $\text{C}_x\text{H}_y\text{O}_z + \text{MnO}_4^- \rightarrow \text{Mn(II)} + -\text{ne}^- + \text{CO}_2\dots$

- 2) After 24 hours, the permanganate solution is removed and the glassware is rinsed with a $\text{H}_2\text{O}_2 + \text{H}_2\text{SO}_4$ solution to reduce MnO_2 traces to soluble Mn(II) .
- 3) The glassware is successively rinsed and boiled with ultra-pure water (2-4 times). Boiling with water has two functions: at first, removing more easily the remaining organic contamination by thermic stirring. Secondly, dissolving the traces of anions such as SO_4^{2-} that can adsorb specifically on the surface.



Figure 3.16: glassware kept in a permanganate solution.

Other acids and oxidizing agents used to clean the glassware are:

-Piranha: a mixture solution between $\text{H}_2\text{O}_2 + \text{H}_2\text{SO}_4$ in the molar ratio of 1:3 approximately.

- HNO_3 solution. This methodology is suitable when ionic liquids are studied since the HNO_3 (aq) helps to dissolve relatively well some RTILs.

-Chromic solution: a solution containing $\text{K}_2\text{CrO}_4 + \text{H}_2\text{SO}_4$.

3.3) Chemicals

3.3.1) Properties of the $[\text{Emmim}][\text{Tf}_2\text{N}]$ and ChCl:urea DES

The employed RTIL was the 1-ethyl-2,3-dimethylimidazolium bis(trifluoromethylsulfonyl)imide: $[\text{Emmim}][\text{Tf}_2\text{N}]$. The election of this ionic liquid is related with the methylation of the second position in the imidazolium ring (Figure 2.2, chapter 2). Table 3.3²¹⁻²⁴ shows the main physical and chemical properties of $[\text{Emmim}][\text{Tf}_2\text{N}]$, joint to the properties of $[\text{Bmmim}][\text{Tf}_2\text{N}]$ and $[\text{Emim}][\text{Tf}_2\text{N}]$ for comparison. Although the former one has the C2 position methylated, it contains a longer

alkyl chain (Bu) in C3 that introduces asymmetry in the cation structure and increases the van der Waals interactions. In [Emim][Tf₂N], the proton in C2 favours the hydrogen bond interactions in addition to the coulombic forces:

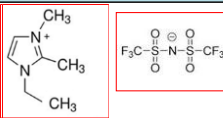
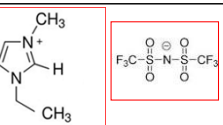
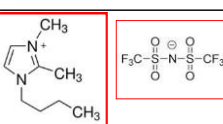
<i>RTIL</i>	<i>T_m/°C</i>	<i>d/gmL⁻¹ (25°C)</i>	<i>Viscosity/mPas (25°C)</i>	<i>Conductivity/mScm⁻¹ (25°C)</i>
 [Emmim][Tf₂N]	20°C	1.49	88	3.2
 [Emim][Tf₂N]	3°C	1.56	34	6.66
 [Bmmim][Tf₂N]	15-20°C	1.41	118	1.94

Table 3.3: Properties of some ionic liquids based on the [Tf₂N]⁻ anion.

The main properties of the employed DES are summarized in Table 3.4. The choline chloride (ChCl)/urea DES (molar ratio 1ChCl:2urea) is liquid at room temperature, shows intrinsic conductivity but lower than RTILs likely because of its considerable higher viscosity. To deal with this, higher temperatures are required when the DES was used (40-70°C)²⁵.

<i>salt</i>	<i>T_f (salt)/°C</i>	<i>Bond proton donor (bdp)</i>	<i>T_f(bdp)/°C</i>	<i>Molar rate</i>
Choline Chloride	303	Urea	134	1ChCl 2Urea
Properties of the ChCl:Urea				
<i>T_m / °C</i>	<i>d/gmL⁻¹ (25°C)</i>	<i>Viscosity / mPas (25°C)</i>	<i>Conductivity / mScm⁻¹ (25°C)</i>	
12	1.24	632	0.74	

Table 3.4: Properties of the ChCl:urea DES.

3.3.2) Purification of ILs. Kolb's procedure

The purification of the RTIL is of paramount importance for the success of the experiments because little amount of impurities changes dramatically the properties of the Metal|RTIL interface. Literature provides several strategies to purify the RTILs and all of them involve a drying step. In the present thesis, the employed procedure is based on the Kolb's method. The methodology involves a vacuum step and the use of both temperature and molecular sieves²⁶(Figure 3.17):

1) The RTIL is introduced in a 25mL glass ball connected to a vacuum pump. The RTIL is kept under vacuum and stirring conditions at 80°C during 5 hours. This step removes most of the water content in the RTIL bulk.

2) Afterwards, the vacuum is broken using dried Ar gas.

3) Activated molecular sieves of 3Å were added. (400 mg per 1mL) and vacuum and temperature were again applied, during at least 24 hours more.

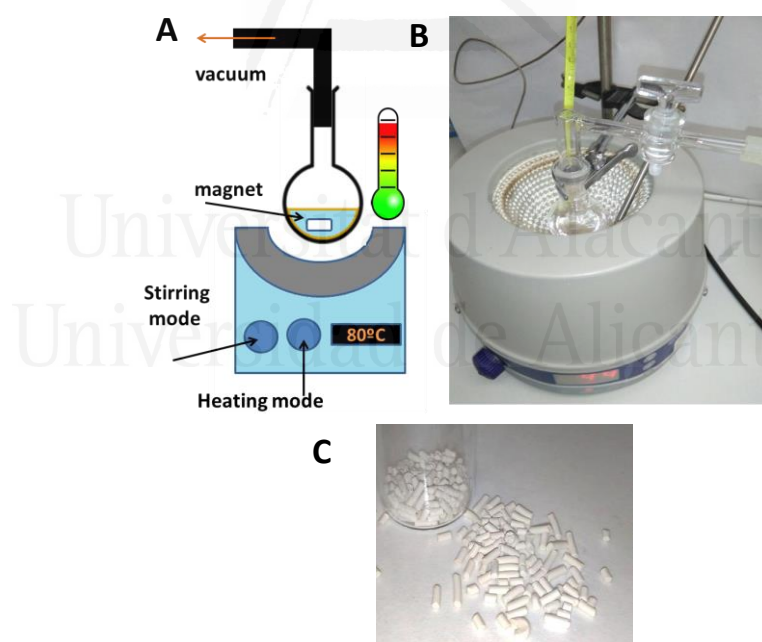


Figure 3.17: Purification set- up A) scheme and B) picture C) molecular sieves.

After the process, the water content measured with Karl Fischer titration ranged between 5-100 ppm of water.

Purification of the DES was performed using the same procedure but under lower temperature (50°C) and without molecular sieves. The water content was around 1%, considerable higher than in the RTIL.

3.3.3) Metal solution preparation

The solutions of metallic ions in ILs were prepared after drying the salts in an oven at $T > 100^\circ\text{C}$. The necessary amount of salt was added to the ionic liquid and the solution was stirred under vacuum conditions during the sufficient time to ensure salt dissolution.

3.3.4) List of reactants and metal solution preparation

Ionic liquids	
<i>1-Ethyl-2,3-dimethylimidazolium bis(trifluoromethylsulfonyl)imide [Emmim][Tf₂N]</i>	<i>Iolitec, 99%, liquid,</i>
<i>Choline Chloride ChCl</i>	<i>Acros organics, solid, 99% grade,</i>
<i>Urea</i>	<i>Merck, for analysis, solid</i>
Metal salts	
<i>Copper (II) chloride dihydrated CuCl₂*H₂O</i>	<i>Merck, for analysis</i>
<i>Copper(I) chloride anhydrous CuCl</i>	<i>Merck, for analysis</i>
<i>Silver nitrate AgNO₃</i>	<i>Panreac, for analysis</i>
<i>Nickel(II) chloride exahydrate NiCl₂*6H₂O</i>	<i>Merck, for analysis</i>
<i>Nickel(II) bis(trifluoromethylsulfonyl)imide Ni[Tf₂N]₂</i>	<i>Alfa Aesar, 98% grade</i>
Electrolytes preparation	
<i>Perchloric acid suprapur HClO₄</i>	<i>Suprapur, Merck, aqueous solution, wt 70%,</i>
<i>Sulphuric acid suprapur H₂SO₄</i>	<i>Suprapur, Merck, aqueous solution, wt 96%,</i>
<i>Potassium perchlorate KClO₄</i>	<i>Merck, Suprapur</i>

Sodium perchlorate NaClO_4	Merck, pro analysis
Sodium fluoride NaF	Merck, 99.99% grade
Sodium chloride NaCl	Merck, pro analysis
Metal solution preparation	
Ag(I)	1) $10^{-3}\text{M AgNO}_3 + 0.6\text{M NaClO}_4$ 2) $10^{-3}\text{M AgNO}_3 + 3\text{M NaCl aq (25}^\circ\text{C)}$ 3) $0.05\text{M AgNO}_3 + \text{DES (70}^\circ\text{C)}$
Cu(II)	1) $0.01\text{M CuCl}_2 + 3\text{M NaCl aq (25}^\circ\text{C)}$ 2) $0.05\text{M CuCl}_2 + \text{DES (40}^\circ\text{C or 70}^\circ\text{C)}$
Cu(I)	1) $0.01\text{M CuCl} + 3\text{M NaCl aq (25}^\circ\text{C)}$ 2) $0.05\text{M CuCl} + \text{DES (40}^\circ\text{C - 70}^\circ\text{C)}$
Ni(II)	1) $0.1\text{M NiCl}_2 + \text{DES (70}^\circ\text{C)}$ 2) $0.05\text{M Ni}[\text{Tf}_2\text{N}]_2 + [\text{Emmim}][\text{Tf}_2\text{N}]$ (T falta)

Table 3.5: Chemicals employed in this thesis.

3.4) In-situ techniques

3.4.1) Classical electrochemical techniques

3.4.1.1) Cyclic Voltammetry

The cyclic voltammetry (CV)³ technique is one of the most employed techniques in Electrochemistry. The CV basically performs a potential scan between two potential limits [E_{min} , E_{max}].

$$E_{ap} = E_i - v * t \text{ (signal)} \quad (3.2)$$

where v is the scan rate (V/s) and E_i is the initial potential (Figure 3.18A). The magnitude measured is the current density as a function of applied potential (Figure 3.18B).

A potentiostat-galvanostat and a three-electrodes cell were employed to carry out the cyclic voltammograms (Figure 3.18C). The electrodes are: working, counter and reference electrode. The reference electrode is sometimes kept in a Luggin capillary filled with the blank electrolyte. A gas bubbler was necessarily introduced in the cell in order to ensure inert atmosphere.

The profile of the cyclic voltammograms depends on both the surface (nature and geometry of the working electrode) and the electrolyte. CV profiles are also sensitive to the presence of pollutants and allow testing the quality of the solution. Due to the simplicity of the technique, CV is usually employed to carry the first basic electrochemical study. It provides preliminary information about the kinetics of the redox processes that take place.

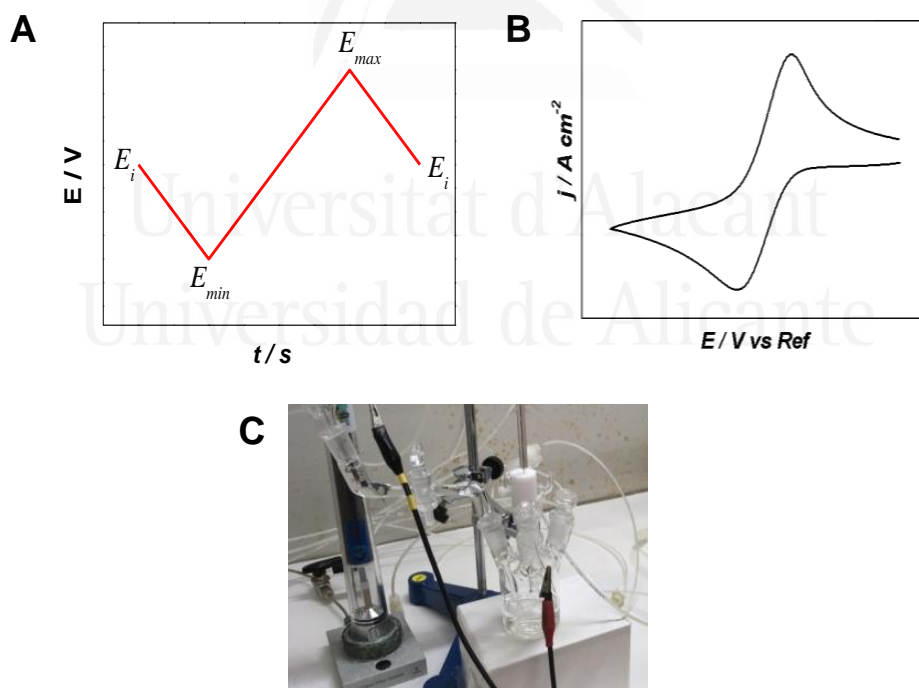


Figure 3.18: Cyclic Voltammetry technique. A) Signal E vs t . B) Cyclic voltammogram and C) Three electrode cell.

The current density recorded contains always a capacitive component and sometimes a faradaic contribution. The capacitive current is proportional to the scan rate and then is minimized at lower scan rates:

$$j_t = j_c + j_f = C_d * v + j_f \quad (3.3)$$

where C_d is the capacitance value, v is the scan rate and j_c and j_f are the faradaic and capacitive contributions to the current density respectively.

How j_f varies with the parameters that define the CV (v , E_{ap}) depends on the nature of the faradaic process. This faradaic contribution can account different overlapped processes depending on the complexity of the reaction mechanism. The reactions can be kinetically limited (electron transfer hindered) or mass transport limited. In this study, voltammetries were performed on planar electrodes.

Redox reactions can be reversible or non-reversible. A reversible reaction can transfer easily the electron and is governed by the Nernst equation.



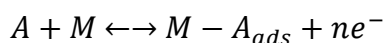
$$\frac{[O]}{[R]} = \exp\left[\frac{nF}{RT} (E - E^0)\right] \quad (3.4)$$

In the case of outer sphere reactions, the CV displays two peaks. The separation between them is close to 59mV, (Figure 3.19A). The variation of the current density peak (j_p) depends on the square root of the scan rate as follows:

$$j_p = -2.69 * 10^5 * n^{\frac{3}{2}} D_0^{\frac{1}{2}} * [O]_{bulk} * v^{1/2} \quad (3.5)$$

where n is the number of transferred electrons, D_0 is the diffusion coefficient and $[O]_{bulk}$ is the reactant concentration in bulk solution.

If the redox process is a reversible adsorption, Frumkin isotherm is used to describe the phenomenon (Langmuir isotherm when the lateral adsorbates interactions are negligible).



$$(Frumkin) \frac{\theta}{\theta - 1} = K C \exp\left(\frac{EF - \omega\theta}{RT}\right) \quad (3.6)$$

where C is the pseudocapacitance that corresponds to $C = q_{monolayer} \left(\frac{\partial \theta}{\partial E} \right)$ and K is the constant equilibrium $K = \exp\left(-\frac{\Delta G^0}{RT}\right)$, θ is the surface coverage of the species [O]. In the Frumkin isotherm, ω is a measure of the lateral interactions of the adlayers and can be positive (repulsion interactions) or negative (attractive interaction).

The CV is symmetric to the E axis and j_p depends proportionally on the scan rate. Other parameter to take into account is the width of the half height that is dependent on the lateral interactions ($90.3/n$ mV for a Langmuir isotherm). See Figure 3.19B for the details.

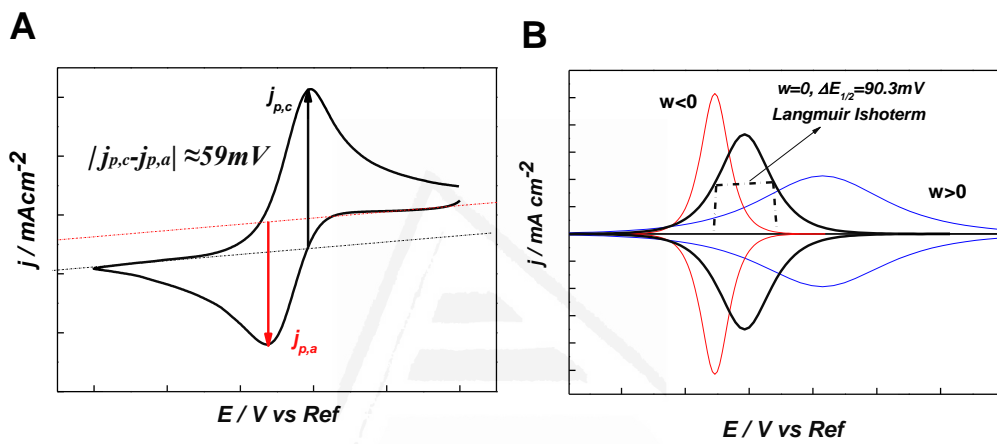


Figure 3.19: Cyclic voltammograms of: A) Outer sphere redox process. B) Specific adsorption.

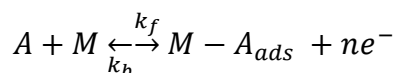
Non-reversible reactions are those reactions that show kinetic limitations. One of the most characteristic voltammetric features for these processes is that the current peak separation is higher than in a reversible redox reaction, either in outer sphere or adsorption processes. In addition, this peak separation tends to increase by increasing the scan rate due to the kinetic limitation in the electron transfer (Figure 3.20).

For outer sphere reactions, the kinetic condition is introduced with Butler-Volmer equation:

$$O + ne^- \xrightleftharpoons[k_b]{k_f} R$$

$$j = F * k_0 [[O](0, t) e^{-\frac{\alpha n F * [E - E^0]}{RT}} - [R](0, t) e^{\frac{(1 - \alpha) n F * [E - E^0]}{RT}}] \quad (3.7)$$

For irreversible adsorption processes the $j(E)$ equation is as follows:



$$j = q_{ML} \left(\frac{d\theta}{dt} \right) = q_{ML} [k_f [A] (1-\theta) e^{\left((E-E^0) \frac{\alpha n F}{RT} - (\beta-1) \frac{\omega \theta}{RT} \right)} - k_b \theta e^{\left(-(E-E^0) \frac{(1-\alpha) n F}{RT} + \beta \frac{\omega \theta}{RT} \right)}] \quad (3.8)$$

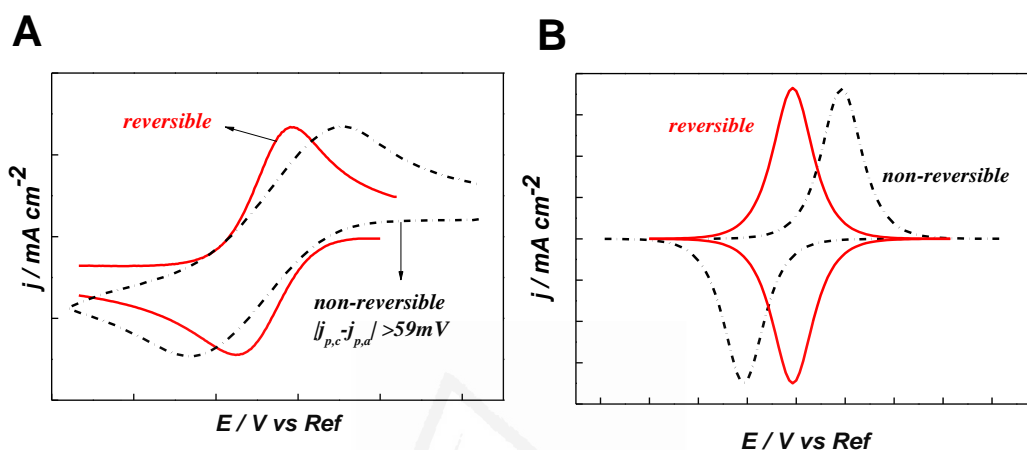


Figure 3.20: Cyclic voltammograms for reversible (red solid line) and non-reversible redox processes (black dashed line): A) Outer sphere redox process. B) Specific adsorption.

Cyclic voltammetry is also the most commonly employed technique in electrodeposition field. Voltammetric measures are easy to carry and provide valuable and preliminary information about the metal deposition mechanism. Voltammetric profiles of the metal deposition process are irreversible and not symmetric to potential axis. The deposition of a metal is a complex process that involves several steps: nucleation, formation of a new crystallographic phase, electron transfer and possible diffusion of the species. Depending on which the limiting step is, the voltammetric profiles are different in the cathodic branch. The anodic branch corresponds to the stripping/oxidation of the deposited metal and depends on the metal oxidation kinetics and efficiency. Oxidation scan can display a sharp peak whether the metal is easily oxidized, or a broad band with lower current if surface passivation occurs. In some cases, even no current is recorded in the oxidation scan if deposited species are non-oxidized.

Figure 3.21 shows voltammetric profiles recorded in metal electrodeposition. One typical voltammetric feature that appears after reversing the scan at low overpotentials limits is the voltammetric nucleation loop, (Figure 3.21A blue line). This voltammetric feature appears when a metal is deposited on a surface which interacts weakly with the metal precursor (for instance, on glassy carbon substrates). At the beginning, an extra overpotential is needed to force the formation of the first stable nucleus, that are the seeds over the deposit will grow. The appearance of the voltammetric loop is the evidence that metal nucleates and later grows, following a nucleation and growth mechanism. If the interaction of the metal precursor and the surface is favoured, no loop is observed in the reverse scan, being the overpotential needed to carry out the metal deposition lower. This behaviour is typical when the metal deposition on metallic surfaces takes place due to the strong metal_{substrate}-metal_{precursor} interaction (Figure 3.21B).

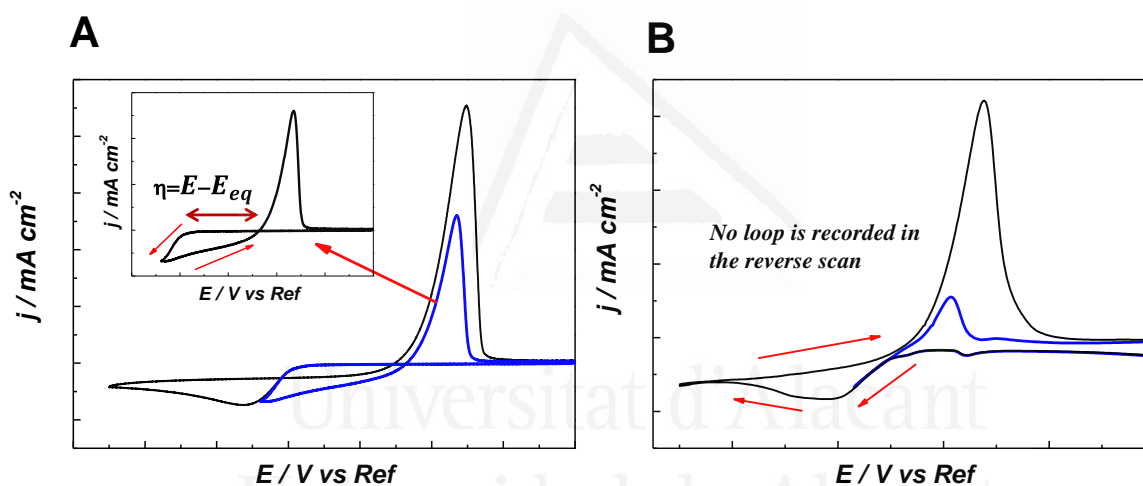


Figure 3.21: Cyclic voltammograms of metal deposition A) weak substrate-metal precursor interaction. Inset) nucleation loop. B) Strong substrate-metal precursor interaction.

When monolayer formation precedes the metal bulk deposition, underpotential deposition (UPD) takes place. UPD is reversible and usually displays sharp surface sensitive peaks revealing a phase transition of the metal adsorbed or co-adsorbed with the anion (Figure 3.22).

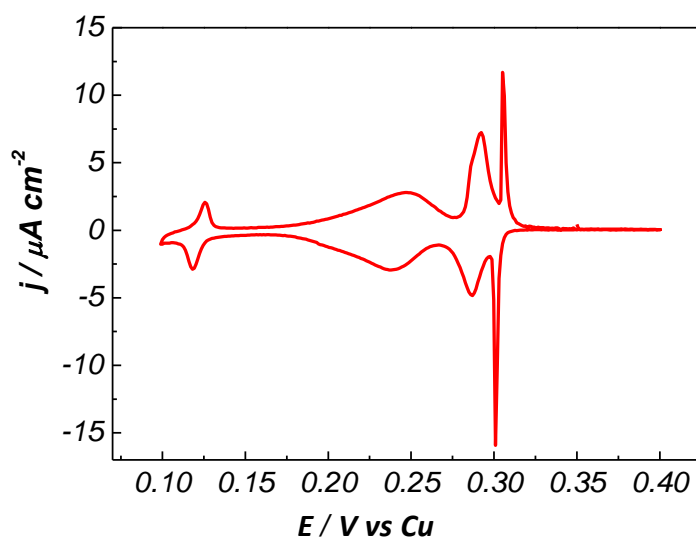


Figure 3.22: Cu UPD on Au(111) in 0.5M H_2SO_4 Solution. Scan rate: 10mV/s.

3.4.1.2) Potential step techniques. Chronoamperometry

The chronoamperometric technique³ measures the change in the current density with time after applying a constant potential value (Figure 3.23A). The faradaic current density overlaps with the double layer charging. However, the double layer current contribution decays quickly during around the first 50 μ s, being negligible at longer times. To get deep information about the double layer restructuration, the time scale should be lower, within the microsecond (μ s) scale. Laser induced temperature jump technique provides a response in the microsecond scale related with the double layer restructuration. This technique will be explained in detail in section 3.4.2.4.

Chronoamperometric j-t transients display several profiles depending on the nature of the redox process. The present thesis has employed potential step techniques to analyse the j-t transients recorded during the metal electrodeposition. In metal electrodeposition, chronoamperometry is also used to analyse nucleation and growth mechanism. Figure 3.23C shows the typical j-t transient profile obtained for metal deposition under 3D nucleation and growth mechanism diffusion controlled. At first, the current rises suddenly until attaining a maximum current peak. The formed nucleus grows radially (spherical geometry) until they overlap. Then the electrode behaves as a planar electrode and the current decays by linear diffusion, following the Cottrell equation:

$$j = \frac{n \cdot F \cdot c_{bulk} \cdot D^{0.5}}{(\pi \cdot t)^{0.5}} \quad (3.9)$$

where n is the number of transferred electrons, F is the Faraday constant, c_{bulk} is the bulk concentration and D is the diffusion coefficient (Figure 3.24).

By combination of different steps the process could be analysed in sequential way (Figures 3.23B and D)

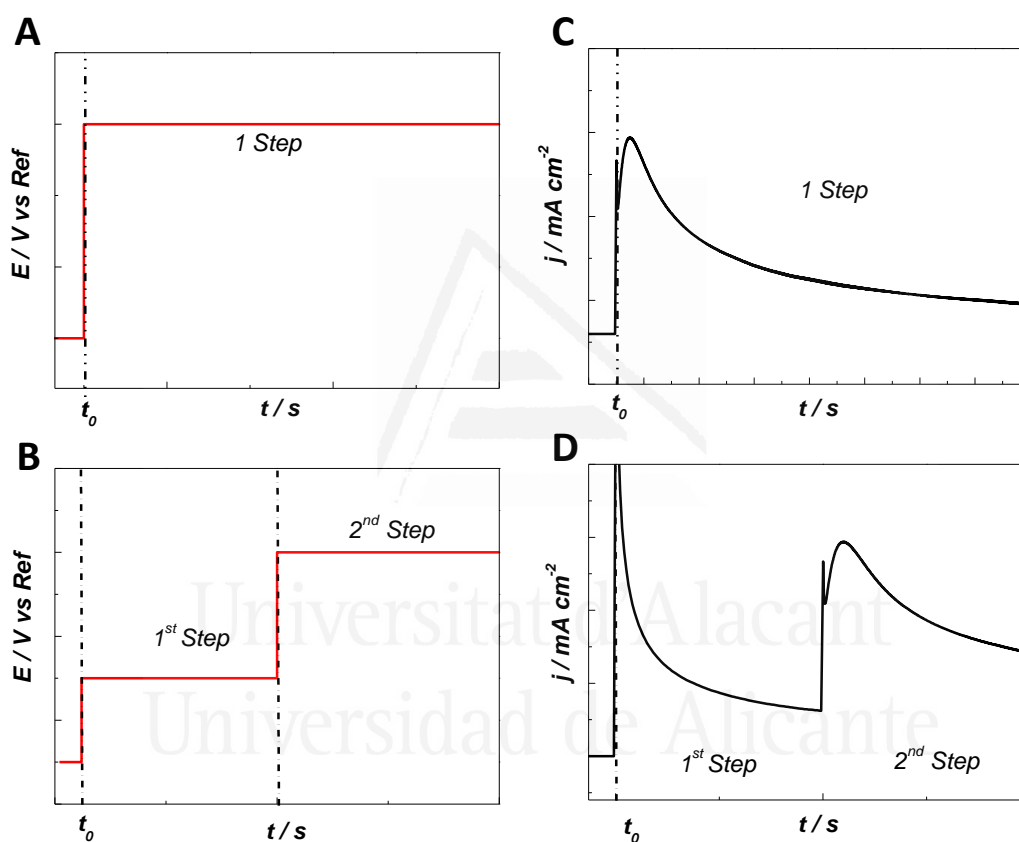


Figure 3.23: Chronoamperometry technique. Single and double potential steps. A) and B) correspond to the signal. C) and D) are the chronoamperometric j - t transient for single and double potential step, respectively.

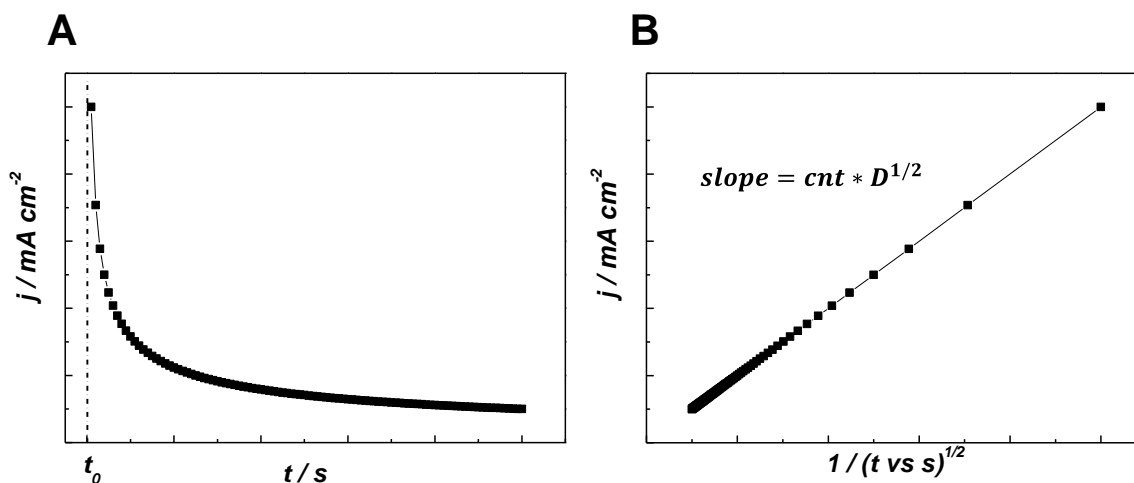


Figure 3.24: A) j - t transient under mass control limitation, B) linearization of A).

3.4.2) Techniques to characterize the $M(hkl)$ /solution interface

3.4.2.1) The electrified interfacial metal/solution . Introduction

The interfacial region between two phases: α and β , is the separation region in which the properties change from α to β . The deep knowledge of the main properties that govern the Metal/solution interface is important for the understanding of the different electrochemical reactions or processes that take place on it. One formulism to describe interfaces involving two phases is using the Gibbs isotherm. Gibbs isotherm applied for electrified interfaces provides the **Electrocapillary equation**:

$$-d\gamma = \sigma^M dE + \sum_i \Gamma_i d\mu_i \quad (3.10)$$

where γ is surface tension and Γ_i and μ_i are respectively the surface excess and chemical potential of the compound i . σ^M is the surface charge density on the metallic side, which is the same value than on the solution side (σ^S) but with opposite sign in order to obey the electroneutrality condition.

From the electrocapillary equation 3.10, it is obtained:

$$\sigma^M = -\left(\frac{\partial \gamma}{\partial E_{ap}}\right) \mu_i \quad (3.11)$$

Experimental electrocapillary curves γ vs E usually show non-symmetric parabolic shape in aqueous electrolytes. The maximum of the curve ($\sigma^M = 0$) corresponds to the **potential of zero charge, pzc**. This parameter is the potential at which the total charge on the surface is zero and provides the relation between the surface charge density and the applied potential, allowing rationalizing the electrochemical processes that takes place on the surface as a function of the measured charge.

Finally, the, the **differential capacitance** value of the interface Metal|solution is obtained (equation 3.12), where the capacitance is a measure of the charge storage capability at the applied potential:

$$C_d = \left(\frac{\partial \sigma^M}{\partial E_{ap}} \right) \quad (3.12)$$

In this section, we introduce the classical models that describe the electrified double layer region (Figure 3.25), initially employed to investigate aqueous electrolytes. These models: 1) are electrostatic, 2) do not consider specific adsorption and 3) do not consider the solvent interactions.

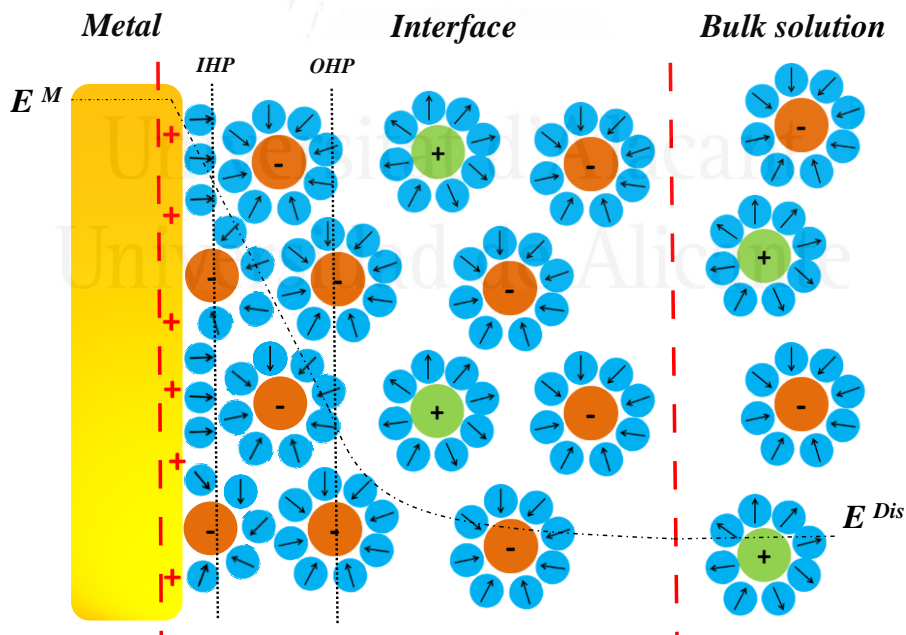


Figure 3.25: Double layer region of the Metal|solution electrified interface.

The simplest model to describe the double layer region is the **Helmholtz (H)** model. The Helmholtz's model considers the electrified interface as a parallel plate capacitor where the charge of the ions located at the electrolyte side is compensated by the counter charges in the metal electrode side. The surface charge density depends linearly on the applied potential as follows:

$$\sigma^M = \frac{\varepsilon\varepsilon_0}{d} E_{ap} \quad (3.13)$$

where ε and ε_0 are the dielectric constant and the permittivity in the vacuum respectively, and d is the distance between both metal electrolyte phases. Then, the **differential capacitance** is a constant value in all the potential range:

$$C_d = \left(\frac{\partial \sigma^M}{\partial E_{ap}} \right) = \frac{\varepsilon\varepsilon_0}{d} \quad (3.14)$$

Despite of simplicity of the model, Helmholtz approximation works quite well to describe the double layer region in high concentrated ion solutions. On the other limit, there is the **Gouy-Chapman theory (G-C)**. In the G-C theory, the authors propose that the double layer is a diffuse layer where the ion distribution depends on the value of the potential at any point. G-C applies a statistical treatment of the ion distribution across the double layer and concludes that ions arrange following a Boltzmann distribution. The potential dependence across the interface is exponential:

$$\phi = \phi_0 e^{-ax} \quad (3.15)$$

where ϕ_0 corresponds to the applied potential (E_{ap}) and x is the distance relative to electrode.

The capacitance vs potential dependence is:

$$C_d = \frac{d\sigma^M}{d\phi_0} = (A * c_{bulk}) * \cosh(B * E_{ap}) \quad (3.16)$$

Thus, G-C predicts a minimum in the capacitance curve (Figure 3.26) where the *pzc* is located. G-C model also predicts that the capacitance value increases infinitely by increasing the applied potential, which is unrealistic. This discrepancy in the model is because the model assumes that the charges are discrete points in the space that can arbitrarily occupy zero space (Boltzmann distribution), but in a real system ions have a finite size. The Gouy-Chapman-Stern modification (G-C-S) corrects this discrepancy. For

that, G-C-S combines Helmholtz and G-C and considers that interfacial region evolves both a Helmholtz region and a diffuse layer:

$$\frac{1}{C_d} = \frac{1}{C_H} + \frac{1}{C_{G-C}} \quad (3.17)$$

At sufficiently high applied overpotentials, the $1/C_H$ (Helmholtz capacitance) term dominates and the capacitance achieves a constant value, due to the surface polarization. At potentials near the pzc , the ion concentration is lower and the double layer behaves more as a diffuse layer (G-C).

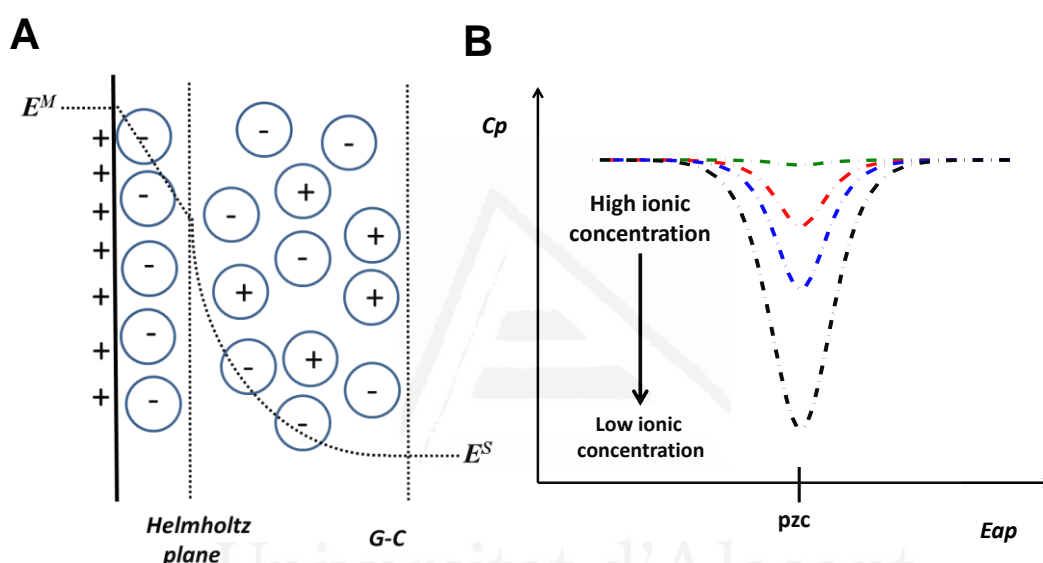


Figure 3.26: A) G-C-S double layer model. B) Capacitance vs applied voltage curves.

It is important to highlight that these models do not consider the role of the solvent. In addition, they only work relatively well to describe the Metal|solvent interface if the metal is a polarizable surface. The formalism of these models does not usually apply for metal|non-aqueous electrolytes. For ionic liquids, the high ion concentration and the ion-ion interactions influence the double layer structuration. From above, the metals that display high catalytic properties like Pt or Ir require other strategies for the study of their interfacial properties. So, the following section focus on describing the employed methodologies to study the $M(hkl)|solution^3$.

3.4.2.2) *The potential of zero charge. Definition and significance*

The potential of zero charge (pzc) is the potential at which the charge on the surface is zero. The pzc is a measure of how the surface charge changes with the applied potential. The pzc depends on both the nature of the material and the specific surface orientation. Trasatti et al. relates the pzc with the work function (ϕ) of the metal in an electrochemical environment. The work function is the energy needed to withdraw an electron from the metal phase to vacuum and it depends on the specific metal because of the electronics are different in each material, but it also depends on the specific surface orientation due to the atoms on the surface have different energy than the atoms in bulk structure (different coordination number). Table 3.6 summarize the work function values (ϕ/eV) of Pt, Au and Ir polycrystallines and $\langle 111 \rangle$ orientation. According to literature, for the same metal, closed packed structures have higher ϕ values. Then, the work functions of the lowest Miller index follow the next order: $(111) > (100) > (110)$. Table 3.7 contains the $\Delta\phi$ between the three basal plane orientations for Pt, Au and Ir.

<i>Metal</i>	<i>ϕ/eV</i>
<i>Pt</i>	5.30 ²⁷
<i>Pt(111)</i>	5.90-6.10 ²⁸
<i>Au</i>	4.70 ²⁷
<i>Au(111)</i>	5.25 ²⁹
<i>Ir</i>	5.00 ²⁷
<i>Ir(111)</i>	5.70-5.80 ²⁸

Table 3.6: Work functions (ϕ) of the employed metals in the present thesis.

<i>Metal</i>	<i>$\Delta\phi/eV$</i>		
	<i>(111)-(100)</i>	<i>(111)-(110)</i>	<i>(100)-(110)</i>
<i>Pt</i>	0.218	0.632	0.414
<i>Au</i>	0.190	0.553	0.363
<i>Ir</i>	0.237	0.680	0.499

Table 3.7: Theoretical differences between work functions of the basal planes for Pt, Ir and Au³⁰.

The relation between the work function and the potential of the metal in an aqueous environment is:

$$E^M = \frac{\phi^M}{e} + \delta\chi^M - g^s(dip) + g(ion) + E_{ref} \quad (3.18)$$

Where E^M is the potential of the electrode, ϕ^M (eV) is the work function of the metal, and $g^s(dip)$ is the dipole contribution of the solvent network to the potential due to the surface polarization in the interfacial region, contribution negative because the solvent dipoles orientate in the direction of electric field. $g(ion)$ is the ion contribution to the potential of the electrode. Finally, $\delta\chi^M$ is the modification of the surface potential in the metal due to the presence of the solvent, i.e, the electron spillover. Obviously, these terms change with the applied potential (E_{app}), including the metal work function because of different E_{app} values change the energy required to withdraw surface electrons. So, the pzc ($g(ion)=0$) is expressed as:

$$pzc = \frac{\phi^M}{e} + \delta\chi^M - g^s(dip) + E_{ref} \quad (3.19)$$

At the pzc , the solvent contribution is not zero ($g^s(dip) \neq 0$) due to there is a chemical bond between the surface and the solvent dipoles and then a neat surface orientation of the solvent dipoles occur^{31,32}.

If the material studied is a polarizable surface displaying wide electrochemical window, the pzc can be determined relatively easy obtaining the capacitive curves (for gold electrode). However, the pzc on non-polarizable surfaces such as platinum or iridium is challenging because of the total charge accounts for faradaic charge (electron transfer, anion specific adsorption...) and the capacitive charge or free charge. As the capacitive charge can not be separated from the total charge, the presence of faradaic reactions complicates the analysis of the interfacial properties on these electrodes. In fact, on platinum or iridium electrodes two pzc must be defined. The potential of zero total charge ($pztc$) and the potential of zero free charge ($pzfc$). The former one is the potential at which the total charge is zero (eq. 3.20) and the later takes into account the free or capacitive charge (eq. 3.21):

$$pztc = \Gamma_i + \sigma = 0 \quad (3.20)$$

$$pzfc = \sigma = 0 \quad (3.21)$$

The $pztc$ has been calculated by using the CO displacement technique, whereas the $pzfc$ can be estimated using the laser induced temperature jump technique. The following section summarizes these two techniques³³.

3.4.2.3) CO displacement technique

The CO displacement technique is used on high catalytic surfaces such as Pt or Ir electrodes. The procedure consists on the displacement of all the absorbed species using carbon monoxide (CO).

Initially, the electrode is kept at a specific potential and at the meniscus configuration in the solution under inert conditions. The electrochemical cell is well deoxygenated with Ar because small traces of oxygen introduce a negative contribution in the charge-displaced curves, thus underestimating the total displaced charge at $E_{ap} < pztc$ (Figure 3.27B)^{2, 34}. A glass capillary is introduced in the cell and positioned near the electrode. The CO stream flows slowly through this capillary avoiding that the meniscus was broken. The electrode was maintained under potential control and the charge displaced by the CO is monitored (Figure 3.27A).

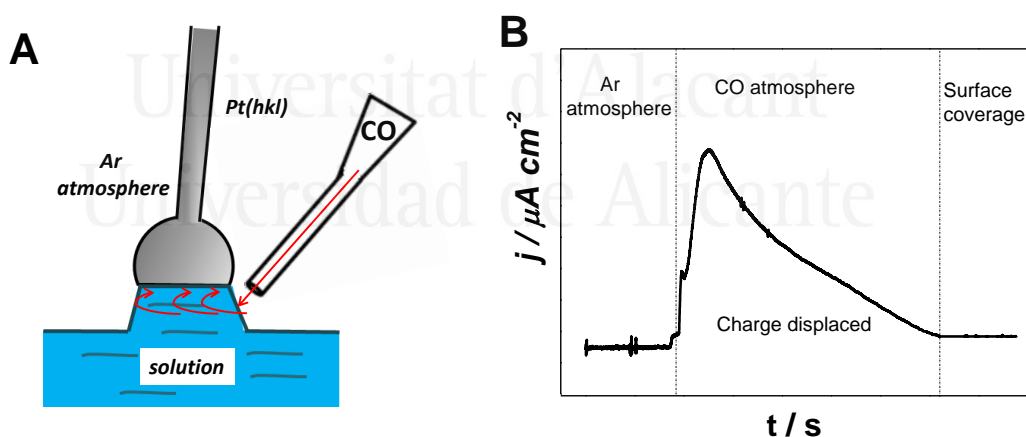
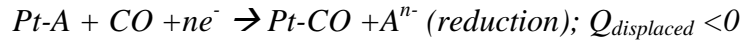
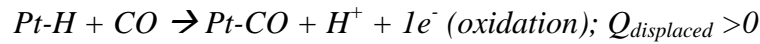


Figure 3.27: Experimental set-up. B) Monitoring of the charge displaced by CO.

If the applied potential corresponds to a region where proton is adsorbed on the surface (low applied potentials), the displaced charge is positive, meaning that the total neat charge on the surface has a negative sign. However, if the applied potential is located

in the potential region where hydroxide or anions are specifically adsorbed, the displaced charge is negative being the charge on the surface positive:



The total displaced charge corresponds to:

$$Q_{surface} = -Q_{displaced} + Q_{CO} \quad (3.22)$$

$$Q_{displaced} = -Q_{surface} + Q_{CO} \quad (3.23)$$

The displaced charge also contains small contribution from the CO capacitive charge, or the charge involved in the formation of the Pt-CO|solution double layer, which is almost negligible. Then, equation 3.23 can be approached to:

$$Q_{displaced} \approx -Q_{surface} \quad (3.24)$$

The idea is calculating the total charge at several applied potentials, in particular at those potentials where specific adsorption takes place ($\Gamma \gg \sigma$). Then the voltammetric region is integrated to obtain the charge value at any potential. The previous $Q_{displaced}(E_{app})$ value obtained by CO displacement is the integration constant in the $Q(E)$ vs E curve :

$$Q(E) = \frac{1}{v} \int_{E_{ap}}^E j dE - Q_{displaced}(E_{ap}) \quad (3.25)$$

where $Q(E)$ is the charge at any potential, v is the scan rate and j is the current density. The curve obtained after integration of the voltammetric curve provides the value of the $pztc$. This potential corresponds to the value at which the CO displacement curve cross the ($y=0$) axis (Figure 3.28).

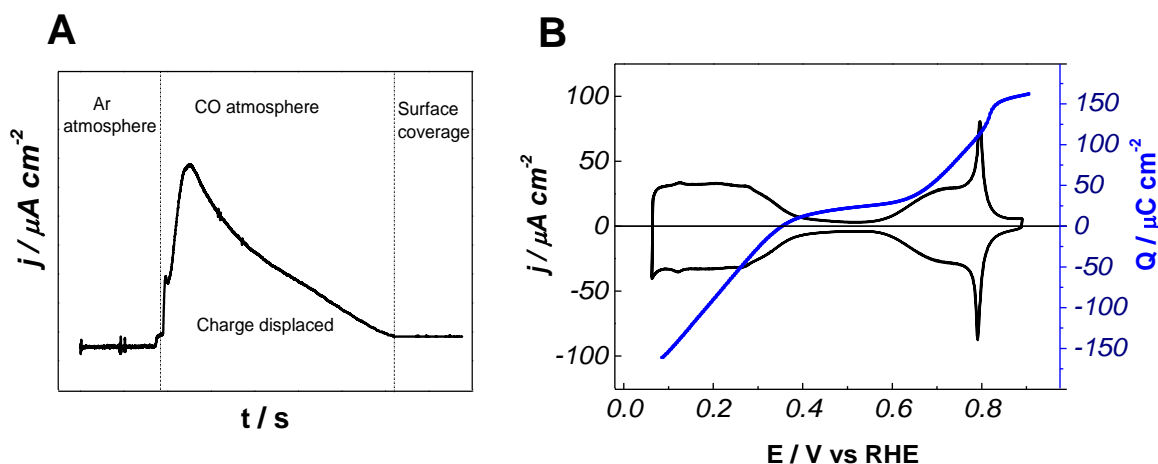


Figure 3.28: On Pt(111) A) Charge displaced by the CO at an applied potential of 0.10V vs RHE ($\approx 160 \mu\text{C cm}^{-2}$). B) Cyclic voltammogram recorded for Pt(111)|0.1M HClO_4 interface and CO charge curve.

The potential at which the $pztc$ is located does not always correspond to the position of the $pzfc$, since the $pztc$ involves both the capacitive and faradaic charges. The knowledge of the $pzfc$ value is usually of more interest than the former one due to the $pzfc$ approach better to the work function expectations. The CO displacement technique sometimes allows estimating the $pzfc$ taking into account a few considerations: 1) the capacitive contribution value of the CO monolayer is subtracted from the total charge; 2) then the $pzfc$ is estimated by extrapolation of the capacitive charge values obtained in the double layer region (Weaver approximation). These considerations imply that this methodology only allows estimating the $pzfc$ on surfaces that display a double layer region, such as Pt(111)/(perchlorate/perchloric mixtures). For the rest of the cases, it is not possible to separate the free charge from the total charge³⁵.

Figure 3.29 shows five possible scenarios for the $pzfc$ and $pztc$ location. Scenarios (1) and (2) corresponds to a situation in which the $pztc$ is located in a region where specific adsorption takes place, then the capacitive charge (σ) is not 0 and is compensated by the faradaic contribution (Γ): The scenarios (3) and (4) correspond to a situation in which σ is zero and then the $pzfc$ is obtained, but Γ is not zero. In the last scenario (5), both the $pzfc$ and the $pztc$ are located at the same potential position and there is neither faradaic contribution nor capacitive contribution. This situation occurs when the pzc falls in the voltammetric double region, i.e., at pH 3 in perchloric/perchlorate solutions^{36, 37}

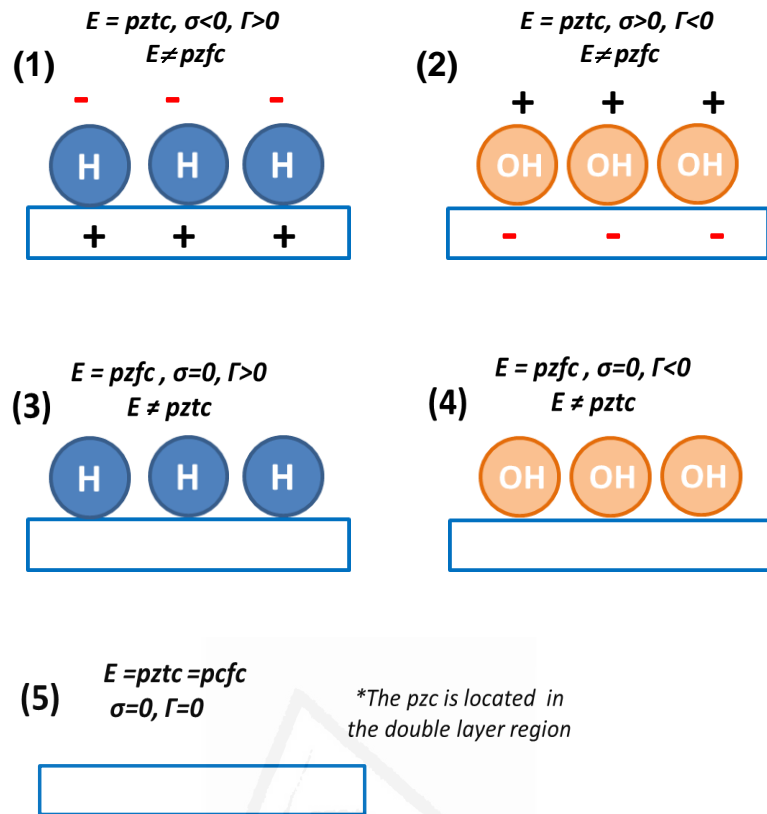


Figure 3.29: Scheme of the charge distribution in the Metal/solution double layer region at the both $pztc$ and $pzfc$.

In the present thesis, the CO displacement technique was employed to explore the charge distribution on Ir(111) in contact with different pH solutions and calculating the $pztc$ of this electrode. Results were compared with previous $pzfc$ values estimated using laser induced temperature jump technique.

3.4.2.4) Laser induced temperature jump technique

3.4.2.4.1) Experimental set-up and basic fundamentals

Laser induced temperature jump technique (LIPT)³⁸⁻⁴³ is a technique that measures the potential change of the electrode in the microsecond scale towards an external thermal perturbation. For that, short laser pulses of 5 ns and 532 nm of wavelength are fired to the surface electrode. The energy of the laser pulse ranges between 8-16 mJ cm⁻². It is important to highlight that the only effect from firing the laser

is a fast increase of the temperature in the interfacial region. The work function values of the metals employed in this thesis are sufficiently high and no electron withdrawing or emission during the laser firing is observed ($E_{\lambda(532nm)} = 2.34 eV$). The increase of the temperature in the interfacial region is due to the heat dissipation. Before firing the laser, the electrode potential is kept at a specific potential value using the potentiostat-galvanostat. 200 μs before firing the laser, the counter electrode is disconnected, leading the working electrode at open circuit potential. However, due to the thermal perturbation is enough fast (5 ns), the open circuit potential is not attained during the time that the measure is performed. The change in the electrode potential due to the increase of temperature is recorded at constant charge (under coulostatic conditions).

To allow the measure, the different parts of the laser technique set-up (potentiostat-galvanostat, oscilloscope and Q-Switch) are connected each other through different electronic devices. Among these electronic components, there are: a box of functions, a box of switches and different amplifiers. These components coordinate the laser firing with the turning off of the switches (that disconnect the counter electrode allowing the oscilloscope to monitor the potential electrode change at open circuit potential). The potential change is amplified by a factor of 30. Once the laser is fired, the counter electrode is again connected during a few *ms* in order to ensure that the electrode is kept at the desirable applied potential. The oscilloscope averages around 200 ΔE vs t transients for any applied potential. The employed oscilloscope was a Tecktronix TDS3054B. The Q-Switch is Nd-YAG laser that provides a high energetic laser beam, but its energy density is modulated by using an external attenuator. The laser beam diameter is decreased to 4mm by positioning a set of divergent and convergent lenses conveniently. By using mirrors, the laser beam is focused to the electrode surface. In addition, a splitter is placed between the electrochemical cell and the Q-Switch (Figure 3.30). The laser beam is then divided in two secondary beams. While one sub-beam goes to the cell, the other one is collected with a Laser power energy analyser that provides the energy value of the beam. The electrical noise is minimized placing the electrochemical cell in a faraday box. Figure 3.30 contains a scheme of the laser technique set-up.

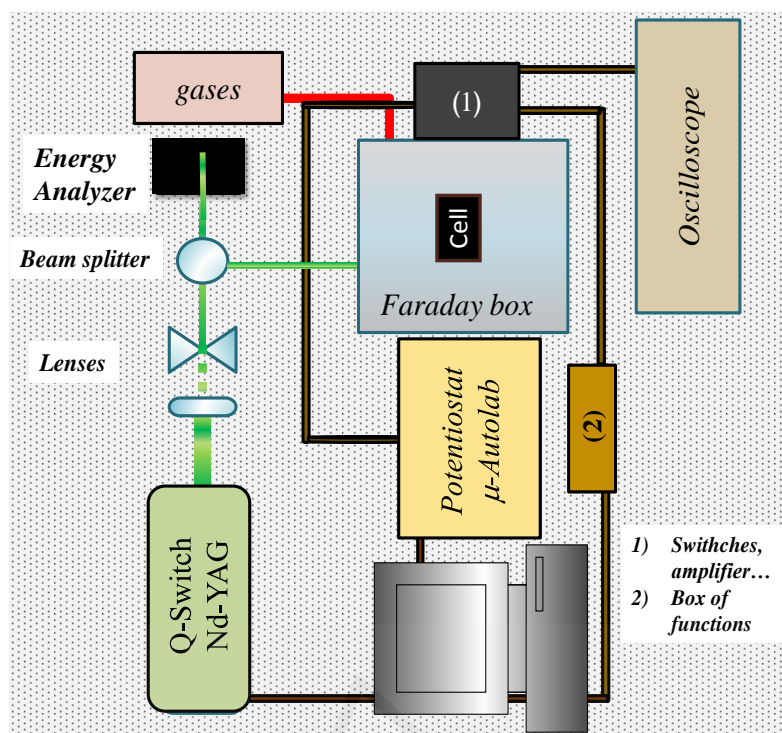


Figure 3.30: Laser induced temperature jump technique set-up.

The electrochemical cell has two working electrodes besides the reference electrode and the counter electrode. One of the working electrodes is the single crystal electrode in contact with the solution by the meniscus configuration. The other working electrode is a wire made with the same metal than the single crystal electrode. Both working electrodes are kept at the same applied potential but only the laser pulse perturbs the single crystal electrode. The technique actually measures the potential change difference between both working electrodes (W_1 and W_2). Before carrying the experiment, a blank ΔE vs t transient is recorded (the laser beam trajectory is intercepted before reaching the surface electrode). This blank transient is automatically subtracted from the laser transient as:

$$[\Delta E_{w1,laser}(t) - \Delta E_{w2,laser}(t)] - [\Delta E_{w1,blank}(t) - \Delta E_{w2,blank}(t)] = \Delta E_{w1,laser}(t) - \Delta E_{w1,blank}(t) \quad (3.26)$$

As the potential change of the second working electrode is zero, because of the W_2 is not perturbed by the laser, the ΔE_{w2} term is cancelled and the technique provides the potential change in the W_1 electrode. This procedure helps to minimize the electrical noise, evidenced in the blank laser transient.

The glass cell has five openings and a screw at the bottom part (Figure 3.31). The cell fits in a polyvinyl chloride (PVC) or methacrylate piece that supports it. Between the PVC holder and the glass cell, a quartz lens transparent to the laser beam is placed.

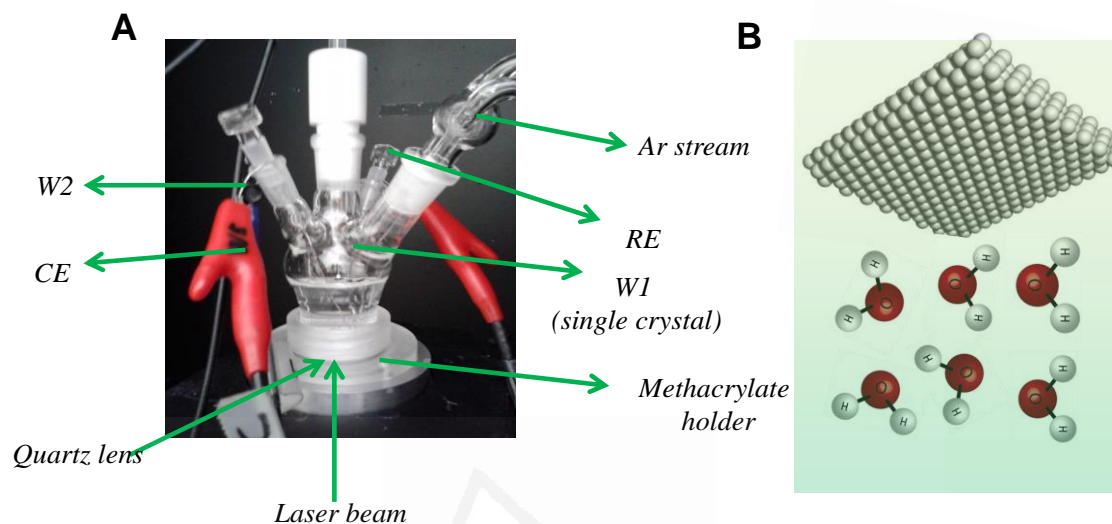


Figure 3.31: A) Electrochemical cell employed in laser experiments, B) Pt(111)/aqueous solution interface perturbed with a laser pulse.

The potential of the electrode contains several contributions³¹ (equation 3.18). The first and the second term (work function and spill over respectively) are considered as the potential terms for the metal side in the interfacial region, and hardly changes with the temperature. In high concentrated ionic solutions, the ionic contribution $g(ion)$ approaches to $\sigma/\epsilon\epsilon_0$. Although the permittivity value is temperature dependent, the ionic contribution change with the temperature is very small and this can be considered as negligible. So, the change in the potential electrode with the temperature is mainly given by the dipolar contribution to the electrode potential as follows:

$$\frac{\partial E^M}{\partial T} \approx - \frac{\partial g^s(dip)}{\partial T} \quad (3.27)$$

The dipolar contribution to the electrode is against the potential of the metal electrode since the dipoles orientate in the direction of the electric field. An increase of the temperature introduces disorder in the solvent dipolar network (water molecule network in aqueous electrolytes) thus decreasing its contribution to the potential electrode. If the potential of the electrode is lower than the pzc , i.e., the dipolar

contribution is positive (water molecules orientate with the hydrogens towards the surface), a negative transient is obtained, $\Delta E < 0$, due to the temperature increase. However, if the applied potential is higher than the pzc , the electrode potential is positive and the dipolar contribution is negative (water molecules orientate with the oxygen towards the surface). Hence, the laser provides a positive transient $\Delta E > 0$. At the potential in which there is maximum disorder in the solvent network, there is not dipolar contribution and the obtained transient has zero value. This potential is the potential of maximum entropy of the double layer formation (pme) and is close to the $pzfc$ because the solvent dipoles structuration in the interfacial region is sensitive to the electric field, i.e., to the free charge. Figure 3.32 summarizes the abovementioned fundamentals.

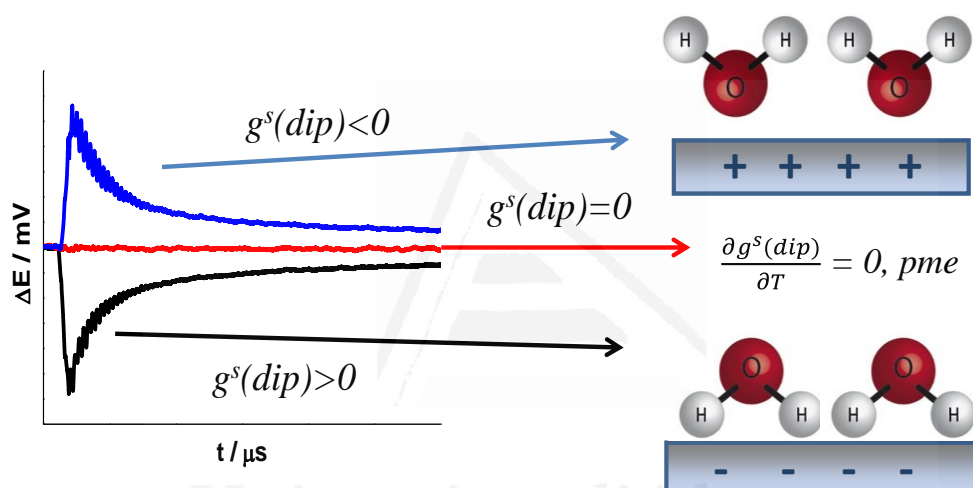
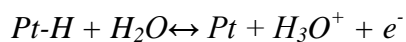


Figure 3.32: Scheme of the solvent network distribution with the thermal perturbation and the corresponding laser transients.

The main advantage of using the laser technique to investigate $M(\text{hkl})|\text{solution}$ interfaces is that the technique can decouple processes with different rates (as the laser perturbation is fast, the provided response is also fast). The double layer restructuring is usually faster than any other processes. Therefore, the technique can separate pure capacitive processes from faradaic or adsorption processes, providing a measure of the potential change linked with the free charge in the surface.

In acidic perchloric/perchlorate solutions at pH 1 or 2, the hydrogen adsorption/desorption equilibrium influences the laser response at low applied potentials, and the ΔE vs t transients display a bipolar profile (Figure 3.33):



The double layer restructuration is the fastest process, thus the decrease of the potential electrode due to the thermal disordering of the solvent network causes a shift of the hydrogen adsorption/desorption equilibrium in the proton adsorption direction. The proton adsorption withdraws an electron from the metallic side causing an increase of the potential electrode. The capacitive contribution to the potential electrode (negative response) is against the faradaic contribution (positive response). Consequently, laser responses at pH 1 and 2 are not monotonic. Since the adsorption reaction rate depends on the proton concentration, increasing the pH decreases the proton adsorption rate until its laser response is completely decoupled at pH 3.

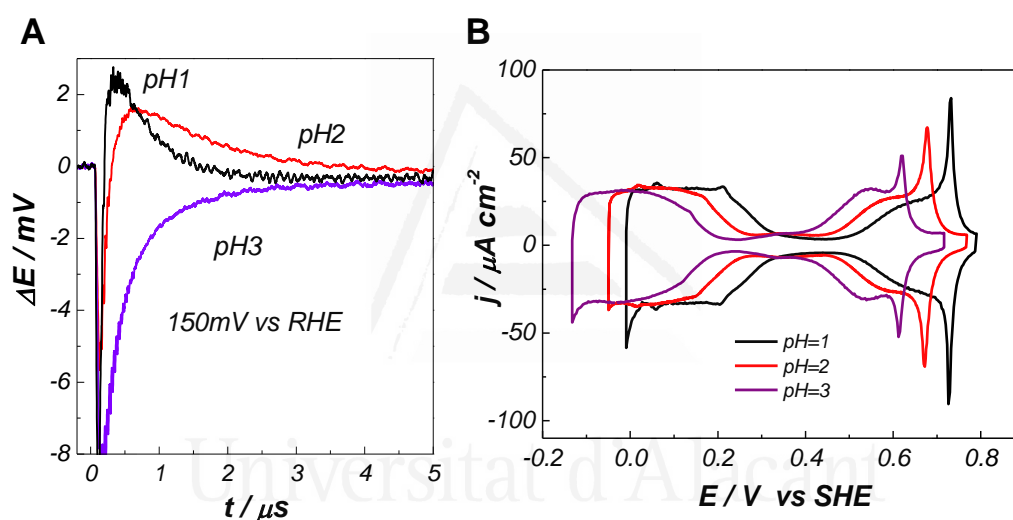


Figure 3.33: For different $\text{HClO}_4/\text{KClO}_4$ mixtures solutions A) laser ΔE vs t transients at 0.150 mV vs RHE at pH 1 to 3. B) Cyclic voltammograms at pH 1 to 3 at 50 mV/s.

3.4.2.4.2) Theoretical aspects

In the absence of specific adsorption phenomena, or adsorption phenomena responses are negligible in the microsecond scale, the potential change in the electrode after the laser perturbation follows the relaxation of the temperature in the interface. As the perturbation is too fast (5 ns), we cannot measure the temperature increase. However, by applying a simple thermal model, the temperature change with time can be estimated, assuming that the only effect from firing the laser is the heating of the interfacial region,

i.e., the non-reflected part of the laser is suddenly converted into heat. The temperature vs time dependence is obtained resolving these partial equations:

$$\frac{\partial^2 \Delta T}{\partial x^2} = \frac{1}{\alpha_i} \frac{\partial \Delta T}{\partial t} \quad (3.28)$$

Applying the boundary conditions

$$-\kappa \frac{\partial \Delta T}{\partial x} \Big|_{x=0^+} = q - q' \quad (3.29)$$

$$-\kappa_1 \frac{\partial \Delta T}{\partial x} \Big|_{x=0^-} = -q' \quad (3.30)$$

$$\Delta T(x, t = 0) = 0 \quad (3.31)$$

$$\lim_{x \rightarrow \pm\infty} (\Delta T(x, t)) = 0 \quad (3.32)$$

In this model, the surface of the metal is located at $x = 0$. In this framework $x < 0$ corresponds to the solution and $x \geq 0$ to the metal; q' is the heat flux conducted to the solution whereas q is the flux of heat absorbed at the surface of the electrode, i.e., the part of the radiation that is not reflected. κ , α and κ_1 , α_1 are the thermal conductivity and the thermal diffusivity of the metal and the solution, respectively. At the same time, $\alpha = \kappa/\rho c$, where ρ is the material density and c is the heat capacity.

Here, q (heat flux in the metal) can be expressed as follows:

$$q = (1-R)I \quad (3.33)$$

where I is the laser intensity (considered spatially uniform) and R is the reflectivity of the surface.

By solving the above-mentioned equations and applying Laplace Transform, the change in temperature with time is:

$$\Delta T = \frac{2(1-R)I}{\sqrt{\pi}} \left[\frac{\kappa}{\sqrt{\alpha}} + \frac{\kappa_1}{\sqrt{\alpha_1}} \right]^{-1} (\sqrt{t} - \sqrt{t-t_0}) \quad t > t_0 \quad (3.34)$$

So the maximum temperature change at the surface is ($t=t_0$):

$$\Delta T_0 = \frac{2(1-R)I}{\sqrt{\pi}} \left[\frac{\kappa}{\sqrt{\alpha}} + \frac{\kappa_1}{\sqrt{\alpha_1}} \right]^{-1} \sqrt{t_0} \quad (3.35)$$

For instance, for Pt electrodes, the maximum temperature change by applying a laser beam of 8mJcm^{-2} density approach to 35K.

At sufficiently long times ($t \gg t_0$) the temperature decay with time can approximate to:

$$\Delta T = \frac{1}{2} \Delta T_0 \sqrt{\frac{t_0}{t}} \quad (3.36)$$

being the potential change with the temperature:

$$\Delta E = \frac{\partial E}{\partial T} \Delta T = \frac{1}{2} \frac{\partial E}{\partial T} \Delta T_0 \sqrt{\frac{t_0}{t}} \quad (3.37)$$

$\frac{\partial E}{\partial T}$ is the temperature coefficient at any applied potential. They can be extracted from the slopes obtained by plotting ΔE vs $1/\sqrt{t}$.

From the electrocapillary equation (equation 3.7) and by introducing the corresponding thermodynamic relations, it can be demonstrated that the thermal coefficient is related with the entropy of formation of the double layer as:

$$-d\gamma = \sigma_M dE^M + \Delta S_{dl} dT \quad (3.38)$$

$$\left(\frac{\partial E^M}{\partial T}\right)_{\sigma_M, \Gamma_H, \Gamma_{OH}, p, c_i} = -\left(\frac{\partial \Delta S_{dl}}{\partial \sigma_M}\right)_{T, p, c_i} \quad (3.39)$$

where σ_M is the charge density on the metal and ΔS_{dl} is the difference in the entropy of the constituents of the double layer when they are forming it and when they are present in the bulk of the adjoining phases. From the above-mentioned equations, one can see that the potential at which the transient is zero, the curve ΔS_{dl} vs Q shows a maximum value at this potential value, and then it corresponds to the *pme*.

The calculated thermal coefficient from the ΔE vs $1/\sqrt{t}$ slopes also contains a thermodiffusion contribution that could limit the analysis. This thermodiffusion potential is due to the temperature difference between the working electrode and the reference electrode that causes the ions in solution move because of this temperature gradient. The thermodiffusion potential can be estimated by knowing the entropy of transport of the ions in solution (Eastman coefficients) as follows:

$$\frac{\Delta E}{\Delta T} = \frac{\Delta E_{dl}}{\Delta T} + \frac{\Delta E_{thermodiffusion}}{\Delta T} \quad (3.40)$$

$$\frac{\Delta E_{thermodiffusion}}{\Delta T} = -\frac{1}{F} \sum \frac{t_i}{z_i} \widehat{S}_i \quad (3.41)$$

where t_i , z_i , and \widehat{S}_i are the transport number, the charge (with its sign) and the Eastman entropy of transport of the ion i , respectively. The transport numbers are calculated from the tabulated ionic mobilities of the ions, but these are taken at infinitely diluted solutions (u_i), which introduces a source of error in the calculation (although this is small and treated as negligible here):

$$t_i = \frac{|z_i|c_i u_i}{\sum |z_i|c_i u_i} \quad (3.42)$$

where c_i is the bulk concentration of the corresponding anion.

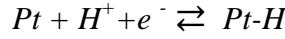
The thermodiffusion potential contribution due to the thermal coefficient is in most of the cases negligible, except at high acidic or basic solutions due to the abnormal high entropy of transport of OH^- and H^+ ions. Table 3.8 compares the entropy of transport of OH^- and H^+ with other ions usually employed in electrochemistry.

<i>Ion</i>	$\widehat{S}_i/\text{Jmol}^{-1}\text{K}^{-1}$
H^+	39.44
OH^-	53.9
ClO_4^-	-3.10
K^+	4.40

Table 3.8: Entropy of transport of the ions that compose the mixtures $\text{HClO}_4/\text{KClO}_4$.

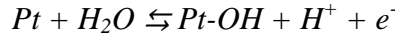
The abovementioned equations are only valid if the response through the laser perturbation is only related with the restructuration of the double layer, i.e., in absence of specific adsorption and faradaic reactions or when they are too slow being negligible in the measured time scale. Figure 3.34 shows that the laser transient displays a bipolar behaviour evidencing two different overlapped contributions. These contributions correspond to two processes with different relaxation times, i.e., displaying different kinetics. Specific adsorption is kinetically slower than the double layer restructuration phenomena, and is analysed by using a Frumkin isotherm and Butler-Volmer equations.

For the adsorption of a monovalent cation (like hydrogen) at $\text{pH} < 7$ solutions:



$$\frac{d\theta_H}{dt} = k_H^0 [(1 - \theta_H)c_{H^+} \exp\left[\frac{-0.5}{RT}(FE^{SHE} + \overline{\Delta G^0} + \omega_{H-H}\theta_H)\right] - \theta_H \exp\left[\frac{0.5}{RT}(FE^{SHE} + \overline{\Delta G^0} + \omega_{H-H}\theta_H)\right]] \quad (3.43)$$

For the adsorption of an anion (hydroxide) at pH<7 solutions:



$$\frac{d\theta_{OH}}{dt} = k_{OH}^0 [(1 - \theta_{OH}) \exp\left[\frac{0.5}{RT}(FE^{SHE} - \overline{\Delta G^0} - \omega_{OH-OH}\theta_{OH})\right] - \theta_{OH}c_{H^+} \exp\left[\frac{0.5}{RT}(-FE^{SHE} + \overline{\Delta G^0} + \omega_{OH-OH}\theta_{OH})\right]] \quad (3.44)$$

where θ is the normalized coverage; k^0 is the standard rate constant; E^{SHE} is the electrode potential measured vs. an SHE reference electrode; $\overline{\Delta G^0}$ is the Gibbs energy of adsorption at $\theta = 0$; and ω is the lateral interaction parameter.

The change in the electrode potential evolving both contributions (capacitive and specific adsorption) is expressed by using the following equation:

$$\Delta E(t, \theta) = b_{dl}\Delta T + \frac{q_{ML}}{C_{dl}}\Delta\theta \quad (3.45)$$

where C_{dl} is the double-layer capacity, $\Delta E = E - E_i$, and $\Delta\theta = \theta - \theta_i$. E_i and θ_i are the initial potential and the initial coverage, respectively. q_{ML} is the charge related to the adsorption of a ion monolayer, ΔT is the temperature change and b_{dl} is the response of the double-layer potential to the increase of the temperature.

The change of the electrode potential due to the restructuring of the double layer towards the thermal perturbation (term 1 from equation 3.45) shifts the ion adsorption/desorption equilibrium, influencing the potential change in the electrode (term 2 eq. 3.45).

Combining equations 3.43 or 3.44 with 3.45 allows simulating the ΔE vs t transients at different applied potentials and compare with experimental results. Numerical solution of the previous equations requires the application of computational methods. For the details of the transient modelling, see references^{33, 40-42, 44}. The analysis of the ΔE vs t transients also provides values of the kinetic constants of ion adsorption/desorption reaction on the surface.

All these theoretical considerations allow deeply analysing interfacial processes related to solvent restructuration in the M(hkl)|aqueous electrolyte interface. But when the selected electrolyte is an IL, the following assumptions were taken. As an IL is a high dense coulombic system composed by discrete ions, the proposed scenarios would be: 1) at sufficient low applied potentials the density of cations in the interface may be higher than the anion density, and a negative transient should be obtained. 2) At sufficiently high positive applied potentials, the population of anions should increase and a positive transient would be obtained. 3) At the potential at which the population of anions and cations is the same, there is not electrolyte/solvent contribution to the electrode potential, and the laser transient should be zero. This potential would be the *pme* in ionic liquid media.

3.5) Ex-situ techniques

3.5.1) Scanning Electron Microscopy (SEM)

The scanning electron microscopy (SEM) techniques use a very thin and energetic beam of electrons that are ejected to the sample surface. These electrons (called as primary electron beam) penetrate through the sample producing different phenomena that finally generate several signals. From these signals, morphological and chemical information (energy dispersive X-ray spectroscopy (EDS)) can be obtained. How deep the primary electrons penetrate in the sample depends on both its Z number and the energy electron beam (or acceleration voltage). Once the electrons have reached and deepened in the sample they generate: 1) secondary electrons (dispersed primary electron that have lost energy due to the collision), which produce SEM images; 2) backscattered electrons that produce both BSE (backscatter electrons) images revealing the Z numbers of the different elements. Figure 3.34 contains a scheme of the different signals obtained when the primary electron deeps into the surface sample:

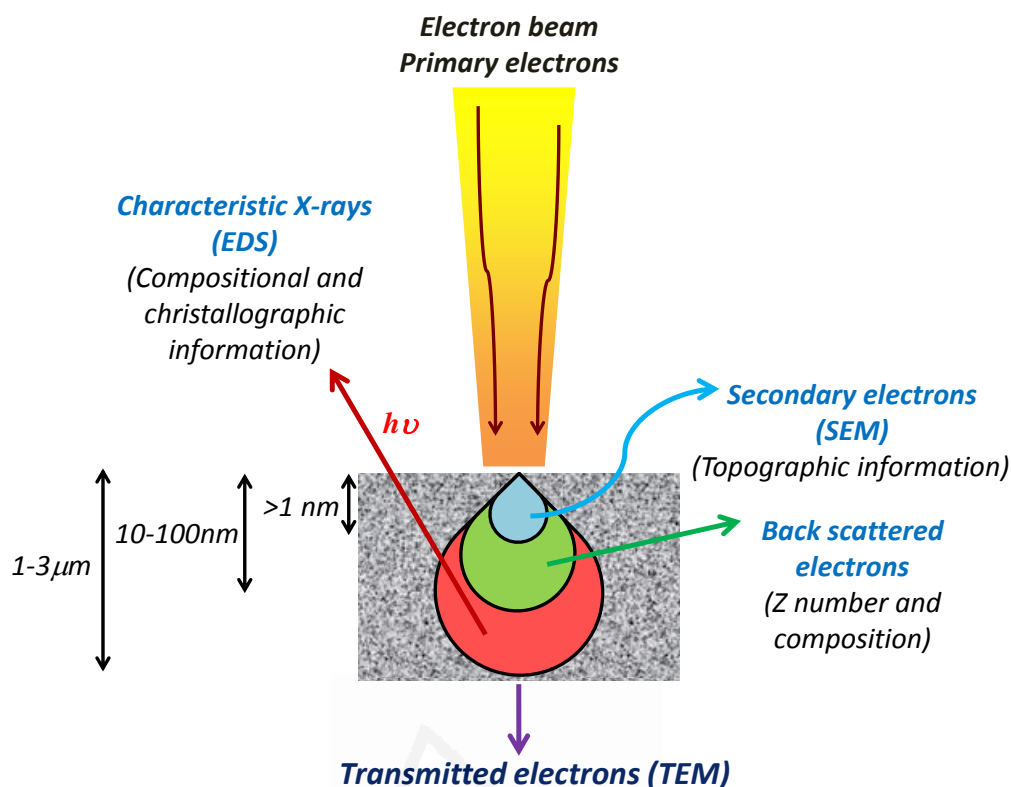


Figure 3.34: Scheme of the different processes involving electron emission.

In the present study, several SEM setups were used: JEOL JSM-7100F (*Centres Científics i Tecnològics de la Universitat de Barcelona (CCiT-UB)*), Field-emission Hitachi H-4100FE SEM (*CCiT-UB*) and Field-emission JEOL JSM-6510 SEM (*CCiT-UB*) *FE-SEM*. It is worth to say that the spatial resolution of FE-SEM is from 3 to 6 times higher than conventional SEM equipment.

The SEM was employed to analyse the morphology of metallic deposits obtained on glassy carbon on both aqueous and DES solution. SEM was also used to study the morphology of the nickel deposits on both glassy carbon and Pt surfaces. The samples have to be conductive and electrically grounded to avoid an excess of charge on top of the surfaces. It was necessary to apply a colloidal silver strip between the surface and the stub to improve the electrical contact and avoid artefacts. A scheme that reveals the main components of a FE-SEM equipment can be found in Figure 3.35.

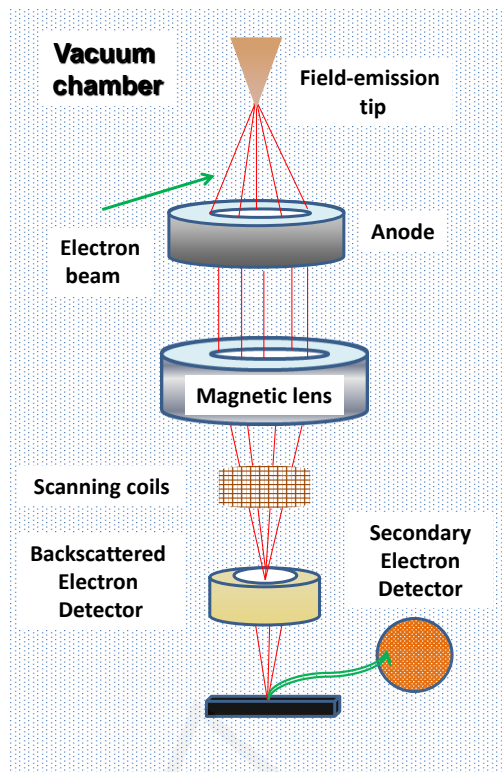


Figure 3.35: Scheme of a conventional field-emission scanning electron microscope (FE-SEM).

The primary electrons are accelerated and focalized by adjusting a game of electromagnetic field lenses. Several detectors are conveniently placed to collect and detect the electrons dispersed⁴⁵⁻⁴⁶.

3.5.2) Energy Dispersive X-Ray Spectroscopy (EDS)

Energy dispersive X-Ray spectroscopy (EDS) provides rapid information of elemental composition. Either SEM or FE-SEM systems have usually coupled a X-detector that collects elemental information of the analysed surfaces. The high energetic electrons emitted to the surfaces penetrate inside the sample. These electrons cause that electrons in the inner layers of a specific element kick out leading a hole. This new elemental configuration is high energetic and therefore not stable. Then, the excited element relaxes to a fundamental state, i.e., an electron from outer layers occupies the empty hole (Figure 3.36). Consequently, a photon (X-Ray spectrum) is emitted and detected by the X-Ray detector. Since each element has a unique atomic structure, the

EDS provides the set of peaks in its X-Ray spectrum for any element in the periodic table (characteristic X-Ray radiation). Calibration of the equipment was necessary in order to obtain quantitative results before taking the measurements. EDS was employed to evaluate the metal presence⁴⁵⁻⁴⁶.

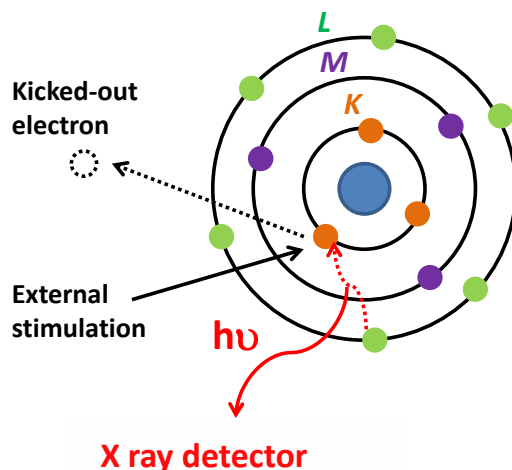


Figure 3.36: Scheme of the atomic level of element X.

3.5.3) X-Ray Photoelectron Spectroscopy (XPS)

X-Ray Photoelectron Spectroscopy is a surface spectroscopic technique that provides information about chemical and electronic states and can also quantify chemical composition³. The sample is irradiated with a monochromatic X-Ray beam (e.g., the AlK_{α} line at 1486.6 eV or the $Mg K_{\alpha}$ line at 1253.6 eV). Due to this radiation ($h\nu$), electrons in the deep core levels are ejected to the vacuum environment. From atoms located near the surface sample, these electrons are inelastically scattered, losing kinetic energy. The energy of a photon ejected is conserved and can be divided in the following terms:

$$h\nu = E_b + E_k + \phi_{sp} \quad (3.46)$$

where $h\nu$ is the photon energy, E_b is the binding energy (eV), E_k is the kinetic energy of the electrons ejected outside and ϕ_{sp} is the work function value associated to the X-Ray spectrometer (3-4 eV). A photoelectron spectrogram plots the number of electrons detected, sometimes per unit time, (Y -axis) versus the binding energy of the detected electrons (X -axis).

XPS can provide atomic information about the surface region without seriously surface damaging. Information about oxidation states is also available, because the binding energy of one electron in an orbital is influenced by its electronic environment. In XPS spectrograms, peaks are often broad and they are usually overlapped, fact that sometimes complicates the assignment of the compound or oxidation states (Figure 3.37).

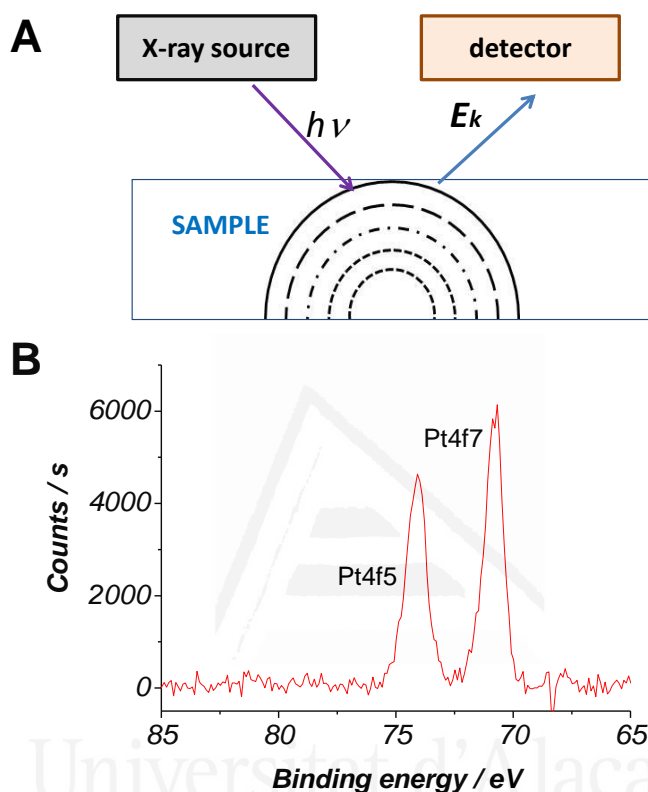


Figure 3.37: A) X-ray spectrophotometer scheme and B) XPS spectrogram of Pt.

XPS was employed to analyse the different surface states of Ni deposits onto Pt electrode.

3.5.4 X-Ray Diffraction (XRD)

X-Ray diffraction (XRD) is used for the investigation of crystal structures and crystallographic orientations and provides structural information. This technique consists on focusing an X-Ray beam on the sample with an angle (θ), and measuring the diffraction angles of the scattered beam (Figure 3.38). Constructive interferences take

place under Bragg's law, and the intensity of the peaks can be measured. Bragg's law equation is expressed below:

$$2 d_{hkl} \sin(\theta) = n_x \lambda \quad (3.47)$$

where d_{hkl} is the distance between lattice planes, λ is the X-Ray wavelength, n_x is the diffraction order and θ is the angle between the X-Ray beam and the samples surface. X-Ray diffraction allows determining different crystallographic structures or orientations in polycrystalline samples, grain size and chemical analysis.

A Philips MRD diffractometer (CCiT-UB) with parallel optical geometry using Cu K α radiation ($\lambda = 1.5418 \text{ \AA}$) and a texture goniometer, which allows control of the sample rotation about the three axes. By analysing the diffraction patterns, crystallographic orientation can be estimated from the resulting peaks positions. The full width at half maximum (FWHM) can be directly obtained from the peak profile. The crystallite size and the average width of the micro-strain distribution can be semi-quantitatively deduced from the broadening of the adjusted pseudo-Voigt function to the diffracted peaks. Absolute values cannot be taken into account since XRD is sensitive to the presence of crystallographic defects⁴⁷.

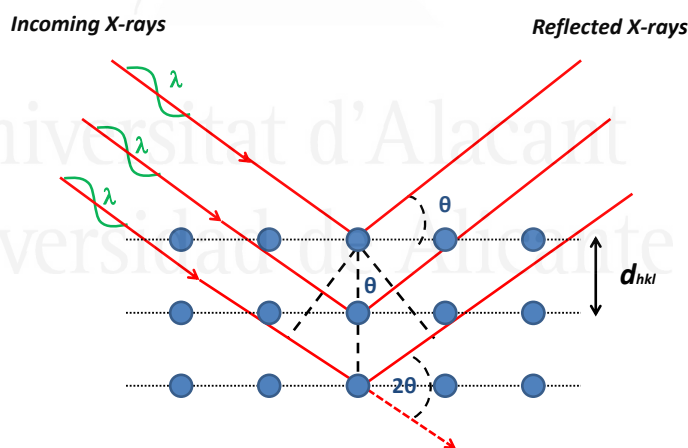


Figure 3.38: Schematic representation of XRD geometry.

XRD was employed to investigate different facets orientation formed on the prepared Ni deposits in DES.

3.5.5) *Electron probe microscopy: Atomic Force Microscopy*

Electron probe microscopies are versatile and valuable tool in this research topic. They are based on a scanning probe (commonly called as tip) located just above the surface. The tip shifts over the surface scanning a specific region while monitoring the interaction between the atoms in the tip and the atoms in the surface. The type of interaction defines the specific electron probe technique. The interaction between the tip and the surface generates a signal that can provide images of high resolution even at an atomic or molecular level. Relevant structural surface information of the materials studied are provided by these techniques.

In atomic force microscopy (AFM)⁴⁸, different attractive/repulsive forces between the tip and the surface operate. These forces are mainly: 1) Coulombic forces: Strong repulsive interactions between the electron clouds in both the tip and the surface. 2) van der Waals interactions, longer range attractive forces due to the formation of fluctuating dipoles. Both of these types of forces increases by decreasing the distance between the tip and the surface, but in balance the net force become repulsive since Coulombic forces are stronger than van der Waals (Figure 3.39).

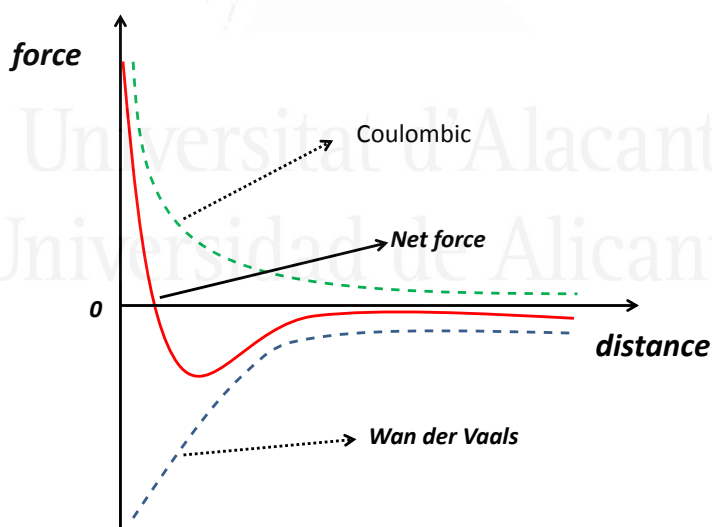


Figure 3.39: Representation of the forces that operate in AFM.

In AFM, samples are not necessarily conductive because of no external voltage is needed to apply. The tip is positioned at the extreme of a long beam called cantilever. The motion of the cantilever is detected by reflecting a diode laser beam in the back part

of the cantilever, as represented in Figure 3.40. The reflected laser is collected in a photo-detector. The photo-detector has four sections, being position sensitive. The vertical deflection of the cantilever is defined by the difference in light intensity measured by the upper and lower sectors. The lateral deflection of the cantilever is determined by the left and right sectors of the photo-detector.

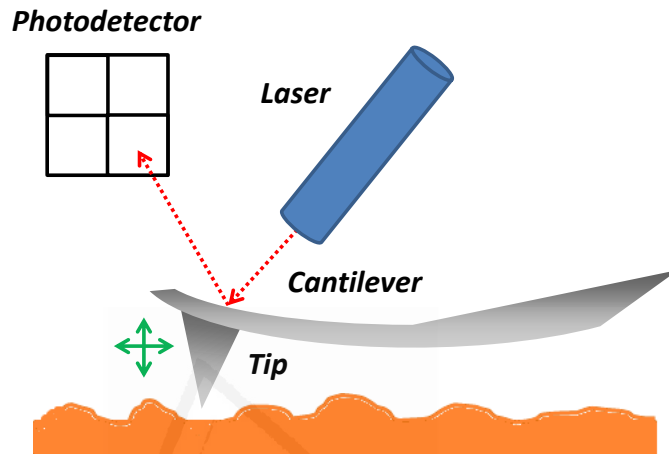


Figure 3.40: Scheme of the main parts of the set-up in AFM.

Although AFM has different modes to operate, contact mode was the only mode employed to analyse the nickel deposits on Pt(111). In contact mode, the tip contacts the surface and the detector monitors how the cantilever deflection changes. The resultant force is calculated using Hooke's law:

$$F = -k x \quad (3.48)$$

F is the force, k is the spring constant and x is the cantilever deflection.

The feedback circuit adjusts the probe height to maintain a constant force and deflection on the cantilever. This is known as the deflection set-point. Contact mode can operate in air or in liquid. While it allows high speed scans and can scan roughness surfaces, lateral interactions or capillary forces can distort the images causing the appearance of artefacts, likely related with the damage of the tip. So, the cantilever needs to deflect easily without damaging the sample surface or tip. For that, the cantilever should have a low spring constant, (0.3–2 μm) and a high resonant frequency to avoid vibrational instability (100–200 μm). The tip has usually pyramidal shape and can be

doped to make it conductive if electrical signal is needed. The sharper the tip is, the best resolution is obtained.

AFM was used to analyse nickel deposits on Pt(111) and in DES, at low coverages.

3.6) REFERENCES

- (1) J.M. Feliu, E. H. a. V. C., Electrocatalytic properties of stepped surfaces. In *Catalysis in Electrochemistry. From Fundamentals to strategies for fuel cell development*, Schmickler, E. S. a. W., Ed. John Wiley Sons: New Jersey, 2011.
- (2) Carol Korzeniewski, V. C., and Juan M. Feliu, Electrochemistry at Pt single crystal Electrodes, Chapter Book, Electroanalytical Chemistry. In *Electroanalytical Chemistry. A Series of Advances*, CRC Press: 2011; Vol. 75.
- (3) Faulkner, A. J. B. a. L. R., *Electrochemical methods. Fundamentals and applications*. 2nd ed.; Wiley: New York, 2001; p 850.
- (4) Clavilier, J.; Faure, R.; Guinet, G.; Durand, R., Preparation of monocrystalline Pt microelectrodes and electrochemical study of the plane surfaces cut in the direction of the {111} and {110} planes. *Journal of Electroanalytical Chemistry and Interfacial Electrochemistry* **1980**, *107* (1), 205-209.
- (5) Petrii, S. T. a. O. A., Real surface area measurements in electrochemistry. *Journal of Electroanalytical Chemistry* **1992**, 327.
- (6) Climent, V.; Feliu, J. M., Thirty years of platinum single crystal electrochemistry. *Journal of Solid State Electrochemistry* **2011**, *15* (7), 1297.
- (7) Clavilier, J., The role of anion on the electrochemical behaviour of a {111} platinum surface; an unusual splitting of the voltammogram in the hydrogen region. *Journal of Electroanalytical Chemistry and Interfacial Electrochemistry* **1979**, *107* (1), 211-216.
- (8) Clavilier, J.; Armand, D.; Sun, S. G.; Petit, M., Electrochemical adsorption behaviour of platinum stepped surfaces in sulphuric acid solutions. *Journal of Electroanalytical Chemistry and Interfacial Electrochemistry* **1986**, *205* (1), 267-277.
- (9) Momma, K.; Izumi, F., VESTA 3 for three-dimensional visualization of crystal, volumetric and morphology data. *Journal of Applied Crystallography* **2011**, *44* (6), 1272-1276.
- (10) Lide, C. R., *CRC Handbook of Chemistry and Physics*. 79 ed.; CRC Press: Boca Raton, 1998.
- (11) Clavilier, J., The role of anion on the electrochemical behaviour of a {111} platinum surface; an unusual splitting of the voltammogram in the hydrogen region. *Journal of Electroanalytical Chemistry* **1979**, *107* (1), 211-216.
- (12) Kibler, L. A.; Cuesta, A.; Kleinert, M.; Kolb, D. M., In-situ STM characterisation of the surface morphology of platinum single crystal electrodes as a function of their preparation. *Journal of Electroanalytical Chemistry* **2000**, *484* (1), 73-82.
- (13) Hanc-Scherer, F. A.; Sanchez-Sanchez, C. M.; Ilea, P.; Herrero, E., Surface-Sensitive Electrooxidation of Carbon Monoxide in Room Temperature Ionic Liquids. *ACS Catalysis* **2013**, *3* (12), 2935-2938.

- (14) Hanc-Scherer, F. A.; Montiel, M. A.; Montiel, V.; Herrero, E.; Sanchez-Sanchez, C. M., Surface structured platinum electrodes for the electrochemical reduction of carbon dioxide in imidazolium based ionic liquids. *Physical Chemistry Chemical Physics* **2015**, *17* (37), 23909-23916.
- (15) Ejigu, A.; Walsh, D. A., The Role of Adsorbed Ions during Electrocatalysis in Ionic Liquids. *Journal of Physical Chemistry C* **2014**, *118* (14), 7414-7422.
- (16) Pajkossy, T.; Kibler, L. A.; Kolb, D. M., Voltammetry and impedance measurements of Ir(1 1 1) electrodes in aqueous solutions. *Journal of Electroanalytical Chemistry* **2005**, *582* (1-2), 69-75.
- (17) Kolb, D. M., Reconstruction phenomena at metal-electrolyte interfaces. *Progress in Surface Science* **1996**, *51* (2), 109-173.
- (18) Gnahn, M.; Pajkossy, T.; Kolb, D. M., The interface between Au(111) and an ionic liquid. *Electrochimica Acta* **2010**, *55* (21), 6212-6217.
- (19) Gnahn, M.; Muller, C.; Repanszki, R.; Pajkossy, T.; Kolb, D. M., The interface between Au(100) and 1-butyl-3-methyl-imidazolium-hexafluorophosphate. *Physical Chemistry Chemical Physics* **2011**, *13* (24), 11627-11633.
- (20) Oliveira-Brett, C. M. A. B. a. A. M., *Electrochemistry. Principles, Methods and Applications*. Oxford, New York, Tokyo, 1993.
- (21) Fredlake, C. P.; Crosthwaite, J. M.; Hert, D. G.; Aki, S. N. V. K.; Brennecke, J. F., Thermophysical properties of imidazolium-based ionic liquids. *Journal of Chemical & Engineering Data* **2004**, *49* (4), 954-964.
- (22) Dong, K.; Zhang, S. J., Hydrogen Bonds: A Structural Insight into Ionic Liquids. *Chemistry-a European Journal* **2012**, *18* (10), 2748-2761.
- (23) https://portal.uni-freiburg.de/fril/fril_home/fundamentals/physical_properties.
- (24) Bonhôte, P.; Dias, A.-P.; Papageorgiou, N.; Kalyanasundaram, K.; Grätzel, M., Hydrophobic, Highly conductive ambient-temperature molten salts. *Inorganic Chemistry* **1996**, *35* (5), 1168-1178.
- (25) Abbott, A. P.; Capper, G.; Davies, D. L.; Munro, H. L.; Rasheed, R. K.; Tambyrajah, V., Preparation of novel, moisture-stable, Lewis-acidic ionic liquids containing quaternary ammonium salts with functional side chains. *Chemical Communications* **2001**, (19), 2010-2011.
- (26) Gnahn, M.; Kolb, D. M., The purification of an ionic liquid. *Journal of Electroanalytical Chemistry* **2011**, *651* (2), 250-252.
- (27) Trasatti, S., Work function, electronegativity, and electrochemical behaviour of metals. *Journal of Electroanalytical Chemistry and Interfacial Electrochemistry* **1972**, *39* (1), 163-184.
- (28) Kaack, M.; Fick, D., Determination of the work functions of Pt(111) and Ir(111) beyond 1100 K surface temperature. *Surface Science* **1995**, *342* (1), 111-118.
- (29) Otálvaro, D.; Veening, T.; Brocks, G., Self-assembled monolayer induced Au(111) and Ag(111) reconstructions: work functions and interface dipole formation. *The Journal of Physical Chemistry C* **2012**, *116* (14), 7826-7837.
- (30) Aref'eva, L. P.; Shebzukhova, I. G., Electron work function and surface energy of body-centered and face-centered cubic modifications of 4d- and 5d-metals. *Physics of the Solid State* **2016**, *58* (7), 1289-1294.

-
- (31) Trasatti, S., The temperature coefficient of the water dipole contribution to the electrode potential. *Journal of Electroanalytical Chemistry and Interfacial Electrochemistry* **1977**, 82 (1), 391-402.
- (32) Trasatti, S., Structuring of the solvent at metal/solution interfaces and components of the electrode potential. *Journal of Electroanalytical Chemistry and Interfacial Electrochemistry* **1983**, 150 (1–2), 1-15.
- (33) N.García-Araez, V. C. a. J. M. F., Temperature effects on platinum single-crystal/Aqueous solution interphases. Combining Gibbs Thermodynamics with Laser-Pulsed experiments. In *Modern aspects of Electrochemistry*, J.O.M Bockris, B. E. C. a. R. E. W., Ed. Plenum Press: New York and London, 2002; Vol. 17.
- (34) Clavilier, J.; Albalat, R.; Gomez, R.; Orts, J. M.; Feliu, J. M.; Aldaz, A., Study of the charge displacement at constant potential during CO adsorption on Pt(110) and Pt(111) electrodes in contact with a perchloric acid solution. *Journal of Electroanalytical Chemistry* **1992**, 330 (1), 489-497.
- (35) Weaver, M. J., Potentials of zero charge for platinum(111)-aqueous interfaces: A combined assessment from in-situ and ultrahigh-vacuum measurements. *Langmuir* **1998**, 14 (14), 3932-3936.
- (36) Martínez-Hincapié, R.; Sebastián-Pascual, P.; Climent, V.; Feliu, J. M., Exploring the interfacial neutral pH region of Pt(111) electrodes. *Electrochemistry Communications* **2015**, 58, 62-64.
- (37) Rizo, R.; Sitta, E.; Herrero, E.; Climent, V.; Feliu, J. M., Towards the understanding of the interfacial pH scale at Pt(1 1 1) electrodes. *Electrochimica Acta* **2015**, 162, 138-145.
- (38) Smalley, J. F.; Krishnan, C. V.; Goldman, M.; Feldberg, S. W.; Ruzic, I., Laser-induced temperature-jump coulostatics for the investigation of heterogeneous rate processes: Theory and application. *Journal of Electroanalytical Chemistry and Interfacial Electrochemistry* **1988**, 248 (2), 255-282.
- (39) Benderskii, V. A.; Velichko, G. I., Temperature jump in electric double-layer study. *Journal of Electroanalytical Chemistry and Interfacial Electrochemistry* **1982**, 140 (1), 1-22.
- (40) Climent, V.; Coles, B. A.; Compton, R. G., Laser-induced potential transients on a Au(111) single-crystal electrode. Determination of the potential of maximum entropy of double-layer formation. *Journal of Physical Chemistry B* **2002**, 106 (20), 5258-5265.
- (41) Climent, V.; Coles, B. A.; Compton, R. G., Coulostatic potential transients induced by laser heating of a Pt(111) single-crystal electrode in aqueous acid solutions. Rate of hydrogen adsorption and potential of maximum entropy. *Journal of Physical Chemistry B* **2002**, 106 (23), 5988-5996.
- (42) Garcia-Araez, N.; Climent, V.; Feliu, J., Potential-dependent water orientation on Pt(111), Pt(100), and Pt(110), As inferred from laser-pulsed experiments. Electrostatic and chemical effects. *Journal of Physical Chemistry C* **2009**, 113 (21), 9290-9304.
- (43) Garcia-Araez, N.; Climent, V.; Feliu, J. M., Evidence of water reorientation on model electrocatalytic surfaces from nanosecond-laser-pulsed experiments. *Journal of the American Chemical Society* **2008**, 130 (12), 3824-3833.
- (44) W.H. Press, B. P. F., S.A. Teukolsky and W.T. Vetterling, *Numerical Recipes in Fortran 77: The Art of Scientific Computing* 2ed.; 1992; Vol. 1.
-

- (45) J. Goldstein, D. E. Newbury, D. C. Joy, C. E. Lyman, P. Echlin, E. Lifshin, L. Sawyer, J. R. Michael, Scanning electron microscopy and X-ray microanalysis, Springer, New York, (2003).
- (46) L. Reimer, Scanning electron microscopy, Springer, New York (1998).
- (47) C. Suryanarayana, M. G. Norton, X-Ray diffraction: a practical approach, Springer, New York, USA (2013).
- (48) University of Cambridge DoITPoMS web page. Atomic Force Microscopy. www.doitpoms.ac.uk.



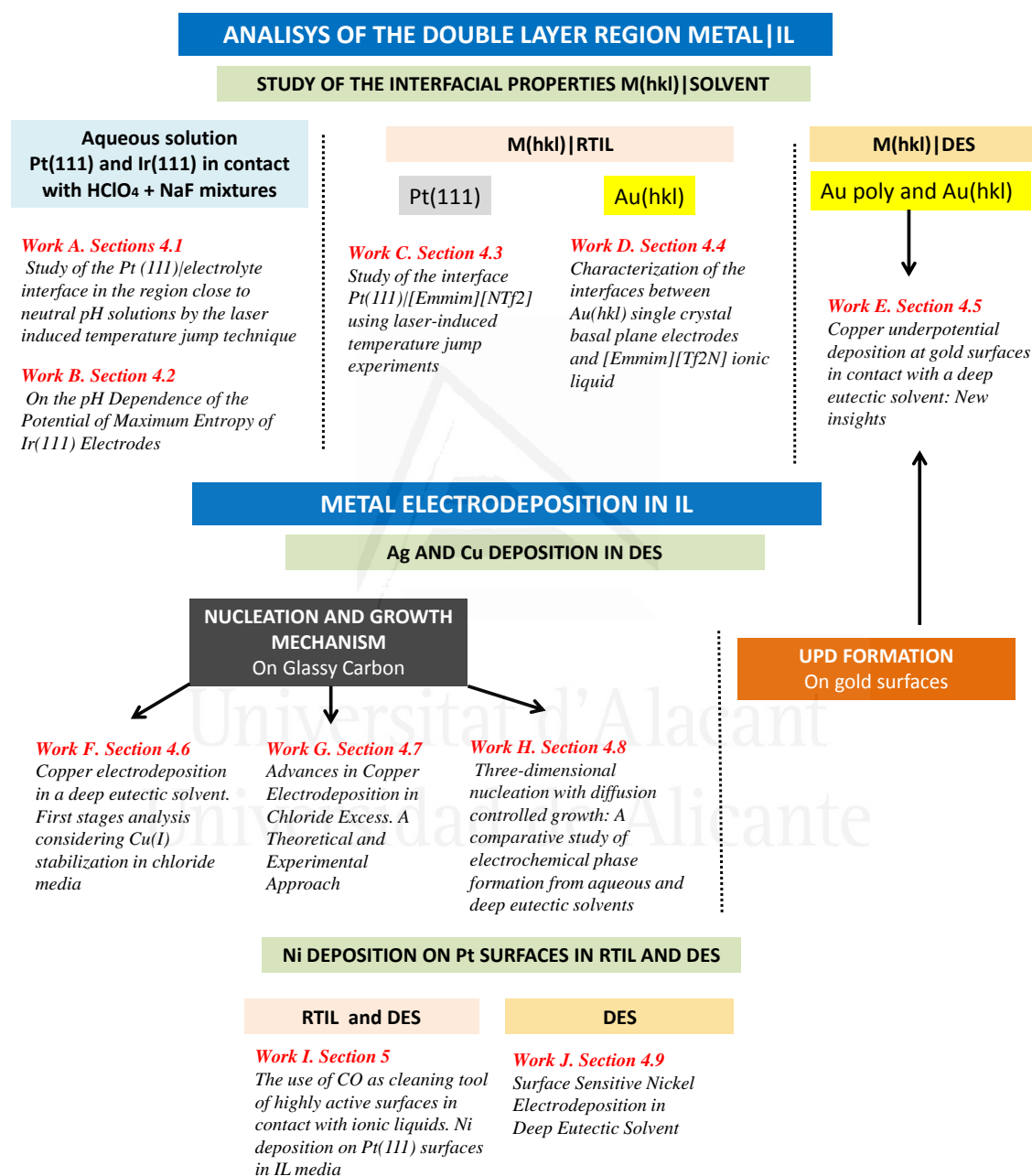
Universitat d'Alacant
Universidad de Alicante

Chapter 4

Publications

Universitat d'Alacant
Universidad de Alicante

According to the objectives introduced in chapter 1, works in different sections should be read following the next scheme.



4.1) Study of the Pt (111) / electrolyte interface in the region close to neutral pH solutions by the laser induced temperature jump technique

P. Sebastián, R. Martínez-Hincapié, V. Climent, J.M. Feliu

Electrochimica Acta, 2017, 228,667-676.

DOI: [10.1016/j.electacta.2017.01.089](https://doi.org/10.1016/j.electacta.2017.01.089)

WORK A

Abstract

The laser-induced temperature jump method is used to determine the potential of maximum entropy (pme) of a Pt(111) single crystal electrode in contact with an aqueous solution, in a wide pH range and in the absence of specifically adsorbed anions. For this purpose, buffer solutions composed of a mixture of NaF and HClO₄ are used. The results are compared with those from non-buffered perchlorate solutions. The use of the NaF/HF buffer allows extending the pH range from 3 to 6, approaching the situation of a neutral pH. Laser experiments show that the pme appears located at nearly the same potential position in the whole pH range between 3 and 6. This value is around 300 mV vs SHE, in agreement with previous works. Moreover, the potential response to the fast thermal perturbation at high potentials, above the pme, indicates the presence of a slower contribution, resulting in a bipolar, non-monotonous, profile. Such behaviour is strongly affected by the presence of fluoride anion and/or hydrofluoric acid, thus evidencing a strong structural effect on interfacial water from these species. These results bring some light to the understanding of the interfacial properties in acid-neutral conditions, and also show the influence of different non-specifically adsorbed anions on the interfacial properties that cannot be evidenced only by cyclic voltammetry.

4.2) On the pH Dependence of the Potential of Maximum Entropy of Ir(111) Electrodes

A. Ganassin, P. Sebastián, V. Climent, W. Schuhmann, A.S. Bandarenka, J.M. Feliu

Scientific Reports 2017,7 (1): 1246.

DOI: [10.1038/s41598-017-01295-1](https://doi.org/10.1038/s41598-017-01295-1)

WORK B

Abstract

Studies over the entropy of components forming the electrode/electrolyte interface can give fundamental insights into the properties of electrified interphases. In particular, the potential where the entropy of formation of the double layer is maximal (potential of maximum entropy, PME) is an important parameter for the characterization of electrochemical systems. Indeed, this parameter determines the majority of electrode processes. In this work, we determine PMEs for Ir(111) electrodes. The latter currently play an important role to understand electrocatalysis for energy provision; and at the same time, iridium is one of the most stable metals against corrosion. For the experiments, we used a combination of the laser induced potential transient to determine the PME, and CO charge-displacement to determine the potentials of zero total charge, (EPZTC). Both PME and EPZTC were assessed for perchlorate solutions in the pH range from 1 to 4. Surprisingly, we found that those are located in the potential region where the adsorption of hydrogen and hydroxyl species takes place, respectively. The PMEs demonstrated a shift by ~ 30 mV per a pH unit (in the RHE scale). Connections between the PME and electrocatalytic properties of the electrode surface are discussed.

© 2017 Nature

4.3) Study of the interface Pt(111)||[Emmim][NTf₂] using laser-induced temperature jump experiments

P. Sebastián, A.P. Sandoval, V. Climent, J.M. Feliu

Electrochemistry communications 2015,55, 39-42.

DOI: [10.1016/j.elecom.2015.03.012](https://doi.org/10.1016/j.elecom.2015.03.012)

WORK C

Abstract

The interface between a Pt(111) electrode and a room temperature ionic liquid, 1-ethyl-2,3-dimethylimidazolium bis(trifluoromethylsulfonyl)imide, was investigated with the laser-induced temperature jump method. In this technique, the temperature of the interface is suddenly increased by applying short laser pulses. The change of the electrode potential caused by the thermal perturbation is measured under coulostatic conditions during the subsequent temperature relaxation. This change is mainly related to the reorganization of the solvent components near the electrode surface. The sign of the potential transient depends on the potential of the experiment. At high potential values, positive transients indicate a higher density of anions than cations close the surface, contributing negatively to the potential of the electrode. Decreasing the applied potential to sufficiently low values, the transient becomes negative, meaning that the density of cations becomes then higher at the surface of the electrode. The potential dependence of the interfacial response shows a marked hysteresis depending on the direction in which the applied potential is changed.

© 2015 Elsevier B.V

4.4) Characterization of the interfaces between Au(hkl) single crystal basal plane electrodes and [Emmim][Tf₂N] ionic liquid

P. Sebastián, V. Climent, J.M. Feliu

Electrochemistry communications 2016,62, 44-47

DOI: [10.1016/j.elecom.2015.11.005](https://doi.org/10.1016/j.elecom.2015.11.005)

WORK D

Abstract

The interface between Au(hkl) basal planes and the ionic liquid 1-Ethyl-2,3-dimethyl imidazolium bis(trifluoromethyl)sulfonyl imide was investigated by using both cyclic voltammetry and laser-induced temperature jump. Cyclic voltammetry showed characteristic features, revealing surface sensitive processes at the interfaces Au(hkl)/[Emmim][Tf₂N]. From laser-induced heating the potential of maximum entropy (pme) is determined. pme is close to the potential of zero charge (pzc) and, therefore, the technique provides relevant interfacial information. The following order for the pme values has been found: Au(111) > Au(100) > Au(110). This order correlates well with work function data and values of pzc in aqueous solutions.

© 2015 Elsevier

4.5) Copper underpotential deposition at gold surfaces in contact with a deep eutectic solvent: New insights

P. Sebastián, E. Gómez, V. Climent, J.M. Feliu

Electrochemistry communications 2017,78, 51-55

DOI: [10.1016/j.elecom.2017.03.020](https://doi.org/10.1016/j.elecom.2017.03.020)

WORK E

Abstract

The electrodeposition of copper on a polycrystalline gold electrode and on Au(hkl) single crystals was investigated in a deep eutectic solvent (DES). The DES employed consisted of a mixture of choline chloride and urea (1:2). The Au(hkl)/DES interface was studied using cyclic voltammetry in the capacitive region. The blank voltammograms showed characteristic features, not previously reported, that demonstrate the surface sensitivity of this solvent. Copper electrodeposition was then studied and it was found that this takes place through the formation of an underpotential deposition (UPD) adlayer, demonstrating the surface sensitivity of this process. Voltammetric profiles showed similarities with those obtained in aqueous solutions containing chloride, suggesting that the copper UPD in this DES is strongly influenced by the presence of chloride.

© 2017 Elsevier B.V.

***4.6) Copper electrodeposition in a deep eutectic solvent.
First stages analysis considering Cu(I) stabilization in chloride
media***

P. Sebastián, E. Vallés, E. Gómez

Electrochimica Acta 2014,123, 285-295

DOI: [10.1016/j.electacta.2014.01.062](https://doi.org/10.1016/j.electacta.2014.01.062)

WORK F

Abstract

The aim of the present work is to study copper electrocrystallization in a Deep Eutectic Solvent (DES) (eutectic mixture of choline chloride and urea 1:2) as electrolyte, paying special attention to the influence of the liquid on the nucleation mechanism. Deposition process was studied from both Cu(II) and Cu(I) solutions. As the DES solvent is chloride rich, a parallel analysis was made in aqueous solution containing an excess of chloride to compare medium influence on nucleation mechanism. While copper (I) can be directly electrodeposited from chloride excess solutions, copper (II) electrodeposition takes place via a separate step in which Cu(II) is firstly reduced to Cu(I). A methodology is proposed for studying mechanistic aspects of the early stages of copper electrodeposition from the Cu(II) chloride solutions. For all solutions, cyclic voltammetry was used to establish the potential range at which copper electrodeposition occurred, while potentiostatic technique was used to study the nucleation mechanism. In all media, deposition follows a nucleation and three-dimensional growth controlled by diffusion. The diffusion coefficient of Cu(I) species present in the solution has been calculated from potentiostatic curves by logarithmic linear regression of j vs $t^{-1/2}$ at long deposition times, whereas the same parameter for copper (II) was calculated from cyclic voltammetry, taking advantage from the process quasi-reversibility. The viability of the nucleation mechanism by Scharifker-Hills model was demonstrated by the analysis of the rising part of the j - t transients independently of the selected solution.

© 2014 Elsevier

4.7) Advances in Copper Electrodeposition in Chloride Excess. A Theoretical and Experimental Approach

P. Sebastián, E. Torralba, E. Vallés, A. Molina, E. Gómez

Electrochimica Acta 2015,164, 187-195

DOI: [10.1016/j.electacta.2015.02.206](https://doi.org/10.1016/j.electacta.2015.02.206)

WORK G

Abstract

This is an in depth study in the knowledge of the nucleation and growth mechanism that governs copper electrodeposition in excess chloride media. In these conditions copper electro-reduction takes place via two well-separated steps, since the Cu(I) intermediate is stabilized through chloride complexation. The process was studied in two media, a deep eutectic solvent (DES) based on a mixture of urea and choline chloride, and in excess chloride aqueous solution, in order to also analyse solvent influence on the early stages of the deposition process. In both media, copper electrodeposition follows a nucleation and a diffusion controlled three-dimensional growth mechanism. In line with a previous work a double potentiostatic step signal was employed to record j - t transients associated to both nucleation and growth stages, and from them, the whole mechanistic analysis of the copper electrodeposition was performed. This analysis involved the calculation of the surface concentrations of Cu(II), free Cu(I) and complexed Cu(I) for any time and potential required and the application of Sharifker-Hills model, $j_m^2 t_m$ products and rising part analysis including the calculated parameters, which are strengthened as valuable tools for complete copper electrodeposition analysis in these media.

© 2015 Elsevier

4.8) Three-dimensional nucleation with diffusion controlled growth: A comparative study of electrochemical phase formation from aqueous and deep eutectic solvents

P. Sebastián, L.E. Botello, E. Vallés, E. Gómez, M. Palomar-Pardavé, B.R. Scharifker, J. Mostany

Journal of Electroanalytical Chemistry 2017, 794, 119-125

DOI: [10.1016/j.jelechem.2016.12.014](https://doi.org/10.1016/j.jelechem.2016.12.014)



WORK H

Abstract

The nucleation of Ag onto vitreous carbon from aqueous 3 M NaCl or 0.6 M NaClO₄ and deep eutectic solvent (DES) 1:2M mixture of choline chloride:urea solutions containing Ag⁺, has been studied analyzing the chronoamperometric response to single potential steps. From the coordinates of the maxima observed in the current responses, the nucleation frequencies A (s⁻¹) and number densities of nucleation sites N_0 (cm⁻²) were obtained from the standard model of nucleation with diffusion-controlled three-dimensional growth. Analysis of the overpotential dependence of nucleation frequencies using the classical electrochemical nucleation theory allowed to calculate the Gibbs free energy of nucleation $\Delta G^{\sim}n_c$ and critical nucleus size n_c as well as the exchange current density j_0 , transfer coefficient α and surface tension σ of silver nuclei. The kinetics of Ag⁺ reduction is two orders of magnitude slower in DES compared to both aqueous systems studied, and values of $\alpha \ll 0.5$ were found in both aqueous and DES media, indicating either that the intermediate state for metal ion reduction is located close to the initial state, i.e., the solvated or complexed metal ion in solution, or that the metal ion is specifically adsorbed on the surface and the symmetry factor involved requires an alternative electron transfer formalism. The low $\Delta G^{\sim}n_c$ and n_c values observed indicate that the discharge of a single Ag ion on the surface already becomes a supercritical nucleus, involving a very low Gibbs energy barrier, characteristic of a non-activated process.

4.9) Surface Sensitive Nickel Electrodeposition in Deep Eutectic Solvent

P. Sebastián, M. I. Giannotti, V. Climent, J.M. Feliu

ACS Applied Energy Materials 2018, 1, 1016-1028

DOI: [10.1021/acsaem.7b00177](https://doi.org/10.1021/acsaem.7b00177)

WORK J

Abstract

The first steps of nickel electrodeposition in a deep eutectic solvent (DES) are analyzed in detail. Several substrates from glassy carbon to Pt(111) were investigated pointing out the surface sensitivity of the nucleation and growth mechanism. For that, cyclic voltammetry and chronoamperometry, in combination with scanning electron microscopy (SEM), were employed. X-ray diffraction (XRD) and atomic force microscopy (AFM) were used to more deeply analyze the Ni deposition on Pt substrates. In a 0.1 M NiCl₂ + DES solution (at 70 °C), the nickel deposition on glassy carbon takes place within the potential limits of the electrode in the blank solution. Although, the electrochemical window of Pt|DES is considerably shorter than on glassy carbon|DES, it was still sufficient for the nickel deposition. On the Pt electrode, the negative potential limit was enlarged while the nickel deposit grew, likely because of the lower catalytic activity of the nickel toward the reduction of the DES. At lower overpotentials, different hydrogenated Ni structures were favored, most likely because of the DES co-reduction on the Pt substrate. Nanometric metallic nickel grains of rounded shape were obtained on any substrate, as evidenced by the FE-SEM. Passivation phenomena, related to the formation of Ni oxide and Ni hydroxylated species, were observed at high applied overpotentials. At low deposited charge, on Pt(111) the AFM measurements showed the formation of rounded nanometric particles of Ni, which rearranged and formed small triangular arrays at sufficiently low applied overpotential. This particle pattern was induced by the <111> orientation and related to surface sensitivity of the nickel deposition in DES. The present work provides deep insights into the Ni electrodeposition mechanism in the selected deep eutectic solvent.

Chapter 5

Other results

Universitat d'Alacant
Universidad de Alicante



OTHER RESULTS

The use of CO as cleaning tool of highly active surfaces in contact with ionic liquids. Ni deposition on Pt(111) surfaces in IL media

This work proposes a strategy to pre-treat a flame-annealed Pt(111) single crystal ensuring surface ordering to carry out experiments in ionic liquid (IL) media, avoiding water contamination. A room temperature ionic liquid (RTIL) and a Deep Eutectic Solvent (DES) representative of two families of ionic liquids were selected as test species: The RTIL [Emmim][Tf₂N] and the DES based on the mixture of choline chloride (ChCl) and urea (1ChCl:2urea molar ratio). Electrode was flame-annealed and cooled down in CO atmosphere until the surface was fully covered by a protective carbon monoxide (CO) layer. Prior to experiments, the removal of surface CO was performed by electrochemical oxidation. CO reactivity on Pt(111) was different depending on the IL nature. While CO is oxidised to CO₂ in [Emmim][Tf₂N], in DES CO remains and restructures leading an order-disorder transition. For both liquids, the proposed method allows obtaining neat blank cyclic voltammograms, demonstrating that the adsorption of CO is a useful tool to protect high catalytic surfaces such as Pt in contact with ILs.

As the final purpose is the evaluation of the feasibility of CO treatment in ILs and the general trends of both types of ILs on the modification of Pt(111) single crystal surface with metallic nickel nanostructures, nickel electrodeposition on Pt(111) surface was explored in both [Emmim][Tf₂N] and DES by using classical electrochemical techniques such as cyclic voltammetry and chronoamperometry, and deposits were characterized by FE-SEM.

**Submitted*

1) Introduction

The incorporation of Ionic Liquids (ILs) as novel electrolytes for many reactions of interest in electrochemistry has motivated the study of their interactions with highly active materials such as Pt, Ir or their alloys. These metals show different activity dependent on their crystallographic orientation¹⁻³. For this reason, a deeper understanding of well-defined Pt(hkl)|IL interface is demanded. However, there are not sufficient works that focus on investigating the Pt(hkl):IL interface paying attention to the influence of the liquid structure¹⁻⁶. In this respect, strategies are needed to keep the Pt(hkl) surfaces in contact with the ILs clean and ordered. The high sensitivity of platinum to contamination is most likely the main reason the lack of information in this field. Traditionally, the most convenient methodology employed to pre-treat a Pt single crystal electrode was the so-called flame annealing treatment introduced in the 80's by J. Clavilier, method that usually involves the electrode quenching in water as the final step in the treatment⁷. This procedure is not valid when the solvent is an IL because it would involve the attachment of water to the surface. CO is a neutral probe that adsorbs strongly on Pt and protects the surface from the surrounding atmosphere⁸. In the search of alternative methods, we have explored the use of carbon monoxide (CO) to protect the Pt(hkl) electrodes in ILs. In aqueous electrolytes, CO can be easily removed from the surface by its electrochemical oxidation to CO₂⁹⁻¹¹. In the few reports focused on the study of CO oxidation on Pt surfaces in contact with RTILs, the authors have found that this reaction is dependent on two factors: the amount of water and, particularly, the specific nature of the anion in the RTIL^{6, 12}. These factors also determine the electrochemical stability of the RTIL (i.e the electrochemical window) and thus their availability to oxidize CO with or without overlapping with solvent oxidation. Keeping in mind previous results obtained in ILs and aqueous media, CO coverage and oxidation was investigated and evaluated as a tool to maintain the cleanliness and to protect the Pt surfaces after the flame annealing and during the transfer to either [Emmim][Tf₂N] or DES. For this study, a Pt(111) single crystal was employed.

As evaluation of the feasibility of CO treatment in ILs we have checked the Ni electrodeposition on a previously pre-treated Pt(111) surfaces with CO. Nickel electrodeposition on Pt(111) surfaces was explored as an example of an alternative route to modify a high catalytic and well-ordered surface such as Pt(111) with metal structures that, in addition, are hardly deposited in aqueous electrolytes^{13, 14}. Ni is a cheap and

abundant metal which combined with Pt enhances the catalytic properties of the electrode in several reactions of interest¹⁵⁻¹⁷.

2) Results

2.1) CO reaction on Pt(111)/0.1M HClO₄ aqueous blank solution

Prior to investigating the Pt(111)|IL interface, the CO pre-treatment was evaluated in a solution containing 0.1 M HClO₄. The electrode was flame-annealed and cooled down in CO atmosphere for enough time to ensure complete surface blockage, but no electrode quenching in water was carried out after the cooling down step. Figure 1A shows the cyclic voltammetry of the CO stripping on Pt(111)|0.1M HClO₄ interface after performing the pre-treatment. The main CO oxidation peak appears centred at 0.75 V vs RHE. Interestingly, the main peak is preceded by a small peak located at 0.64 V vs RHE, which origin is uncertain and could be related with the flame-annealing treatment. Once the CO was oxidized, the Pt(111) displays the common blank cyclic voltammogram reported in 0.1M HClO₄. Figure 1B shows the CO stripping on Pt(111) after holding the covered Pt(111) electrode in air, during 10 and 60 minutes respectively, overlapped with the CO stripping voltammetry from Figure 1A (the electrode was suddenly introduced in the cell after the thermic treatment). The goal of these experiments is evaluating the efficiency of CO to keep the Pt(111) surface protected during long time period. After holding the electrode for 10 and 60 minutes the Pt(111) is still fully covered by CO, and the overall charge involved in the main CO oxidation peak hardly changes (about 360 $\mu\text{C cm}^{-2}$ in all cases). The most interesting fact is that the small peak at 0.64 V recorded in Figure 1A, which involves a charge value of around 22 $\mu\text{C cm}^{-2}$, has disappeared from the voltammograms in which the covered Pt(111) electrode was hold some time in air. This result suggests that the identity of the small peak would be related with weakly adsorbed CO on the surface^{18, 19}. It is remarkable that, in the absence of electrolyte, the atmospheric oxygen is not able to oxidise the CO on the surface. Figure 1C compares the blank cyclic voltammograms recorded after CO oxidation for the three previously described exposition times to the atmosphere after the CO pre-treatment. Voltammograms are practically identical, although a small decrease in charge was observed in the anion adsorption region (feature at 0.85 V). The loss in the recorded charge is nearly negligible,

and therefore, the CO pre-treatment is validated as a tool to keep the Pt(111) surface clean and ordered without using water quenching.

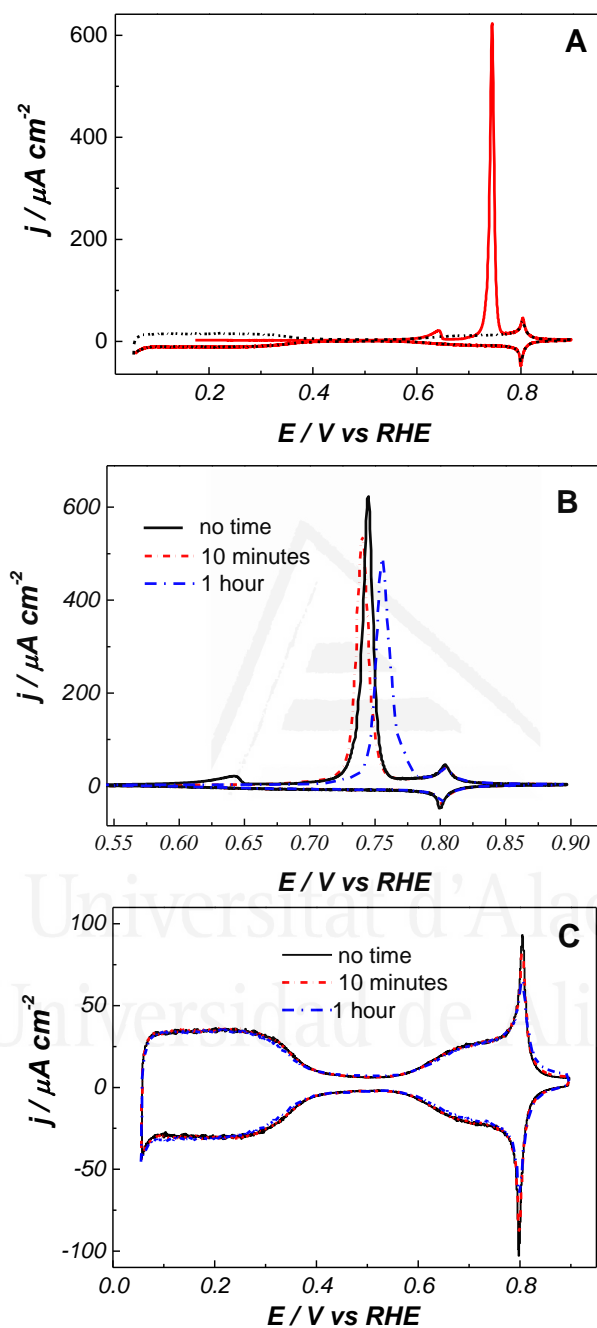


Figure 1: A) CO stripping on Pt(111)/0.1 M HClO₄ (solid line) and blank cyclic voltammogram (dashed line), at 20mV/s. B) CO stripping voltammetric profiles for different Pt(111) pre-treatments, at 20 mV/s. C) Blank cyclic voltammograms of the Pt(111)/0.1 M HClO₄ after oxidizing the CO, at 50mV/s.

2.2) CO reaction on Pt(111)|[Emmim][Tf₂N] blank solution

After carrying the CO oxidation study in classical 0.1 M HClO₄ electrolyte, the conditions for the study of Pt(111)|[Emmim][Tf₂N] interface were investigated. The electrode was pre-treated with CO following the protocol established in the previous section. The electrode was flame-annealed and cooled down in CO atmosphere. Due to the important moisture sensitivity of the [Emmim][Tf₂N], the Pt(111) electrode was transferred inside the glove box. As the CO monolayer was demonstrated stable on Pt(111), even after prolonged exposure to the O₂ containing atmosphere, the Pt(111) surface remained covered by CO during the time spent moving the electrode to be introduced in the glove box. Figure 2A shows the voltammetric CO stripping profile in [Emmim][Tf₂N] liquid, displaying a very sharp peak at 1.1 V vs Fc⁺/Fc preceded by less prominent broad peaks (arrows in the figure). After attaining this sharp peak, the scan is reversed to avoid the solvent oxidation. The second cycle shows a clear increase of the capacitive current (Figure 2A inset), and no current related to CO oxidation was detected, evidencing that the CO was completely removed during the first scan. The electrochemical window in this second scan was widened as the anodic limit of solvent decomposition is displaced positively. Some broad peaks appear in the capacitive region within -1.0 V and 1.0 V vs Fc/Fc⁺ after CO oxidation (inset Figure 2A). By cycling successively within the potential window of the RTIL, these peaks tend to disappear (Figure 2B) and the Pt(111)|[Emmim][Tf₂N] interface displays a cyclic voltammogram that is basically a featureless pseudo-capacitance that extends up to 3.5 V. The voltammetric characterization suggests that the origin of the recorded broad peaks in the first scan is related to post-kinetic diffusion controlled reactions after CO oxidation in RTIL. In order to get more insights about the origin of these peaks, cyclic voltammetry experiments were carried out at high speed rate (500mV/s) to reduce the diffusion limitation (Figure 2C). The voltammogram displays two oxidation peaks at -0.07 V and 0.30 V and their counterparts at -0.25 V and 0.049 V, approximately. Looking for an explanation of the origin of these broad peaks, similar features were observed and reported in previous works and assigned to hydrogen adsorption/reaction on Pt(111) in contact with [Emmim][Tf₂N]³. To confirm that the voltammetric peaks in Figure 2C are related with hydrogen reaction on Pt(111), two cyclic voltammograms of Pt(111) in [Emmim][Tf₂N] were recorded, the first one before (black line) and the second one after saturating the RTIL with hydrogen gas (red line, Figure 2D). Figure 2D shows a

voltammetric profile for Pt(111)|[Emmim][Tf₂N] that does not contain singular characteristic feature, only a double layer structure, but analogous peaks to those shown in Figure 2C, emerge when the scan was performed in presence of hydrogen in the bulk RTIL electrolyte.

These results strongly support that CO oxidation mechanism in [Emmim][Tf₂N] involves water (water content in the RTIL <10ppm). Then, the proposed mechanism pathway would follow:



Protons would be reduced to hydrogen in the following cycles. The hypothesis is that water could concentrate in the interfacial region at strong surface polarization, and reacts with CO to produce CO₂, as was proposed in other cases^{6, 20}. As the amount of water in the RTIL is very low, these interfacial protons are progressively replaced by the species of the RTIL, which would explain the evolution of the peaks in the blank voltammogram (Figure 2C), that ends up disappearing by successive cycling. These results are not especially surprising, since it was claimed before that CO oxidation to CO₂ in RTIL media necessary involves water presence⁶.

Universitat d'Alacant
Universidad de Alicante

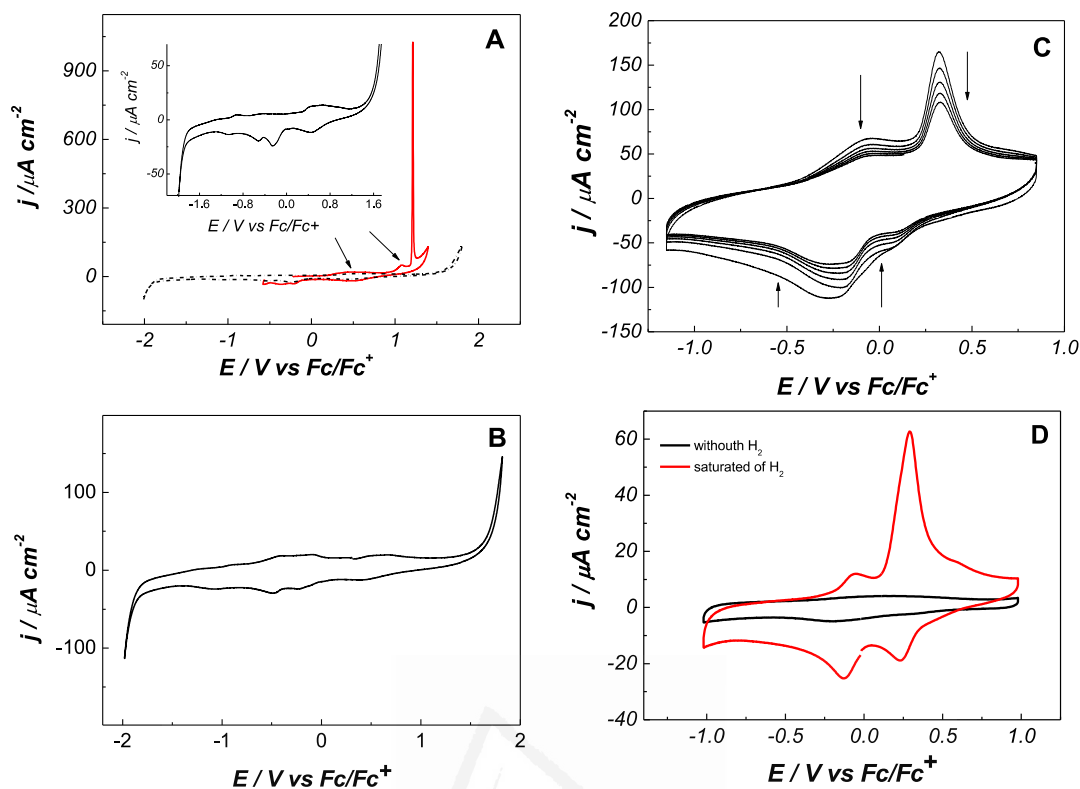


Figure 2: Cyclic voltammograms of the Pt(111) in contact with [Emmim][Tf₂N]: A) consecutive scans: red solid line) first scan showing the CO stripping, black dashed line) second scan, inset) Pt(111)|[Emmim][Tf₂N]. At 20mV/s. B) Blank cyclic voltammogram at 50mV/s. C) Blank voltammogram of Pt(111)|[Emmim][Tf₂N] after CO oxidation at 500mV/s. D) Pt(111)|[Emmim][Tf₂N] cyclic voltammograms: red line) solution saturated with H₂ gas. Black line) blank voltammogram without hydrogen at 50mV/s.

To further analyse the CO oxidation result, the involved charge in the voltammetric region of CO stripping was calculated. The obtained value ranges between 700-900 $\mu\text{C cm}^{-2}$ without background subtraction. This value is considerable higher than the reported in aqueous electrolytes for Pt electrodes, which usually ranges to 320 $\mu\text{C cm}^{-2}$, after subtracting the double layer and anion adsorption contributions. It must be stressed that CO coverage must be the same as the one characterised in aqueous media, since CO adlayer is formed before involving water or IL. The higher value obtained could evidence anion adsorption on the surface on the sites that freed after the oxidation of CO. Similar phenomena were observed in aqueous electrolytes at conditions at which anion adsorption was coupled with CO stripping, and then the apparent charge density

associated to the voltammetric CO stripping increased around $437 \mu\text{C cm}^{-2}$ ²¹. It must be highlighted that F.A. Hanc-Scherer et al. investigated similar RTILS but under the presence of thousands of ppm of water⁶, and they calculated large CO oxidation charges densities, even higher than $4000 \mu\text{C cm}^{-2}$. Authors claimed that CO oxidation was coupled with the oxidation of the RTIL. In the present work, partial oxidation of the IL, overlapped with the CO stripping, could also explain the excess in the charge density but, compared with the results reported in previous works, the oxidation of the solvent appears to be smaller and slightly decoupled from CO oxidation, most likely because of the lowering in water content in the bulk. However, it must be remarked that F.A. Hanc-Scherer et al.⁶ integrated a larger potential interval centred at the CO peak oxidation potential, while we have restricted accurately the oxidation potential limit in the voltammetric experiments to avoid the production of undesirable products in the reverse scan, as well as the surface oxidation.

2.3) CO reaction on Pt(111)/ChCl:urea DES blank solution

The proposed procedure to pre-treat the Pt(111) was also used in DES. The CO covered electrode was transferred to the cell filled with DES and the voltammetric experiment was carried under Ar atmosphere. Nevertheless, it must be mentioned that the DES contains around 1% of water at the beginning of the experiments, even after a careful drying procedure under high vacuum^{22, 23}. Figure 3 shows the CO oxidation on Pt(111) in DES. The CO oxidation overlaps with the solvent oxidation. The fact that the current density displays hysteresis in the reverse scan (as pointed out by the arrows) is evidence that CO is co-oxidized together with the solvent. The solvent oxidation produces some undesirable products that are reduced in the reverse scan (broad peak named as x in Figure 3). Other particularity is that, in the subsequent voltammetric scan, the oxidation onset of the solvent is slightly shifted to less positive potential values, i.e., solvent decomposition is enhanced (Figure 3 inset), likely because CO blockage on Pt(111) was eliminated. As a difference from the behaviour in the RTIL, where the electrochemical window was sufficient to completely oxidize the CO adlayer, in the DES CO stripping overlaps with the solvent oxidation. Probably the excess of water in DES advances the solvent oxidation, reducing the electrochemical window. Another possibility could be that

CO is adsorbed on Pt(111) stronger in DES than in [Emmim][Tf₂N]. In order to explore this last possibility, attention was paid into the capacitive region.

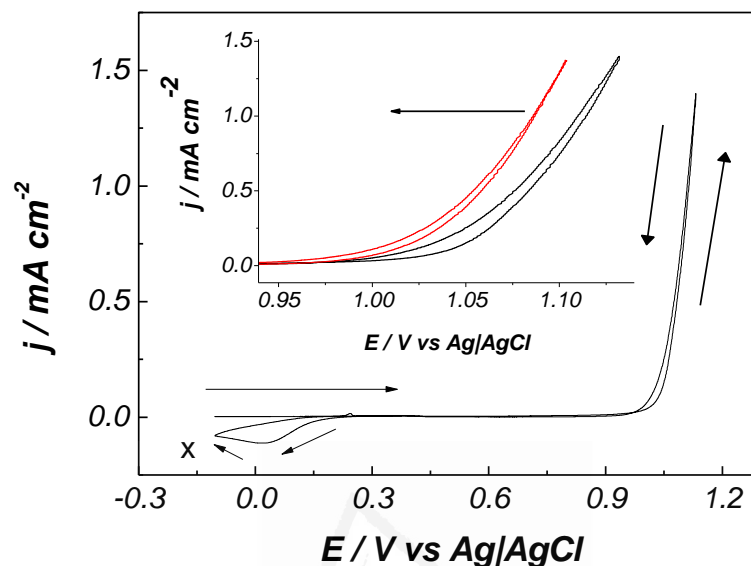


Figure 3: Cyclic voltammograms of the Pt(111) flame annealed and cooled down under CO, in contact with the DES. The inset shows the first scan (black line) and second scan (red line) at 70 °C. Scan rate at 20mV/s.

Figure 4 shows the voltammetric region of the CO-Pt(111) in contact with the DES between -0.30 and 0.60 V. A group of quasi-reversible broad peaks appear in the double layer region. These new peaks (Figure 4Aa) only appear when the Pt(111) is covered by CO in DES, having an unknown origin. By consecutive cycling, these peaks become sharper (Fig. 4Ab) until attain a maximum current value (Fig. 4Ac). However, if successive scans were applied, the current of these peaks decreases (Fig. 4Ad) and finally disappear leading a wider capacitive voltammetric region (Fig 4Ae). These sharp peaks appear superimposed to a relative constant capacitance of 72 $\mu\text{F cm}^{-2}$, being the charge involved in the voltammetric region not higher than 50 $\mu\text{C cm}^{-2}$. This order of magnitude of these values suggests that these peaks could be ascribed to a phase transition involving the interaction of the adsorbed CO with the species of the DES²⁴, i.e., these peaks would correspond to solvent network restructuring on the CO-Pt(111) modified surface.

As shown in Figure 4B, the dissolution of the CO causes an increase of the capacitive region (up to 130 mF cm^{-2}). The interest for the purpose of the present work remains on the fact that adsorbed CO can be removed by successive cycling between indicated potential limits (-0.3 and 0.6 V vs Ag|AgCl). Figure 4C shows the blank cyclic voltammogram of the Pt(111) in contact with the DES after electrochemically removing the CO. The cyclic voltammogram shows a potential window not larger than 2V, shorter than the one displayed by [Emmim][Tf₂N], evidencing the lower electrochemical stability of the DES in comparison with the RTIL. The blank cyclic voltammogram shows a capacitive region between -0.50 V and 0.70 V vs Ag|AgCl and a group of redox peaks close to the solvent reduction. The couple of redox peaks could be related with the hydrogen reduction-oxidation reaction consequence of the urea (hydrogen bond donor) presence and the residual water in bulk. Similar voltammetric features were previously reported in protic ILs^{12, 25}. It is worth to note that cyclic voltammetry recorded in DES after flame-annealing and cooling the Pt(111) down in the argon atmosphere of the cell (not shown) was virtually identical to that obtained after CO dissolution, confirming that no CO remains in this case on the surface.

From the previous voltammetric responses of the Pt(111)|IL interface, it is evidenced that reactivity towards the CO oxidation is dependent on the employed electrolyte. While in [Emmim][Tf₂N] CO oxidation takes place by reaction with interfacial water, CO strongly interacts with DES species undergoing a reorganization in the double layer region. Since this reaction is of paramount interest in terms of sustainability, it deserves special attention and more work is required to establish the parameters that govern the mechanistic pathway of CO adsorption/oxidation in non-aqueous electrolytes. For the purposes of the present work, CO has been proposed as a useful tool to keep clean and ordered the Pt(111) surface in contact with both DES and RTIL.

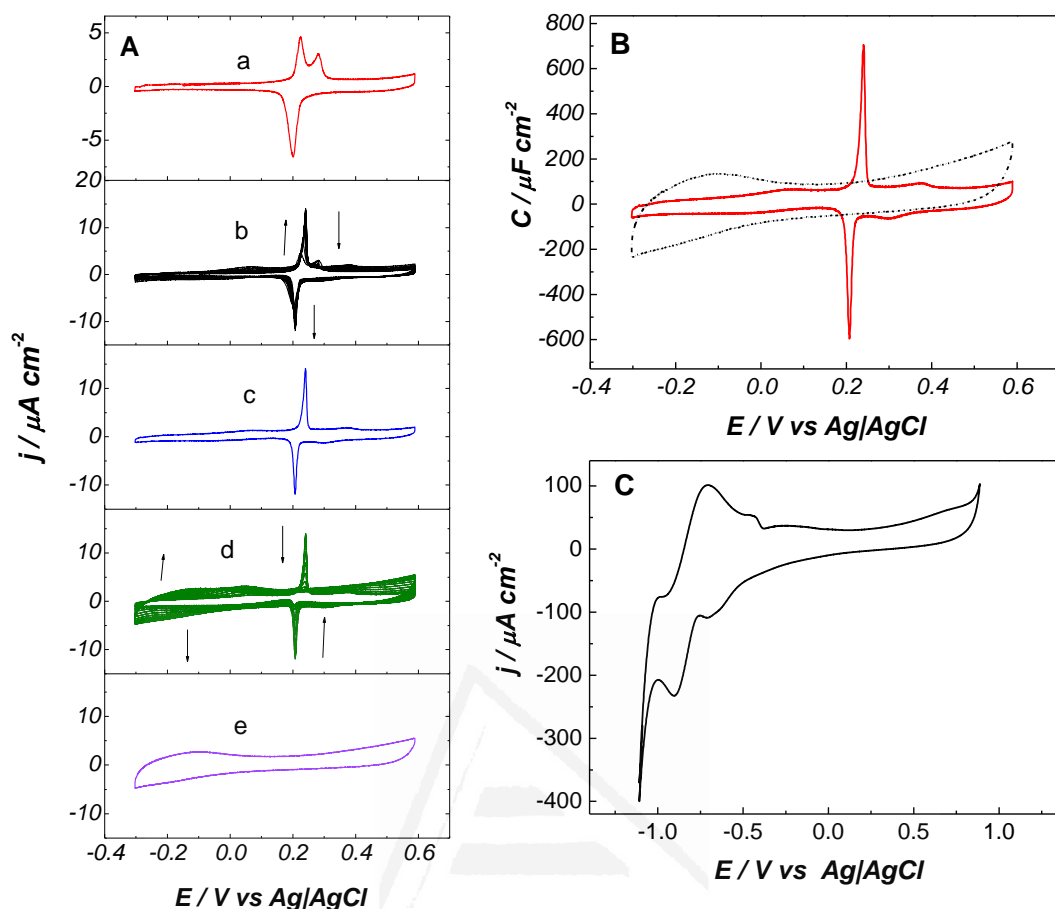


Figure 4: Cyclic voltammograms of the Pt(111)/DES interface at 70°C: A) consecutive scans of the double layer region when the Pt(111) is covered by CO. B) double layer region when, solid line) Pt(111) is covered by CO, dashed line) Pt is free of CO. At 20mV/s. C) blank cyclic voltammetry at 50mV/s when the Pt(111) is free of CO.

2.4) Ni deposition on Pt(111) in the ILs

Nickel electrodeposition in [Emmim][Tf₂N] was investigated on Pt(111) pre-treated with CO. Taking advantage from the fact that the RTIL shows a large electrochemical window, the CO stripping was carried out in the same solution containing 50 mM Ni[Tf₂N]₂ + [Emmim][Tf₂N], followed by successive cycling in the double layer region until reaching a stationary profile. Figure 5A shows the cyclic voltammetry for the nickel deposition on Pt(111) overlapped with the blank cyclic voltammogram. The voltammetric window allows the Ni deposition with negligible solvent co-reduction, although high negative applied potentials are required for nickel electrodeposition. In

addition, the Ni(II) reduction/dissolution is a very irreversible process and around 1V separates the onset of the nickel reduction and the onset of the nickel oxidation. Similar results were reported by Katayama et. al using other RTILs based on the [Tf₂N] anion²⁶. The authors attributed the high irreversibility of the process to the particular nature of the Metal|IL interface. The presence of the cation (a large-size organic ion) on the surface at those negative potentials would hinder the electron transfer between the metal precursor (Ni(II)) and Pt(111). So, high overpotential is needed to overcome this energetic barrier. The irreversibility of the process could be also as a consequence of the slow restructuration of the solvent network in the reverse direction of the scan or it can also be related to the inert condition of nickel towards its deposition that is also observed in aqueous medium²⁷⁻²⁹.

To carry out the nickel electrodeposition, potentials close to the onset of voltammetric process were applied, because a dark liquid surrounding the surface was observed forming at higher potential values, related with the formation of Ni nanoparticles and the deposit was not adherent. Katayama et al. reported also the formation of metal nanoparticles at high applied potentials due to the fact that the ionic species in the electrolyte, especially the cation, inhibited the growth of the deposit favouring nanostructures with low adherence^{27, 30}.

Figure 5B shows the chronoamperometric transient of Ni(II) deposition applying -0.70 V vs Fc/Fc⁺. The j-t transient shows a slow current increase until a maximum is attained around at 150s, just evidencing the slowness of the process. Then, the current falls down with time. The profile of the recorded j-t transient suggests that the nickel nucleates and grows under diffusion control (3-D nucleation and mass controlled growth mechanism).

Figure 5C shows the FE-SEM image corresponding to the nickel deposit onto Pt(111) under the conditions of Figure 5B . Under these conditions, nickel nanoclusters homogeneously covering the entire surface, sized <100 nm are formed, without evidencing any grade of porosity (Figure 5D). The absence of holes or porosity supports that nickel deposition takes place without the interference of the solvent reduction, thus confirming the ability of [Emmim][Tf₂N] to readily modify the Pt(111) single crystal with nickel.

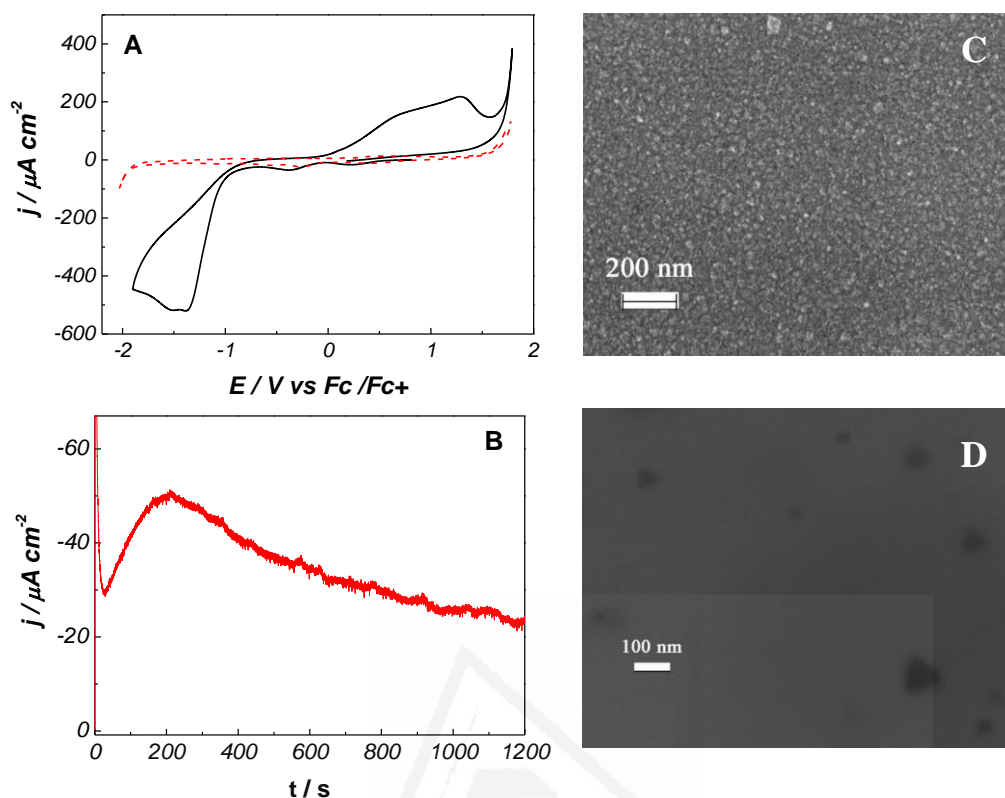


Figure 5: A) Cyclic voltammogram at 20mV/s of the nickel deposition in 50mM $\text{Ni}[\text{Tf}_2\text{N}]_2 + [\text{Emmim}][\text{Tf}_2\text{N}]$ solution. The dashed line corresponds to the blank. B) $j-t$ transient recorded at -0.700V. C) FE-SEM image of nickel deposit obtained at 40 mC cm^{-2} at -0.70V. D) FE-SEM bare Pt(111).

Before investigating Ni(II) deposition in DES, a temperature study was carried out, from which 0.1 M Ni(II) plus DES at 70 °C were selected as the optimal conditions to perform Ni(II) deposition on Pt electrode (not shown). The high viscosity of the media hinders the Ni(II) deposition at lower temperatures. An increment of the nickel (II) concentration (twice that the employed in the RTIL) was also employed.

Figure 6A shows the cyclic voltammogram for 0.1M Ni(II) electrodeposition on Pt(111) in DES. The dashed line corresponds to the blank cyclic voltammetry within the potential limits where the nickel electrodeposition was carried out. Although the electrochemical window of the DES is considerable shorter than in $[\text{Emmim}][\text{Tf}_2\text{N}]$, it is sufficient to allow the nickel deposition. When the nickel deposit is present on the Pt(111) surface, the limit for the DES reduction increases because nickel is less catalytic. The

solvent reduction involves hydrogen reaction (broad peak labelled as x in the anodic scan of the Pt(111)|DES cyclic voltammogram)³¹⁻³³.

The cyclic voltammetry from the Ni deposition shows two peaks in the reduction scan (a and b) thus suggesting a change in the nickel deposition mechanism. According to the literature, these two peaks are related with different hydrogenated Ni species, i.e., Ni containing different fractions of hydrogen in its network (α -Ni and β -Ni)^{23, 34}. Chronoamperometric transients were recorded at low applied overpotential to minimize solvent reduction (Figure 6B). As in RTIL, the j-t transient evidences nucleation and growth mechanism (Figure 6B), being the maximum current value centred at around 100 s, evidencing that the growth in this media is also kinetically slow.

Ni nanostructures obtained in DES have a size that approach to 100 nm, i.e. they are higher than those obtained in [Emmim][Tf₂N], although the sample has been prepared under the same charge for comparison (Figure 6C). This result evidences the influence of the electrolyte. Modulation of Ni nanostructures is possible according the selected IL medium. The Ni deposit in DES is also homogenous and does not shown signs of porosity if low potentials were applied.

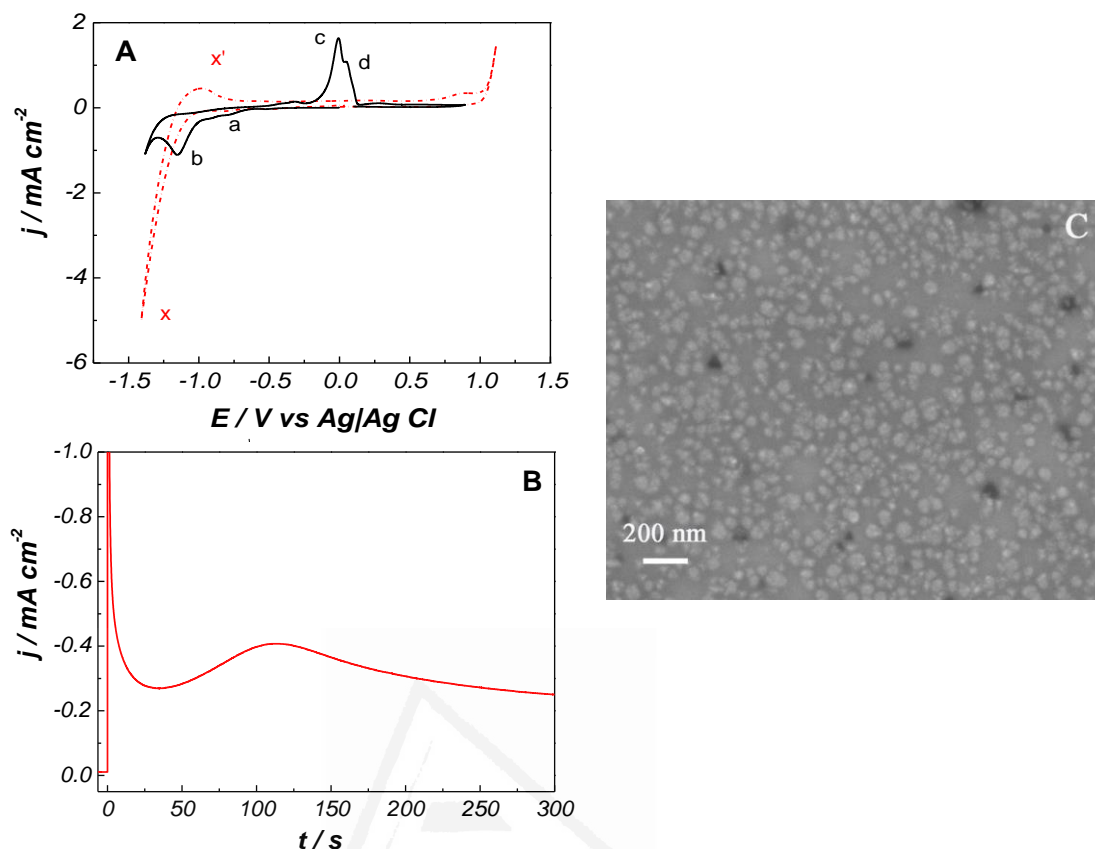


Figure 6: A) Cyclic voltammogram of the nickel deposition on Pt(111) from a 0.1 M NiCl₂ + DES solution. The dashed line corresponds to the blank cyclic voltammetry at 20 mV/s. B) *j*-*t* transients recorded at -1.0 V. C) FE-SEM images of the Ni deposit obtained at -0.98 V and -40 mC cm⁻².

3) Conclusions

An strategy to pre-treat the Pt(111) substrate ensuring both surface ordering and cleanness in IL media was proposed. The method consists on protecting the surface with CO, and later stripping it electrochemically to CO₂. RTIL possess an electrochemical window that allows the CO stripping within the potential limits, but the DES has not enough potential window and the CO oxidation overlaps with the oxidation of the solvent. In the RTIL, the low amount of water impurities promotes the CO oxidation, but in the case of the DES, the CO strongly interacts with species of the DES and cannot be oxidized at moderate applied potentials. In addition, the cyclic voltammetry of the CO-

Pt(111)|DES displays a couple of sharp peaks in the capacitive zone. These peaks were associated to a solvent restructuration process involving the CO adsorbed on Pt(111). The CO does not remain stable if consecutive cycling is carried out. These results show the complexity of CO reactivity on Pt in IL media. Different parameters may govern the pathway reaction mechanism, including the different properties of the interfacial Pt|IL region that highly influence the CO oxidation reaction. However, for the goal of this work, CO is proved as a valuable tool to protect the surface and can be used in IL media to investigate platinum single crystal electrodes, keeping the surface ordering.

Once demonstrated that CO allows obtaining reliable blank cyclic voltammograms of Pt(111) in contact with both DES and [Emmim][Tf₂N] liquids, the applicability of these two ionic liquids to modify Pt(111) with Ni was evaluated. Both ILs have shown chemical differences that influence the nickel deposition in several ways. The [Emmim][Tf₂N] has a potential window sufficiently wide for the nickel electrodeposition, allowing the nickel deposition without solvent reduction interference. Nanostructures of nickel with size smaller than 100 nm can be obtained. The DES is less chemically stable and higher both nickel concentration and temperature are needed to moderate the effect of the viscosity of the medium. The reduction of the solvent overlaps with the Ni deposition, but the Ni(II)-solvent co-reduction can be avoided applying low potentials, at which Ni nanostructures of rounded shape were obtained, slightly bigger than those in the RTIL. Although [Emmim][Tf₂N] has a wider potential range for Ni deposition this is not exploitable due to the lack of deposit adherence observed at the higher applied potentials. ChCl:urea DES was also found to be a good candidate for the surface modification .

4) Methods

The RTIL [Emmim][Tf₂N] was purchased from Iolitec in the highest available quality (99% < 60ppm halides, < 60ppm water). The RTIL was then transferred to an argon glove box (Mbraun, USA, H₂O <1 ppm, O₂ <1%). Before carrying the experiments, around 1-2 mL of [Emmim][Tf₂N] were dried under vacuum, heating (80°C) and stirring conditions (P<0.0025mPas, 5 hours). Then, the stirring was stopped and activated molecular sieves (3Å) were added in order to remove residual water and impurities, according to the Kolb's procedure³⁵. Afterwards the water content in the RTIL was measured by Karl Fisher Titration, measuring a value of less than 10 ppm. The Ni[Tf₂N]₂

salt was purchased from Alfa Aesar in the highest quality available (98%). This salt was dried overnight under vacuum and temperature conditions (150°C) before adding to the RTIL. The hydrated salt was initially blue and changed to yellow evidencing the drying. The prepared nickel concentration in the [Emmim][Tf₂N] was 0.05M.

Both the Choline chloride (ChCl) and the urea were purchased in high purity quality (99%) from Merck. The DES was prepared by mixing both components under a temperature not higher than 50°C, until a liquid was obtained stable at room temperature. The molar ratio between both salts in the eutectic mixture was 1ChCl: 2urea³⁶. Then the liquid was transferred to a glass recipient connected to a vacuum pump and dried under vacuum ($P < 0.002$ mbar), stirring and heating conditions ($T < 50^\circ\text{C}$) overnight. The water content, measured electrochemically, was around 1%. Ni(II) solution was prepared, from NiCl₂6H₂O salt of 99% purity grade from Merck. This salt was dried at 100°C overnight. After that, a Ni(II) solution in DES was prepared with 0.1M concentration. In order to dissolve the nickel salt in the DES, the mixture was stirred during 24 h under vacuum and heating conditions ($t < 50^\circ\text{C}$).

Suprapure HClO₄ from Merck was purchased for the CO oxidation tests in aqueous solution.

The working electrode was a bead type Pt(111) pre-treated by flame-annealing and cooled down under the presence of CO, until the surface was completely blocked by the CO.

A three-electrode cell was employed to carry out the experiments. As a reference electrode, a quasi-reference silver wire was used for the experiments carried in [Emmim][Tf₂N] being the potential referred to the Fc⁺/Fc redox pair. In the DES, Ag|AgCl reference electrode was used. In aqueous solutions, a reversible hydrogen electrode (RHE) was employed. As a counter electrode, a platinum wire spiral was employed in all cases. Experiments with [Emmim][Tf₂N] were carried at 25°C inside a glove box, while for the DES a thermostated cell was employed, keeping the temperature at 70°C. In addition, the electrochemical cell was kept under Ar atmosphere to minimize further hydration from the environment when the DES was the employed electrolyte.

Either a Biologic potentiostat BP300 or a μ -Autolab GPES potentiostat were used to carry both cyclic voltammetric and chronoamperometric measures. A JEOL field emission scanning electron microscopy FE-SEM was used to characterize the deposits.

5) References

- (1) Montiel, M.; Solla-Gullón, J.; Sánchez-Sánchez, C., Electrochemical reactivity and stability of platinum nanoparticles in imidazolium-based ionic liquids. *Journal of Solid State Electrochemistry* **2015**, 1-10.
- (2) Navarro-Suarez, A. M.; Hidalgo-Acosta, J. C.; Fadini, L.; Feliu, J. M.; Suarez-Herrera, M. F., Electrochemical oxidation of hydrogen on basal plane platinum electrodes in imidazolium ionic liquids. *Journal of Physical Chemistry C* **2011**, *115* (22), 11147-11155.
- (3) Sandoval, A. P.; Suarez-Herrera, M. F.; Feliu, J. M., Hydrogen redox reactions in 1-ethyl-2,3-dimethylimidazolium bis(trifluoromethylsulfonyl)imide on platinum single crystal electrodes. *Electrochemistry Communications* **2014**, *46*, 84-86.
- (4) Sebastián, P.; Sandoval, A. P.; Climent, V.; Feliu, J. M., Study of the interface pt(111)/[Emmim][NTF₂] using laser-induced temperature jump experiments. *Electrochemistry Communications* **2015**, *55*, 39-42.
- (5) Hanc-Scherer, F. A.; Montiel, M. A.; Montiel, V.; Herrero, E.; Sanchez-Sanchez, C. M., Surface structured platinum electrodes for the electrochemical reduction of carbon dioxide in imidazolium based ionic liquids. *Physical Chemistry Chemical Physics* **2015**, *17* (37), 23909-23916.
- (6) Hanc-Scherer, F. A.; Sanchez-Sanchez, C. M.; Ilea, P.; Herrero, E., Surface-sensitive electrooxidation of carbon monoxide in room temperature ionic liquids. *ACS Catalysis* **2013**, *3* (12), 2935-2938.
- (7) Clavilier, J.; Faure, R.; Guinet, G.; Durand, R., Preparation of monocrystalline Pt microelectrodes and electrochemical study of the plane surfaces cut in the direction of the {111} and {110} planes. *Journal of Electroanalytical Chemistry and Interfacial Electrochemistry* **1980**, *107* (1), 205-209.
- (8) Kibler, L. A.; Cuesta, A.; Kleinert, M.; Kolb, D. M., In-situ stm characterisation of the surface morphology of platinum single crystal electrodes as a function of their preparation. *Journal of Electroanalytical Chemistry* **2000**, *484* (1), 73-82.
- (9) Feliu, J. M.; Orts, J. M.; Fernandez-Vega, A.; Aldaz, A.; Clavilier, J., Electrochemical studies in sulphuric acid solutions of adsorbed co on pt (111) electrodes. *Journal of Electroanalytical Chemistry* **1990**, *296* (1), 191-201.
- (10) Climent, V.; Feliu, J. M., Thirty years of platinum single crystal electrochemistry. *Journal of Solid State Electrochemistry* **2011**, *15* (7), 1297.
- (11) Clavilier, J.; Albalat, R.; Gomez, R.; Orts, J. M.; Feliu, J. M.; Aldaz, A., Study of the charge displacement at constant potential during co adsorption on Pt(110) and Pt(111) electrodes in contact with a perchloric acid solution. *Journal of Electroanalytical Chemistry* **1992**, *330* (1), 489-497.
- (12) Ejigu, A.; Walsh, D. A., The role of adsorbed ions during electrocatalysis in ionic liquids. *Journal of Physical Chemistry C* **2014**, *118* (14), 7414-7422.

-
- (13) Zhang, Q.; Wang, Q.; Zhang, S.; Lu, X.; Zhang, X., Electrodeposition in ionic liquids. *ChemPhysChem* **2016**, *17* (3), 335-351.
- (14) Abbott, A. P.; McKenzie, K. J., Application of ionic liquids to the electrodeposition of metals. *Physical Chemistry Chemical Physics* **2006**, *8* (37), 4265-4279.
- (15) Subbaraman, R.; Tripkovic, D.; Strmcnik, D.; Chang, K.-C.; Uchimura, M.; Paulikas, A. P.; Stamenkovic, V.; Markovic, N. M., Enhancing hydrogen evolution activity in water splitting by tailoring $\text{Li}^+\text{Ni}(\text{OH})_2/\text{Pt}$ interfaces. *Science* **2011**, *334* (6060), 1256-1260.
- (16) Stamenkovic, V. R.; Fowler, B.; Mun, B. S.; Wang, G.; Ross, P. N.; Lucas, C. A.; Markovic, N. M., Improved oxygen reduction activity on $\text{Pt}_3\text{Ni}(111)$ via increased surface site availability. *Science* **2007**.
- (17) Ledezma-Yanez, I.; Wallace, W. D. Z.; Sebastián-Pascual, P.; Climent, V.; Feliu, J. M.; Koper, M. T. M., Interfacial water reorganization as a pH-dependent descriptor of the hydrogen evolution rate on platinum electrodes. *Nature Energy* **2017**, *2* (4).
- (18) Suchorski, Y.; Drachsel, W.; Rupprechter, G., High-field versus high-pressure: Weakly adsorbed co species on $\text{Pt}(111)$. *Ultramicroscopy* **2009**, *109* (5), 430-435.
- (19) Farias, M. J. S.; Busó-Rogero, C.; Gisbert, R.; Herrero, E.; Feliu, J. M., Influence of the co adsorption environment on its reactivity with (111) terrace sites in stepped Pt electrodes under alkaline media. *The Journal of Physical Chemistry C* **2014**, *118* (4), 1925-1934.
- (20) Figueiredo, M. C.; Ledezma-Yanez, I.; Koper, M. T. M., In situ spectroscopic study of CO_2 electroreduction at copper electrodes in acetonitrile. *ACS Catalysis* **2016**, *6* (4), 2382-2392.
- (21) Carol Korzeniewski, V. C., and Juan M. Feliu, Electrochemistry at pt single crystal electrodes, chapter book, electroanalytical chemistry. In *Electroanalytical chemistry a series of advances*, CRC Press: 2011; 75.
- (22) Du, C.; Zhao, B.; Chen, X.-B.; Birbilis, N.; Yang, H., Effect of water presence on choline chloride-2urea ionic liquid and coating platings from the hydrated ionic liquid. **2016**, *6*, 29225.
- (23) Sebastian, P.; Giannotti, M. I.; Gómez, E.; Feliu, J. M., Surface sensitive nickel electrodeposition in deep eutectic solvent. *ACS Applied Energy Materials* **2018**.
- (24) Sebastián, P.; Climent, V.; Feliu, J. M., Characterization of the interfaces between $\text{Au}(hkl)$ single crystal basal plane electrodes and $[\text{Emmim}][\text{Tf}_2\text{N}]$ ionic liquid. *Electrochemistry Communications* **2016**, *62*, 44-47.
- (25) Greaves, T. L.; Drummond, C. J., Protic ionic liquids: Properties and applications. *Chemical Reviews* **2008**, *108* (1), 206-237.
- (26) Zhu, Y. L.; Kozuma, Y.; Katayama, Y.; Miura, T., Electrochemical behavior of $\text{Ni}(\text{ii})/\text{Ni}$ in a hydrophobic amide-type room-temperature ionic liquid. *Electrochimica Acta* **2009**, *54* (28), 7502-7506.
- (27) Katayama, Y.; Fukui, R.; Miura, T., Electrodeposition of cobalt from an imide-type room-temperature ionic liquid. *Journal of the Electrochemical Society* **2007**, *154* (10), D534-D537.
- (28) Tułodziecki, M.; Tarascon, J. M.; Taberna, P. L.; Guéry, C., Importance of the double layer structure in the electrochemical deposition of co from soluble Co^{2+} based precursors in ionic liquid media. *Electrochimica Acta* **2014**, *134*, 55-66.
-

-
- (29) Tułodziecki, M.; Tarascon, J. M.; Taberna, P. L.; Guéry, C., Non-equilibrium ionic liquid-electrode interface at elevated temperature and its influence on Co^{2+} reduction process. *Journal of the Electrochemical Society* **2016**, *163* (8), D355-D365.
- (30) Katayama, Y.; Oshino, Y.; Ichihashi, N.; Tachikawa, N.; Yoshii, K.; Toshima, K., Electrochemical preparation of palladium nanoparticles in bis(trifluoromethylsulfonyl)amide ionic liquids consisting of pyrrolidinium cations with different alkyl chain lengths. *Electrochimica Acta* **2015**, *183*, 37-41.
- (31) Laursen, A. B.; Varela, A. S.; Dionigi, F.; Fanchiu, H.; Miller, C.; Trinhammer, O. L.; Rossmeisl, J.; Dahl, S., Electrochemical hydrogen evolution: Sabatier's principle and the volcano plot. *Journal of Chemical Education* **2012**, *89* (12), 1595-1599.
- (32) Lazarescu, V.; Clavilier, J., Ph effects on the potentiodynamic behavior of the Pt(111) electrode in acidified NaClO_4 solutions. *Electrochimica Acta* **1998**, *44* (6-7), 931-941.
- (33) Mernissi Cherigui, E. A.; Sentosun, K.; Bouckenooqe, P.; Vanrompay, H.; Bals, S.; Terryn, H.; Ustarroz, J., Comprehensive study of the electrodeposition of nickel nanostructures from deep eutectic solvents: Self-limiting growth by electrolysis of residual water. *Journal of Physical Chemistry C* **2017**, *121* (17), 9337-9347.
- (34) Gómez, E.; Pollina, R.; Vallés, E., Nickel electrodeposition on different metallic substrates. *Journal of Electroanalytical Chemistry* **1995**, *386* (1-2), 45-56.
- (35) Gnahn, M.; Kolb, D. M., The purification of an ionic liquid. *Journal of Electroanalytical Chemistry* **2011**, *651* (2), 250-252.
- (36) Abbott, A. P.; Boothby, D.; Capper, G.; Davies, D. L.; Rasheed, R. K., Deep eutectic solvents formed between choline chloride and carboxylic acids: Versatile alternatives to ionic liquids. *Journal of the American Chemical Society* **2004**, *126* (29), 9142-9147.

Chapter 6

Conclusions

Universitat d'Alacant
Universidad de Alicante

CONCLUSIONS

- The Pt(111)|aqueous solution was deeply investigated with the laser induced temperature jump technique. The use of $x\text{HClO}_4 + (0.1-x)\text{M NaF}$ buffer solutions allowed to analyse pH values close to the neutrality condition (pH between 3-6). The laser technique allowed to calculate the potential of maximum entropy (*pme*) on Pt(111). The value does not depend on pH and its position remains constant in the SHE scale. Higher concentrations of fluoride enhance hydroxide adsorption kinetics due to its influence on water network reorganization related to the strong structure-maker character of fluoride.
- Ir(111)|aqueous solution interface was investigated in $\text{HClO}_4/\text{KClO}_4$ mixtures and HClO_4/NaF buffer solutions (pH between 1-5). Comparing results with previously reported on Pt(111), it was found that the *pme* shifting on Ir(111) (30 mV) is lower than that observed on Pt(111) (60mV). The *pme* of Ir(111) is lower than *pme* of Pt(111), in agreement with work function expectations. However, the *pme* differences between both metals disagreed with the reported work functions differences while increasing the pH, fact that was attributed to specific solvent influence on the interfacial properties.
- Voltammetric analysis of Pt(111)|[Emmim][Tf₂N] interface does not display characteristic surface sensitive features, the response only shows a wide capacitive region that extends up to 2.5V. The laser experiment evidences electrode potential change with the thermal perturbation, related to ionic network restructuring. As laser response was not reversible, a single value of *pme* was not available. Thermal coefficients of double layer drop displayed hysteresis behaviour according to the direction of applied potential, suggesting slow dynamics of double layer structuration and strong ion-ion or/and surface-ion interactions.
- Au(hkl)|[Emmim][Tf₂N] interface is surface sensitive. Cyclic voltammograms of the Au(hkl) basal planes displayed a pseudo-capacitive region with several sharp spikes characteristic of the orientation. The *pme* values obtained by laser

technique follow the sequence: *pme* Au(111) > *pme* Au(100) > *pme* Au(110), according to work function expectations.

- Au(poly) and Au(hkl)|DES interfaces are also surface sensitive. Using Cu(I) solution, UPD in Au(hkl) was demonstrated, being the UPD profile similar to that in excess of chloride from aqueous solutions. In DES medium, the strong influence of high chloride concentration on Cu(I) UPD is evidenced.
- On glassy carbon substrate Cu(II) electrodeposition in DES was studied. The Cu(II) electrodeposition involves two electron transfer steps well separated in the potential scale. In the DES, the stabilization of Cu(I) intermediate is allowed by complex formation. Double potentiostatic pulse was performed and its applicability to analyse nucleation mechanism was demonstrated. Smaller grain size of the structures was obtained in DES, confirming the lower surface diffusion in DES because of its higher viscosity.
- On glassy carbon, mechanistic analysis of Cu(II) electrodeposition in DES was carried out and a numerical formulation to analyse the first steps of the process was developed. The mathematical analysis provided surface concentration values of $[\text{Cu(I)Cl}_x]^{x-1}$ and free Cu(I), as consequence of the diffusion controlled first electron transfer (Cu(II) to Cu(I)). Including these values in the S-H non-dimensional model, the analysis of the nucleation and growth mechanism was allowed. The validity of the formulation was checked in chloride-excess aqueous solutions, for which basic thermodynamic information is accessible, demonstrating the accuracy of the method.
- New reformulation of the nucleation and growth S-H model was proposed, to improve the determination of kinetic and thermodynamic values such as: transference coefficient α , exchange current i_0 or free Gibbs energy variations on stable nucleus formation $\Delta G(n_c)$. The proposal was tested for the Ag(I) electrodeposition mechanism on glassy carbon in DES. Promising results are obtained although new conditions must be incorporated in the model to represent the complex situation in ionic liquid.

- In line with electrodeposition studies using ionic liquids on oriented surfaces, a method of surface protection has been proposed with good results. The use of CO as protective layer ensures a dry environment for successful surface cleanness and ordering on Pt(111) electrodes. The method was checked in water and extended to RTIL ([Emmim][Tf₂N]) and DES. In [Emmim][Tf₂N] the low amount of water allows to oxidize CO within its electrochemical window, while in DES CO oxidation overlaps with solvent oxidation. Successive cycles within the voltammetric double layer region are necessary to remove it. Preliminary analysis of Ni deposition in both ILs was carried out, demonstrating that in [Emmim][Tf₂N] the Ni deposition takes place without interference of liquid reduction. In DES, the solvent reduction slightly overlaps and a lower overpotential range was proven useful. Independently of the behaviour of the deposition process, results confirmed the usefulness of the CO to maintain the surface ordering of the Pt(111) surfaces in contact with ILs.
- Analysis of the substrate influence on Ni deposition in DES provides evidence of the different electrochemical stability of the DES upon depending of the substrate. On Pt surfaces, Ni deposition overlaps with the onset of solvent reaction, which has been demonstrated to produce different hydrogenated Ni structures (α -Ni and β -Ni), richer in hydrogen as higher overpotential is. This reaction is less favoured on glassy carbon. Hydrogen evolution leads to surface nickel passivation at high overpotentials. Morphological analysis confirmed that Ni grows forming rounded grains, larger on glassy carbon due to the higher surface diffusion. The AFM analysis confirmed the surface sensitivity of the Ni growth on Pt(111). On Pt(111), at very low charges, Ni nanoparticles aggregate forming triangular clusters, arrangement induced by the $\langle 111 \rangle$ orientation.

OUTLOOK AND FUTURE PERSPECTIVES

The present thesis has shown that both [Emmim][Tf₂N] and DES allows modulating the growth of metal nanostructures and offer the possibility to modify high active surfaces such as Pt with different metals, opening the possibility to use ILs in the synthesis or device of new catalysts in a cheap, simple and more sustainable way. The present thesis has explored the deposition of a single metal on different surfaces but it would be of high interest investigating these solvents for the deposition of alloys or other structures that involve more than one single metal. Other field of interest where ionic liquids could be employed is in the synthesis of nanoparticles or nanostructures. The high viscosity of the media and the strong interaction/adsorption of the species of the IL with metal substrate and metal precursor, joint to the fact that numerous species of ILs exist in literature, could be taken as advantage for tailoring the growth of nanoparticles. Mixtures of ILs in different proportions should be also explored for the same purpose.

However, this thesis has also shown that the description of the metal deposition mechanism in ILs is far to be trivial, several questions remain still open due to the particular nature of IL strongly influences the deposition process. New formulations or models are needed to better describe nucleation and growth mechanism, since classical formulism does not include solvent effects.

Finally, metal deposition in IL media cannot be understood without defining the parameters that govern double layer formation between substrate and IL. Although numerous studies of this topic where performed in RTILs, in the case of DES there is more uncertainty and efforts should be focused on deeply investigating these new solvents.



Universitat d'Alacant
Universidad de Alicante

Annex I:
GLOSSARY

LIST OF ABBREVIATIONS

<i>AFM</i>	Atomic Force Microscopy
<i>APIL</i>	Aprotic Ionic Liquid
<i>CV</i>	Cyclic Voltammetry
<i>DES</i>	Deep Eutectic Solvent
<i>DFT</i>	Density Functional Theory
<i>EDS</i>	Energy Dispersive Spectroscopy
<i>GC</i>	Gouy Chapman theory
<i>GCS</i>	Gouy Chapman Stern modification
<i>IL</i>	Ionic Liquid
<i>IR</i>	Infrared Spectroscopy
<i>LIPT</i>	Laser Induced Potential Transient, Laser induced temperature jump technique
<i>OPD</i>	<i>Overpotential deposition</i>
<i>PILS</i>	<i>Protic Ionic Liquids</i>
<i>RTIL</i>	<i>Room Temperature Ionic Liquid</i>
<i>S-H</i>	<i>Scharifker and Hills model</i>
<i>SEM</i>	<i>Scanning Electron Microscopy</i>
<i>STM</i>	<i>Scanning Tunneling Microscopy</i>
<i>SFG</i>	<i>Sum Frequency Generation Spectroscopy</i>
<i>UPD</i>	<i>Underpotential Deposition</i>
<i>XPS</i>	<i>X-Ray Photoelectron Spectroscopy</i>
<i>XRD</i>	<i>X-Ray Diffraction</i>

LIST OF ABBREVIATIONS FOR CATIONS AND ANIONS IN IONIC LIQUIDS

• *Cations*

$[Emim]$	1-Ethyl-2-methyl imidazolium
$[Emmim]$	1-Ethyl-2,3-dimethyl imidazolium
$[Bmim]$	1-Butyl-2-methyl imidazolium
$[Bmmim]$	1-Butyl-2,3-dimethyl imidazolium
$[C_6mim]$	1-Hexyl-2-methyl imidazolium
$[C_{10}mim]$	1-Decyl-2-methyl imidazolium
$[BMP]$	1-Butyl-1-methyl pyrrolidinium

• *Anions*

$[BF_4]^-$	Tetrafluoroborate
$[CH_3COO]^-$	Acetate
$[NO_3]^-$	Nitrate
$[MeSO_4]^-$	Methylsulfonate
$[MeSO_3]^-$	Methanesulfonate
$[PF_6]^-$	Hexafluorophosphate
$[Tf_2N]^-$, $[NTf_2]^-$	Bis(trifluoromethylsulfonyl)imide

• *DES*

$ChCl:urea$	Choline Chloride and urea
-------------	---------------------------

LIST OF SYMBOLS

<i>Symbol</i>	<i>Meaning</i>	<i>Value and unities</i>
E_{ap}	Applied potential	V
E_i	Onset potential in cyclic voltammetry	V
E_{min}, E_{max}	Potential limits in cyclic voltammetry	V
E^0	Redox standard potential	V
E_{eq}	Equilibrium potential	V
E_{ref}	Potential redox of reference electrode	V
$E^M, \Delta\phi^M$	Potential value of metallic side in M solution	V
pzc	Potential of zero charge	V
$pztc$	Potential of zero total charge	V
$pzfc$	Potential of zero free charge	V
pme	Potential of maximum entropy	V
j_t	Total current density	$A\ cm^{-2}$
j_f	Faradaic contribution to the current density	$A\ cm^{-2}$
j_c	Capacitive contribution to the current density	$A\ cm^{-2}$
j_p	Peak current density	$A\ cm^{-2}$
j^0	Exchange current density	$A\ cm^{-2}$
v	Scan rate	$V\ s^{-1}$
η	Overpotential applied	V
C_d	Differential capacitance	$F\ cm^{-2}$
C_{G-C}	Gouy-Chapman capacitance	$F\ cm^{-2}$
C_H	Helmholtz capacitance	$F\ cm^{-2}$
μ_i	Chemical potential of compound i	J/mol
ϵ	Relative dielectric constant of water	78.36 at 25°C
ϵ^0	Vacuum permittivity	$8.85 \times 10^{-12} F/m$
σ^M	Free charge density	$C\ cm^{-2}$

$\Gamma_{i..}$	Faradaic charge density or relative surface excess of ion i	$C\text{ cm}^{-2}$
$Q_{displaced}$	Charge value density displaced by CO	$C\text{ cm}^{-2}$
$Q_{surface}$	Total charge on the surface electrode	$C\text{ cm}^{-2}$
Q_{CO}	Capacitive charge after CO-M solution double layer formation	$C\text{ cm}^{-2}$
θ	Recovery value [0,1]	<i>dimensionless</i>
$q_{monolayer}$	Charge related with the formation of one monolayer i.	$C\text{ cm}^{-2}$
D^0	Diffusion coefficient	$\text{cm}^2\text{ s}^{-1}$
α	Coefficient of transference	<i>Dimensionless</i>
ω	Lateral interactions parameter	J
R	Ideal gas constant	$8.3145\text{ Jmol}^{-1}\text{ K}^{-1}$
F	Faraday constant	96485 C mol^{-1}
k	Boltzmann constant	$1.3806 \times 10^{-23}\text{ m}^2\text{ kgs}^{-2}\text{ K}^{-1}$
k^0	Standard rate constant of a charge-transfer adsorption process	<i>Dependent of reaction order</i>
T	Temperature	$K / ^\circ\text{C}$
T_m	Melting point	K
ΔT	Laser-induced temperature change	K
ΔT_0	Maximum laser-induced temperature change	K
ΔG	Free energy of Gibbs	J
ΔG^0	Standard free energy of Gibbs	J
ΔS^{dl}	Entropy of double layer formation	$J\text{ K}^{-1}$
\hat{S}_i	Eastman entropy of transport	$J\text{ K}^{-1}$
$\left(\frac{\partial E^M}{\partial T}\right)_{\sigma_M, \Gamma_H, \Gamma_{OH}, p, c_i}$	Temperature coefficient of the potential drop	$V\text{ K}^{-1}$
t_i	Transport number	<i>dimensionless</i>
z_i	Charge number of ion i	<i>Integer number</i>
$g^s(dip)$	Dipolar contribution to potential electrode	V
$g(ion)$	Ionic contribution to potential electrode	V

e	Electron charge	$1.602 \times 10^{-19} \text{ C}$
$\delta\chi^M$	Electron spillover or potential electrode modification by the solvent	V
ϕ	Work function	eV
κ_i	Thermal conductivity	$J s^{-1} m^{-1} K^{-1}$
α_i	Thermal diffusivity	$m^2 s^{-1}$
ρ	Density	$K g m^{-3}$
R	Reflectivity of the surface	<i>Dimensionless</i>
I	Intensity of the laser pulse	$J s^{-1} m^{-2}$
h	Planck's constant	$6.6261 \times 10^{-34} m^2 Kg s^{-1}$
λ	Wave length	m
ν	Frequency	s
A	Steady state nucleation constant	s^{-1}
t	Time	s
t_0	Initial time	s
k^*	Spring Constant	$N m^{-1}$



Universitat d'Alacant
Universidad de Alicante

Annex II:
RESUMEN

Este anexo contiene un resumen de la presente Tesis Doctoral. Se presentan los objetivos del trabajo y se han sintetizado los resultados más relevantes y las conclusiones generales.

A) OBJETIVOS GENERALES DE LA TESIS

Uno de los objetivos de esta Tesis es investigar las propiedades de la interfase Electrodo|IL sobre superficies orientadas, es decir electrodos monocristalinos $M(hkl)$. La electrodeposición de distintos metales en líquido iónico sobre distintos sustratos ha sido otro de los objetivos, en el que se investiga elucidar los factores que gobiernan el mecanismo de depósito electroquímico. Para ello se han utilizado dos tipos diferentes de líquido iónico:

- 1) Un “Room Temperature Ionic Liquid” (RTIL): [Emmim][Tf₂N].
- 2) Un “Deep Eutectic Solvent” (DES): la mezcla entre cloruro de colina y urea, en relación molar 1ChCl:2urea.

El [Emmim][Tf₂N] se ha seleccionado porque la metilación del carbono C2 del anillo “imidazolio” disminuye las interacciones por puentes de hidrógeno y refuerza las interacciones coulombicas. Este comportamiento, se espera que permita racionalizar mejor los resultados de la $M(hkl)|[Emmim][Tf_2N]$ interfase. El DES 1ChCl:2urea se ha escogido por su alta concentración de cloruros, especies capaces tanto de interaccionar con el sustrato como de complejar los iones metálicos a depositar. A diferencia del RTIL el DES es asequible y además fácil de preparar de forma relativamente limpia.

La estructura de la doble capa se ha estudiado con la técnica de laser pulsante (LIPT). Las superficies Pt(hkl) y Au(hkl) se han utilizado como modelos de superficie no polarizable y polarizable respectivamente. El estudio se ha recogido en los siguientes trabajos:

- Estudio de las propiedades interfaciales entre Pt(111) y Ir(111) en electrolitos acuosos a diferentes pH con LIPT.
- Estudio de las propiedades interfaciales de Pt(111) en [Emmim][Tf₂N] con LIPT.
- Estudio de la interfase Au(hkl)|[Emmim][Tf₂N] con LIPT.

La segunda parte de la Tesis se centra en el estudio de la electrodeposición de distintos metales en superficies orientadas y no orientadas en el DES:

- Análisis de la interfase Au(hkl)|DES y depósito UPD de Cu(I) en Au(hkl).
- Estudio de la formación de depósito electroquímico de plata en DES sobre carbono vítreo.
- Estudio de la formación de depósito electroquímico de cobre en DES sobre carbono vítreo.

Inicialmente se investigó las primeras etapas de procesos de electrodeposición de Cu(I) en sustratos metálicos, poli- y monocristalinos, analizando la influencia de la orientación en las primeras etapas de depósito. El estudio se apoyó en los resultados previos de la interfase M(hkl)|DES.

A continuación, se utilizó carbono vítreo para explorar la viabilidad de los procesos de depósito de metales en el DES. Se estudió el proceso de depósito electroquímico de cobre y plata. El hecho de que el exceso de cloruros estabiliza los correspondientes cationes, y la interacción débil entre el carbono vítreo y el metal a depositar ha sido útil para estudiar los procesos de nucleación y crecimiento.

En una etapa más avanzada se estudió la electrodeposición de un metal inerte, el níquel, sobre un metal electrocatalítico al hidrógeno utilizando [Emmim][Tf₂N] y DES a fin de comparar los resultados:

- Electrodeposición de Ni sobre Pt(poly) y carbono vítreo en DES.
- Electrodeposición de Ni sobre Pt(111) en DES.
- Electrodeposición de Ni sobre Pt(111) en [Emmim][Tf₂N].

En estos trabajos se han propuesto nuevas rutas que permitan modificar catalizadores metálicos con diferentes estructuras de níquel. El objetivo de estos trabajos ha sido evaluar la idoneidad de estos dos diferentes líquidos iónicos en la modificación de una superficie altamente catalítica como es el platino con níquel e investigar la posible sensibilidad superficial del proceso.

B) RESUMEN DE LOS TRABAJOS

PUBLICACIÓN A (chapter 4, section 4.1): *Study of the Pt (111)|electrolyte interface in the region close to neutral pH solutions by the laser induced temperature jump technique.*

En esta publicación se estudió la interfase Pt(111)|disolución acuosa a distintos pH (entre 3 y 6), con voltametría cíclica y láser pulsante. Para ello, se utilizó como disolución diferentes tampones fluoruro: $(0.1-x)M$ NaF + xM HClO₄. La utilización de este tampón permitió abordar el estudio de la propiedades interfaciales de Pt(111) a pH más próximos a la condición de neutralidad (pH=6). Dado que ni ClO₄⁻, ni F⁻ se adsorben específicamente en la superficie, no hay interferencia en la respuesta laser de la adsorción de otros aniones distintos al hidróxido proveniente de la disociación del agua. Los blancos voltamétricos, a cada uno de los pH, se caracterizaron por tener una región faradaica a potenciales próximos a la evolución de hidrógeno, que correspondió a la región UPD de hidrógeno (0.05-0.35V vs RHE). Por otro lado, a potenciales superiores a 0.60V vs RHE se identificó la adsorción de hidróxidos. Ambas regiones están separadas por una doble capa (Figura A1).

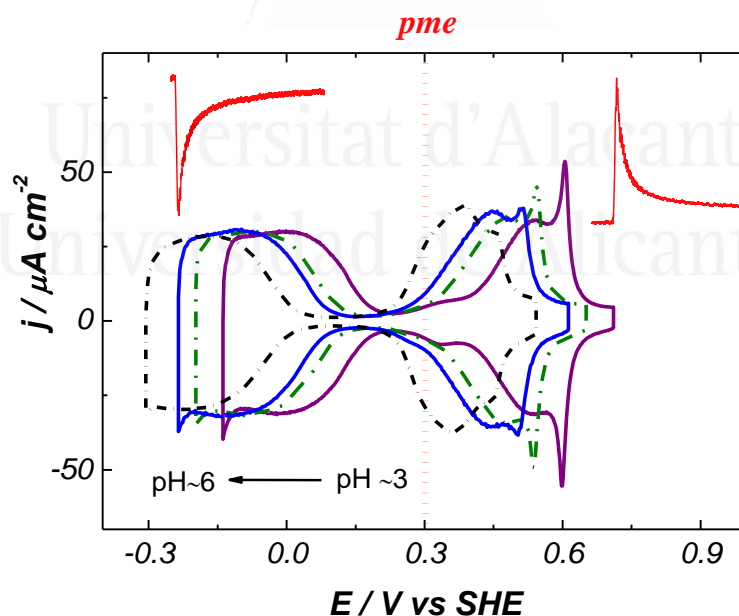


Figura A1: Voltametrías cíclicas de Pt(111)| xM HClO₄ + $(0.1-x)M$ NaF a 50mV/s y representación del pme en Pt(111).

Curiosamente, esta doble capa presenta un pico ancho capacitativo localizado antes del “onset” de adsorción de hidróxido. Pico que se va desplazando a potenciales más positivos con el aumento de pH, de forma que alcanza a solapar con la adsorción del OH⁻, hecho evidenciado por un aumento de la carga de esta región. El origen de este pico es desconocido. Una posible hipótesis es su relación con un cambio en la orientación de las moléculas de agua o con una reestructuración de la red del disolvente (Figura A1).

Las medidas realizadas con la técnica laser en cada uno de los pH mostró que el *pme* de Pt(111) se desplazaba 60mV por unidad de pH, aproximadamente, lo que equivale a decir que su posición es constante en la escala SHE. Por tanto, estos experimentos demostraron que el valor del *pme* de Pt(111) es un parámetro característico de la interfase Pt(111) independiente del pH (a pH ácido y neutro), mientras que la voltametría cíclica sí que se desplaza 60mV a potenciales más negativos en la escala SHE. El *pme* aparece centrado en el pico capacitativo, previo a la adsorción de OH⁻. Al ir aumentando el pH, tanto este pico como el *pme* se van adentrando en la región de adsorción de OH⁻. Es decir, dicho pico capacitativo a pH 3 se comporta con el pH igual que el *pme*, lo que es un claro indicio de que su origen podría estar relacionado con cambios en la orientación del agua con el campo eléctrico en superficie.

Por otro lado, en este trabajo se observó que, a potenciales más positivos de la adsorción de OH⁻, la transitoria laser mostró un comportamiento bipolar, es decir dos procesos solapados con distinta constante de velocidad. El proceso rápido correspondió a la reestructuración de la doble capa (respuesta positiva) mientras que el proceso lento (respuesta negativa) se asignó a la adsorción de OH⁻, cuyo equilibrio se desplaza debido al cambio de potencial del electrodo por la perturbación laser. Se simularon los transitorios laser obteniéndose resultados que, aunque no ajustaban bien a los datos experimentales, sí soportaban la idea de que el OH⁻ se estuviera adsorbiendo. Sin embargo, este comportamiento bipolar, a pH 3, no se observó en medio 0.099N KClO₄ + 1mM HClO₄. Dado que ni F⁻ ni ClO₄⁻ se adsorben específicamente en la superficie, se planteó la hipótesis de que, en realidad, la forma en que estos aniones interaccionan con la red de aguas es el factor que determina la distinta cinética en la disociación del agua para dar adsorción de OH⁻. El F⁻ es un “structure-maker”, reorganiza al agua, mientras que el ClO₄⁻ es un “structure-breaker” desorganiza la red de aguas. Para demostrar dicha hipótesis, se prepararon distintas concentraciones de tampón fluoruro a pH 4 y se ajustó la fuerza iónica a 0.1M con KClO₄. Mientras que los perfiles voltamétricos eran

esencialmente los mismos, la mayor relación F^-/ClO_4^- dio lugar a una transitoria laser de comportamiento bipolar más marcado, demostrando que el F^- acelera la velocidad de adsorción de OH^-

Este trabajo sirvió para demostrar que el pme en Pt(111) es un parámetro característico y descriptivo de la interfase Pt(111)|disolución acuosa, independiente del pH. Además, paralelamente, se demostró que la reactividad de un proceso que involucra al agua como reactante, en este caso adsorción específica de OH^- , puede ser modificada si se perturba la red de moléculas de agua, en este caso por la incorporación de aniones que reestructuran o desorganizan la red de aguas.

PUBLICACIÓN B (chapter 4, section 4.2): On the pH Dependence of the Potential of Maximum Entropy of Ir(111) Electrodes.

En este trabajo se investigó la interfase Ir(111)|disolución acuosa a distintos pH y utilizando distintos electrolitos. Por un lado, se utilizaron mezclas de $xM HClO_4 + (0.1-x)M KClO_4$ (0.1M) en el rango de pH de 1 a 3. Para pH 4 y 5 se preparó el tampón $xM HClO_4 + (0.1-x)M NaF$. También, se utilizaron mezclas $(0.1-x)M K_2SO_4 + xM H_2SO_4$, a $pH= 1-3$. La idea de utilizar mezclas de H_2SO_4/K_2SO_4 como electrolito es analizar el efecto que tiene la adsorción específica de HSO_4^-/SO_4^{2-} sobre la distribución de carga en la región interfacial. Para investigar la interfase Ir(111)|disolución acuosa, se combinó voltametría cíclica, la técnica de desplazamiento de CO y laser pulsante.

Con voltametría cíclica se obtuvieron los blancos voltamétricos. En ausencia de aniones que se adsorben específicamente en la superficie, los blancos voltamétricos mostraron un perfil similar al que se obtiene en Pt(111). En la ventana de potencial baja (0.0V-0.35V vs RHE) próxima a la evolución de hidrógeno, se registró una corriente farádica, tradicionalmente asignada a la UPD de hidrógeno en Ir(111). A potenciales más altos, apareció un pico ancho y centrado alrededor de 0.95V vs RHE, pico asignado como la adsorción de aniones/hidróxidos en Ir(111). Ambas regiones están separadas en la ventana de potencial por una tercera región, la doble capa. Al ir aumentando el pH, se observó que la región voltamétrica más afectada era la de UPD de hidrógeno, mientras que la zona de adsorción de aniones apenas se modificó. Curiosamente, un pico ancho centrado a 0.23V vs RHE emergió al ir aumentando el pH, la intensidad de corriente del

cual aumentaba con el pH. Este resultado voltamétrico sugirió que, en realidad, la corriente farádica registrada en la región baja de potencial en Ir(111) podría involucrar co-adsorción de hidrogeno y de hidróxidos, al contrario de lo que se observa en Pt(111).

Para un análisis más profundo de la interfase Ir(111)|(xM HClO₄ + (0.1-x)M) KClO₄ (0.1M)) o (xM HClO₄+ (0.1-x)M NaF), a los distintos pH, se utilizó la técnica de laser pulsante. Con esta técnica se determinó el *pme* de Ir(111). A pH 1, se obtuvo un valor de *pme* ≈45mV vs RHE. Comparado con el *pme* del Pt(111) en el mismo medio y pH 1 (*pme*≈350 mV vs RHE), se observó que las diferencias entre los *pme* de cada electrodo monocristalino (*pme*_{Pt(111)}}-*pme*_{Ir(111)}}) correlacionaba muy bien con las diferencias entre las funciones de trabajo de ambos metales ($\phi_{Pt(111)}/e - \phi_{Ir(111)}/e$). Sin embargo, al ir aumentando el pH, las diferencias entre los *pme* se desviaron de la diferencia entre las funciones de trabajo, resultado que se atribuyó a como el solvente interaccionaba con cada uno de los monocristales. En el caso del Ir(111), el *pme* se desplazaba 30mV por unidad de pH (en la escala RHE) a valores de potenciales mayores, mientras que en Pt(111), este desplazamiento era de 60mV (Figura A2).

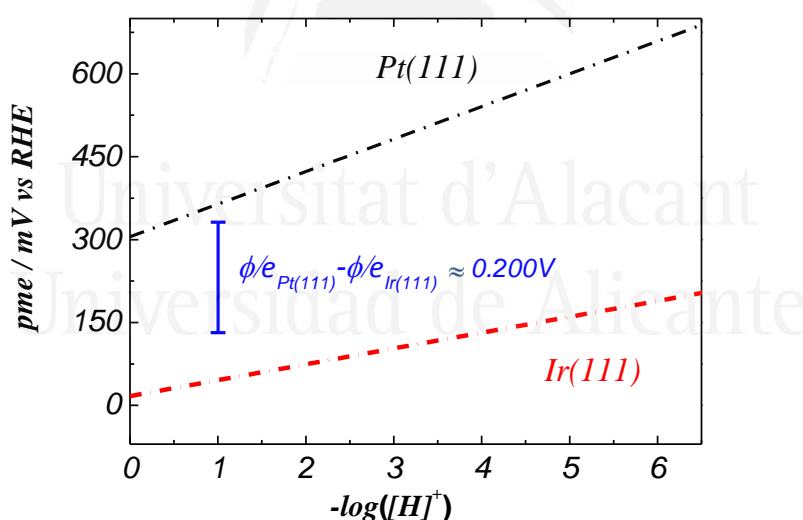


Figura A2: Representación de la variación del *pme* en Pt(111) e Ir(111), respectivamente, en función del pH.

Además, en Ir(111) el *pme* apareció siempre localizado en la región farádica cercana a la evolución de hidrógeno. Este resultado reforzó la idea de que hidrogeno e

hidróxido co-adsorben en la misma región de potencial, mientras que el pico a potenciales altos (0.95V vs RHE), correspondería a la formación de óxido metálico.

Por otro lado, las voltametrías cíclicas realizadas en medio sulfatos mostraron que el “onset” de adsorción de sulfatos apareció a valores ligeramente superiores al *pme*, reforzando que a valores ligeramente superiores tiene lugar el onset de adsorción de aniones y/o hidróxidos.

Finalmente, y para confirmar que el grupo de picos faradaicos que precede a la evolución de hidrogeno (entre 0.0V y 0.35V vs RHE) involucra adsorción de hidrógeno e hidróxido, se realizaron experimentos de desplazamiento de CO. Con estos experimentos se demostró que la adsorción de aniones se iniciaba a potenciales muy bajos y próximos al *pme* de Ir(111).

En conclusión, este trabajo es un análisis comparativo de las propiedades interfaciales de Ir(111) y de Pt(111). Este trabajo pone de manifiesto que la interface Pt(111)|disolución e Ir(111)|disolución son muy diferentes, a pesar de las similitudes químicas y físicas de ambos elementos. Las propiedades interfaciales solo se pueden entender por la distinta forma en que el disolvente (red de moléculas de agua) interacciona con cada uno de los elementos.

PUBLICACIÓN C (chapter 4, section 4.3): *Study of the interface Pt(111)|[Emmim][Tf₂N] using laser-induced temperature jump experiments.*

Teniendo en cuenta los resultados que se obtuvieron con la técnica de láser pulsante en medio acuoso para Pt(111) e Ir(111) a distintos pH, trabajo en los que se observó que el electrolito tenía una gran influencia en las propiedades interfaciales del sistema, en este trabajo se pretendió dar un paso hacia adelante, e investigar la interfase Pt(111)|[Emmim][Tf₂N] con láser pulsante. Para ello, se purificó el líquido iónico aplicando el método descrito por Kolb: secado a vacío en presencia de tamiz molecular (3Å). El contenido de agua fue menor de 50 ppm de agua. El Pt(111), se pre-trató a la llama enfriándolo después en atmosfera de H₂/Ar y protegiendo la superficie con una gota del mismo RTIL saturado de dicha atmosfera. El blanco voltamétrico mostró una región capacitiva que se extendía a 2.5-3V. Al investigar dicha interfase con láser pulsante, se observó que la respuesta láser era positiva a potenciales aplicados suficientemente

elevados, y las transitorias laser iban decreciendo en magnitud al decrecer el potencial aplicado, hasta que finalmente se invirtió, registrándose una transitoria laser negativa. Con este experimento, se demostró que la respuesta laser era dependiente del potencial aplicado, y respondía a cambios en la estructuración de la red del líquido iónico.

El resultado más interesante que se obtuvo fue que la respuesta laser en RTIL no era reversible a la dirección de cambio de potencial. Al invertir el sentido en que se aplicaba el potencial (de valores positivos (+) a valores negativos (-), y después invirtiendo la dirección de (-) a (+)), se obtuvo que la respuesta laser era, en promedio, más negativa a cada potencial aplicado comparado con las medidas del primer barrido. El cambio de signo de la transitoria laser, en el segundo barrido de potencial, tuvo lugar a potenciales mayores (hasta una diferencia de 500mV) (Figura A3. Por tanto se podría decir que en Pt(111)|[Emmim][Tf₂N] no se puede definir un valor fijo de *pme*. La respuesta laser presentó un comportamiento de histéresis respecto a la dirección en que se cambiaba el potencial aplicado. Este experimento demostró que la interfase Pt(111)|[Emmim][Tf₂N] es muy diferente a la de Pt(111)|disolución acuosa. En RTIL, las interacciones ion-ion así como ion-sustrato deben ser consideradas ya que están afectando a la reestructuración de la doble capa, que es más lenta en RTIL que en medio acuoso.

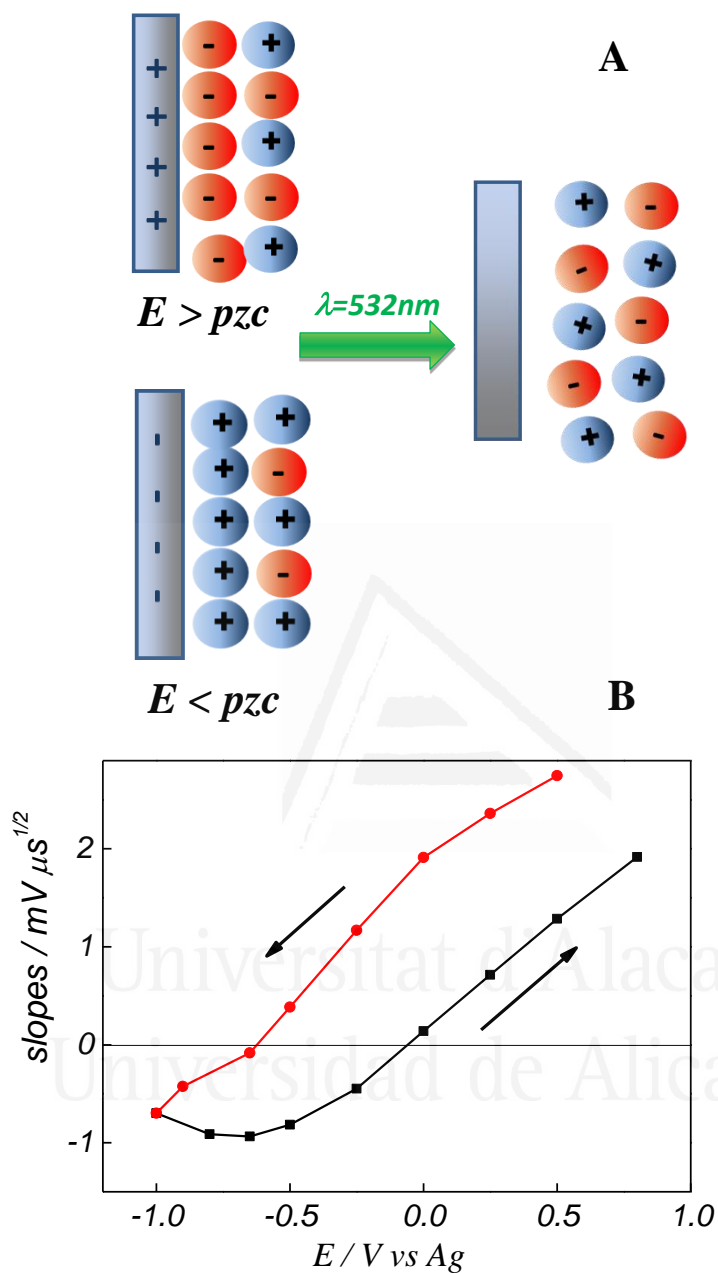


Figura A3: A) Esquema de la interfase Pt(111)/[Emmim][Tf₂N] antes y después de la perturbación laser. B) representación de las pendientes de ΔE vs $t^{1/2}$ obtenidos a partir de la linearización de los transitorios laser a distintos potenciales aplicados. Las flechas indican la dirección en la que se aplica potencial.

PUBLICACIÓN D (chapter 4, section 4.4): Characterization of the interfaces between Au(hkl) single crystal basal plane electrodes and [Emmim][Tf₂N] ionic liquid.

Este trabajo es una continuación del anterior. Se ha estudiado la interfase Au(hkl)[Emmim][Tf₂N] con voltametría cíclica y laser pulsante. Por primera vez, se observó que la respuesta voltamétrica de un RTIL es sensible a la orientación superficial. Los perfiles voltamétricos del Au(111), Au(100) y Au(110) en contacto con [Emmim][Tf₂N] muestran una región pseudo-capacitiva con grupos de picos o “spikes” superimpuestos, característicos de cada una de las orientaciones. Estos “spikes” se han atribuido a transiciones de fase que involucrarían tanto al anión como al catión (Figura A4). En el caso del Au(100) y Au(110) estos “spikes” apenas se desplazan con los límites de potencial, mientras que para el Au(111) la interfase Au(111)[Emmim][Tf₂N] es bastante más dinámica, y el grupo de picos característicos se desplazan en función de los límites de potencial. Este desplazamiento de los picos voltamétricos con el potencial puede estar relacionado con el fenómeno de la reconstrucción en Au(111), es decir la adsorción de aniones eliminaría la estructura reconstruida del Au(111) (3x√22). Otra posibilidad es que el desplazamiento de picos podría estar relacionada con cambios en la reestructuración de la doble capa.

Paralelamente al estudio voltamétrico, se analizó la interfase Au(hkl)[Emmim][Tf₂N] con láser pulsante. La respuesta laser presentaba una histéresis inferior al cambio de la dirección de potencial que en Pt(111), revelando la menor afinidad o adsorción de la especie del RTIL en Au que en Pt. Para realizar las medidas en un amplio rango de potencial minimizando efectos de reestructuración de la doble capa en el RTIL, el electrodo se pre-trató a la llama en cada medida laser. Se observó que el potencial al cual los transitorios laser cambiaban de signo (es decir, el valor del *pme* en medio RTIL), seguía el orden: Au(111)>Au(100)>Au(110). Este resultado está de acuerdo con el orden de las funciones de trabajo de los Au(hkl). Sin embargo, las diferencias entre los *pme* en [Emmim][Tf₂N] y las funciones de trabajo pueden variar debido a la influencia del RTIL en la distribución de carga en el electrodo. En conclusión, en este trabajo se pudo demostrar con voltametría cíclica y laser pulsante, que un RTIL es sensible a la orientación superficial del sustrato.

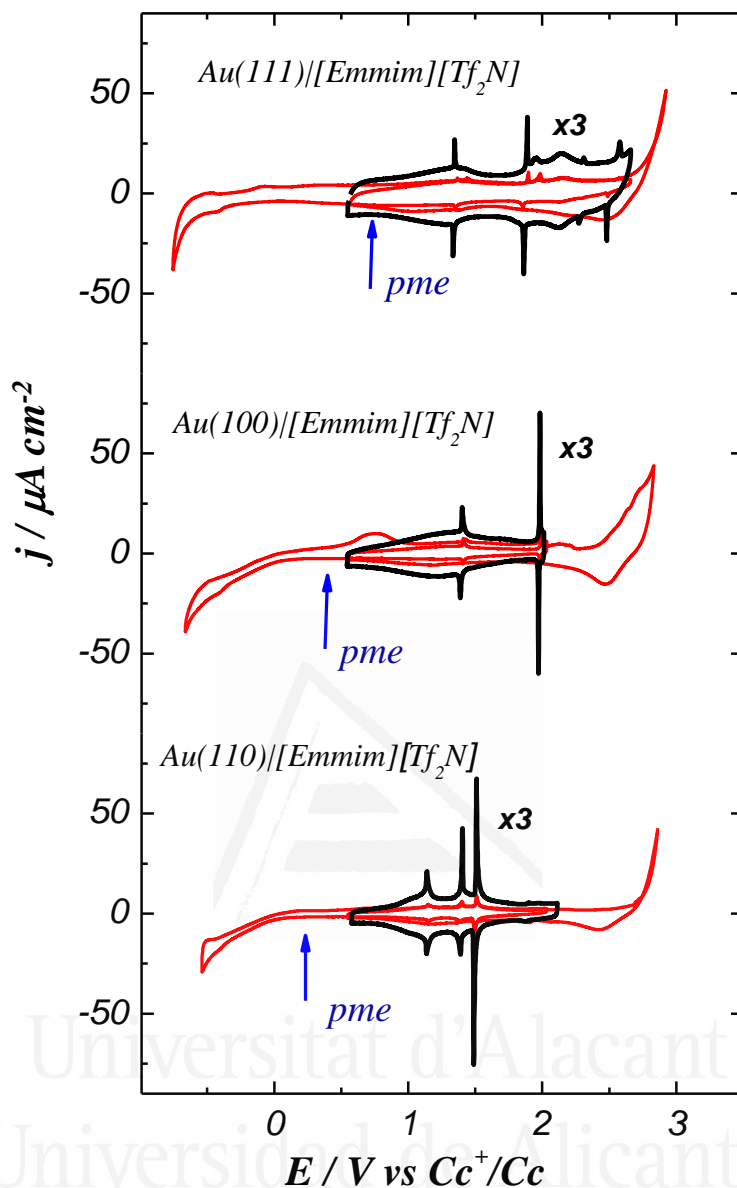


Figura A4: Voltametrías cíclicas de Au(hkl)[[Emmim]][Tf₂N] a 50mV/s y posición del pme.

PUBLICACIÓN E (chapter 4, section 4.5): Copper underpotential deposition at gold surfaces in contact with a deep eutectic solvent: New insights.

En este trabajo se investigó la interfase Au(poly)|DES y Au(hkl)|DES por voltametría cíclica. En este trabajo, el objetivo es investigar la interfase Au(hkl)|DES y analizar si la respuesta del DES también es sensible a la orientación superficial. En él, se verificó que el perfil voltamétrico del blanco Au(111)|DES y Au(100)|DES es también

sensible a la superficie y presenta una serie de picos quasi-reversibles característico de cada uno de los monocristales (Figura A4). El perfil voltamétrico es muy diferente al observado en otros electrolitos (acuoso y no acuoso) revelando la influencia de todas las especies del DES y no solamente del cloruro. La interfase Au(111)|DES es menos dinámica que la de Au(111)|[Emmim][Tf₂N], los picos voltamétricos apenas se desplazan con distintos límites de potencial. Este hecho reflejó la distinta naturaleza de la doble capa o región interfacial entre [Emmim][Tf₂N] y en DES, respectivamente. En DES, la reestructuración de las especies al salto de potencial podría ser más rápida.

A continuación, se analizaron las primeras etapas de depósito de Cu en Au(hkl) y en DES. El objetivo de esta parte es analizar el depósito de Cu sobre un sustrato metálico. Se observó que el depósito de Cu en los monocristales de Au implica la formación de una monocapa UPD (underpotential deposition) como etapa previa que precede el depósito “bulk”. El perfil voltamétrico de la UPD de Cu en ambos monocristales es muy semejante al que se obtiene en medio acuoso en presencia de cloruros, lo que implica que el depósito UPD de Cu en DES está más influenciado por la elevada concentración de cloruros en DES, los cuales, probablemente, co-adsorben con el Cu. Sin embargo, la separación de grupo de picos en la ventana de potencial es mayor en DES que en medio acuoso, evidenciando la influencia del resto de especies de DES en el depósito de Cu en Au(hkl) (Figura A5).

Universitat d'Alacant
Universidad de Alicante

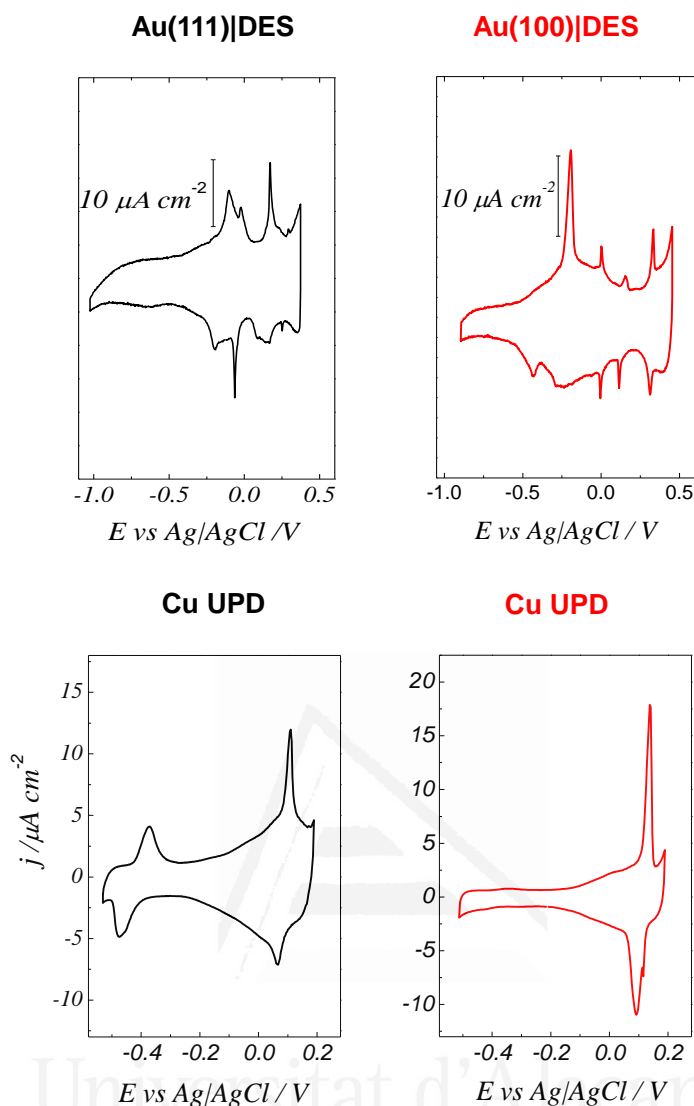


Figura A5: Voltametrías cíclicas de los blancos Au(111)|DES y Au(100)|DES a 50mV/s , y Cu(I) UPD en ambos monocristales a 5mV/s .

PUBLICACIÓN F (chapter 4, section 4.6): Copper electrodeposition in a deep eutectic solvent. First stages analysis considering Cu(I) stabilization in chloride.

El objetivo de esta publicación fue buscar una estrategia que permita analizar las primeras etapas del mecanismo de depósito electroquímico de cobre sobre carbono vítreo en distintos electrolitos: en medio acuoso en ausencia y presencia de cloruros, y en DES. Se analizó tanto las primeras etapas de depósito de Cu(I) como de Cu(II). En presencia de agente complejante, cloruro, el depósito de Cu(II) tiene lugar en dos etapas que están separadas en la escala de potencial. La primera etapa involucra la reducción de Cu(II) a

Cu(I), que es una reacción de esfera externa reversible, o cuasi-reversible en DES. La especie de Cu(I) está estabilizada en el medio por formación del complejo con cloruro. En medio acuoso, ambas etapas están solapadas, debido a que el intermedio de Cu(I) no está estabilizado. En medio acuoso cloruro y en DES, aplicando sobrepotenciales más negativos, el complejo de cloruro de Cu(I) deposita a Cu(0). En el caso del DES, la mayor viscosidad del medio supone aplicar mayores sobrepotenciales para depositar Cu.

Para el análisis de las primeras etapas de depósito metálico, se registraron cronoamperometrías $j-t$ a distintos potenciales aplicados, y después se ajustaron a los modelos clásicos de nucleación y crecimiento formulados por Scharifker y Hills. Para un análisis coherente de las transitorias $j-t$, se planteó una estrategia que permite separar la contribución de la primera etapa de Cu(II)-Cu(I) del depósito de cobre. Para ello se aplicó un programa de doble salto potencioestático. Primero, se registró una cronoamperometría a un potencial en el que el complejo Cu(I)-Cl_x es estable, el tiempo suficiente hasta que la corriente disminuyó por difusión lineal y alcanzó un valor estacionario. A continuación, se saltó a un potencial donde el Cu(I) depositaba a Cu(0). Las cronoamperometrías registradas para el depósito de Cu(I)-Cu(0) mostraban el perfil típico de un metal que nuclea y crece según un proceso 3D controlado por difusión. El ajuste de las cronoamperometrías a las ecuaciones adimensionales de S-H mostraron resultados coherentes con el ajuste previo en disolución acuosa de cloruro. Estos experimentos demostraron que la estrategia de doble pulso potencioestático es útil para el análisis de las primeras etapas de formación de depósito electroquímico de un metal divalente como Cu(II), si la transferencia de ambos electrones está separada en la escala de potencial. El mecanismo de nucleación y crecimiento tiende a ser instantáneo al aplicar sobrepotenciales suficientemente altos. Sin embargo, son necesarios mayores sobrepotenciales en DES para apreciar cambios sustanciales en el mecanismo de formación de depósito.

La morfología de los depósitos obtenidos en cada disolución por FE-SEM mostró que, en medio acuoso en ausencia de cloruros (percloratos), se formaban clusters de tamaño parecido, reforzando la idea de nucleación instantánea en las primeras etapas. En DES y en medio cloruro la morfología típica era la de forma de “flor”, debido a la mayor agregación de las partículas y a la difusión superficial. Sin embargo, aunque en DES y medio acuoso clorurado el cobre desarrolló la misma morfología, en DES el tamaño de clúster era considerablemente más pequeño, hecho que se atribuyó a la mayor viscosidad

del medio y, por tanto, menor difusión superficial (Figura A6). En conclusión, en DES, la formación del depósito de Cu es más lenta, se necesitan aplicar sobrepotenciales más elevados y el tamaño de partícula es más fino.

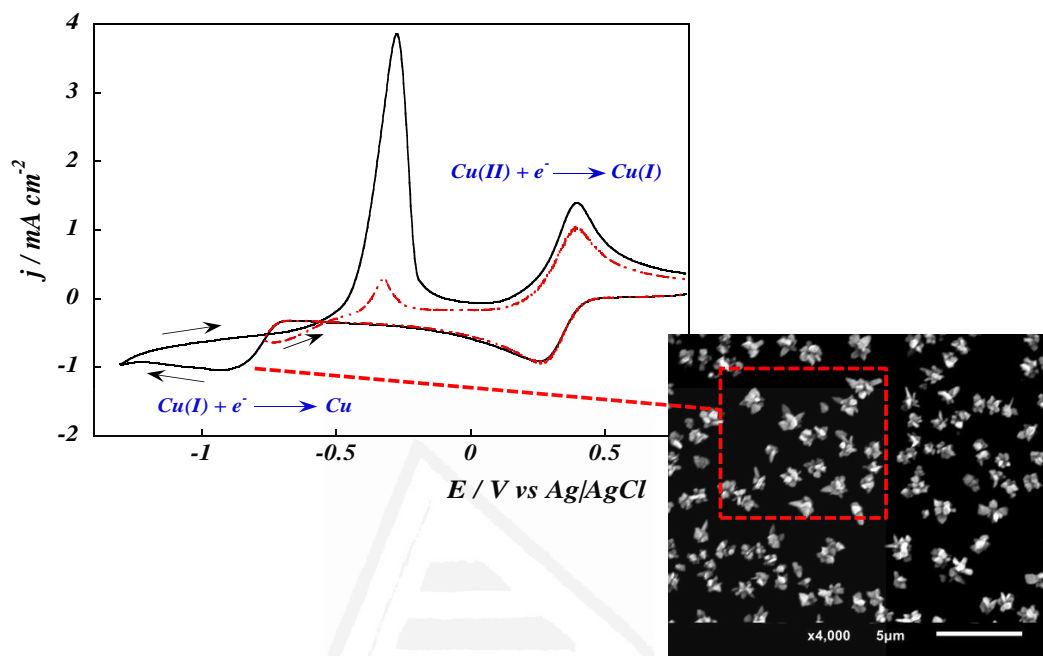


Figura A6: Voltametría cíclica del depósito de Cu(II) en carbono vítreo y DES (70°C) a 50 mV/s y distintos límites de potencial. La línea roja y punteada muestra el bucle de nucleación y crecimiento. A la derecha, imagen SEM del correspondiente depósito de cobre a sobrepotencial moderado.

PUBLICACIÓN G (chapter 4, section 4.7): *Advances in Copper Electrodeposition in Chloride Excess. A Theoretical and Experimental Approach.*

El objetivo de este trabajo es profundizar más en el análisis mecanístico de las primeras etapas de formación del depósito de Cu en DES en medio acuoso con exceso de cloruros. Como se comentó en la sección anterior, en presencia de un agente complejante como cloruros, el depósito de Cu(II) a Cu(0) tiene lugar en dos etapas de transferencia electrónica bien separadas en la escala de potencial, debido a la estabilización del intermedio Cu(I)-Cl_x . La idea de este trabajo es plantear un modelo matemático que permita obtener los valores de las variables necesarias para el análisis de las primeras

etapas de depósito. Para ello, y aplicando el método de doble salto potenciostático, se registraron cronoamperometrías a distintos potenciales aplicados con el objetivo de analizar por separado cada una de las etapas de transferencia electrónica: de Cu(II) a Cu(I) y luego de Cu(I)-Cu(0).

La transferencia del primer electrón: Cu(II)-Cu(I) es una etapa controlada por difusión. Planteando las ecuaciones de transporte de materia y las condiciones límite, es posible calcular las concentraciones en superficie de Cu(II), Cu(I) libre y Cu(I) complejo en cada instante. Se observó que, a partir de un tiempo determinado, los valores de concentraciones para cada una de las especies de Cu(I) alcanzaban un valor estacionario, instante de tiempo en el que se podría saltar al potencial donde el depósito de Cu (Cu(I)-Cu(0)) tenía lugar (Figura A7).

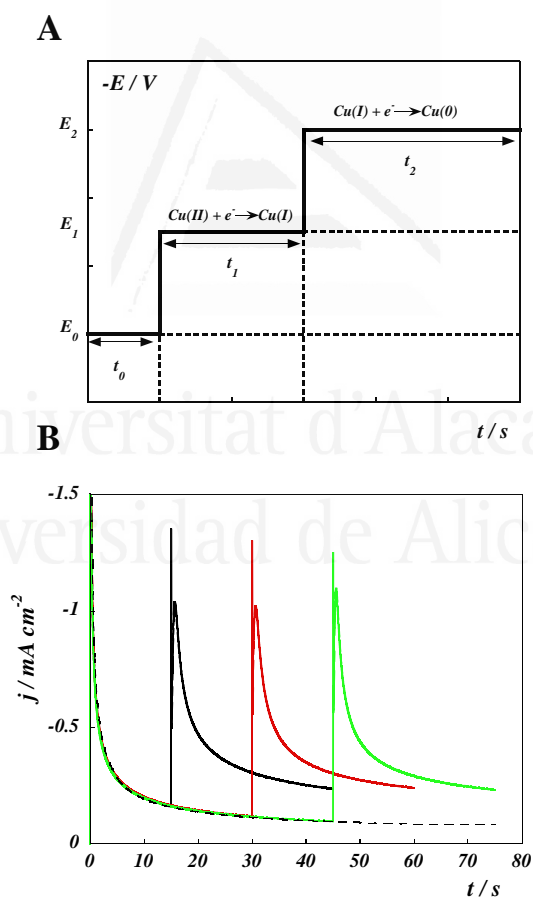


Figura A7: Esquema de la señal de doble salto potenciostático. B) Transitorias $j-t$ del depósito de Cu en DES a 40°C : $E_1 = -0.1\text{V}$ y distintos tiempos y $E_2 = -1.05\text{V}$ vs Ag/AgC.

A partir de las cronoamperometrías registradas para el depósito de Cu se extrajeron los valores del máximo de corriente (j_m, t_m). El modelo matemático de S-H proporciona una expresión matemática que relaciona variables como la concentración de reactante y coeficiente de difusión con otras variables termodinámicas que describen el proceso: esta expresión matemática es equivalente al producto: $j_m^2 t_m$. Para los casos límites de nucleación progresiva e instantánea, la teoría proporciona dos valores: $(j_m^2 t_m)_p$, límite progresivo; y $(j_m^2 t_m)_i$ límite instantáneo. Los valores $j_m^2 t_m$ calculados a partir de los datos experimentales (a partir de los máximos de las transitorias j vs t a distintos potenciales aplicados), deben estar comprendidos entre esos dos valores teóricos si hay coherencia con el modelo. Con el planteamiento matemático propuesto en este trabajo, y conociendo los excesos superficiales de Cu(I) para reducirse, se obtuvo una buena correlación entre los valores experimentales de $j_m^2 t_m$ y los teóricos en medio acuoso. En medio DES, aunque los valores experimentales de $j_m^2 t_m$ tenían el mismo orden de magnitud que los teóricos, sin embargo, eran ligeramente superiores en todos los potenciales aplicados. Esta discrepancia se atribuyó a que las concentraciones superficiales de Cu(I) en DES se subestimaron debido a que se utilizaron valores de potencial formal en el cálculo matemático, asociados a un medio acuoso con una concentración de cloruros próxima a la del DES. A pesar de esta discrepancia, con este trabajo se planteó un método de análisis matemático prometedor para estudiar el depósito de metales que involucran más de una etapa de transferencia electrónica, y que podría ser válida en medio no acuosos si se conocen las variables termodinámicas que definen dicho medio.

PUBLICACION H (chapter 4, section 4.8: Three-dimensional nucleation with diffusion controlled growth: A comparative study of electrochemical phase formation from aqueous and deep eutectic solvents.

En este trabajo se han reformulado los modelos teóricos clásicos de nucleación y crecimiento para calcular una serie de parámetros termodinámicos que permitan caracterizar el depósito metálico de un metal monovalente, el caso más sencillo de analizar. En este trabajo, concretamente se ha analizado el depósito de plata, en medio acuoso en presencia y ausencia de cloruros y en DES, para analizar de que forma el electrolito empleado afecta estos parámetros termodinámicos. Este metal deposita

siguiendo un mecanismo de nucleación y crecimiento en 3D. A partir del máximo en la curva j vs t (j_m , t_m) se extrajo información cinética del proceso: la constante de nucleación (A/s^{-1}) y la densidad de sitios activos o centros de nucleación (N_o/cm^2) a cada sobrepotencial aplicado (η). A partir de estos valores, y representado el logaritmo neperiano de la constante de nucleación (A) en función del valor de η al cual se realiza el depósito, se estimaron valores de: coeficiente de transferencia α , corriente de intercambio i_o , energía libre de Gibbs de nucleación $\Delta G(n_c)$ (para la formación núcleos estables) y tamaño crítico de núcleo n_c , entre otros parámetros. En el caso de la plata, se obtuvo que los valores de α son bastante menores a 0.5, sugiriendo que el estado de transición está mucho más próximo al del metal en disolución que al depositado, probablemente debido a la estabilización del complejo de plata con cloruros. Las corrientes de intercambio indicaron que el proceso de nucleación de Ag(I) era más lento en el siguiente orden: 0.6M NaClO₄ > 3M NaCl > DES, resultado por otro lado esperable y que refuerza el argumento de que en DES, los procesos de nucleación y crecimiento son más lentos, hecho que queda reflejado en el análisis morfológico de los depósitos de plata de trabajos anteriores. Un resultado, sin embargo, controvertido, son los valores de tamaño de núcleo crítico obtenidos, que en todos los casos fueron menores a 1 o 2, indicando que un núcleo estable podría estar formado a partir de un solo átomo. Este resultado indica que el proceso está activado (valores de $\Delta G(n_c)$ muy pequeños). Es importante tener en cuenta que estos modelos clásicos son aproximaciones sencillas cuya mayor limitación radica en que no consideran como el disolvente interactúa con el metal precursor o el sustrato, ni tampoco tiene en cuenta como se reestructura la doble capa a los potenciales en que se deposita, factores que influyen en el depósito metálico, especialmente si este se realiza en medio Líquido Iónico. De este trabajo se concluyó que la aproximación planteada aquí puede ser útil para el análisis del depósito de metales cuyo proceso está ralentizado, como es el caso del depósito en LI, aunque presente ciertas limitaciones al no considerar la influencia del solvente en el modelo.

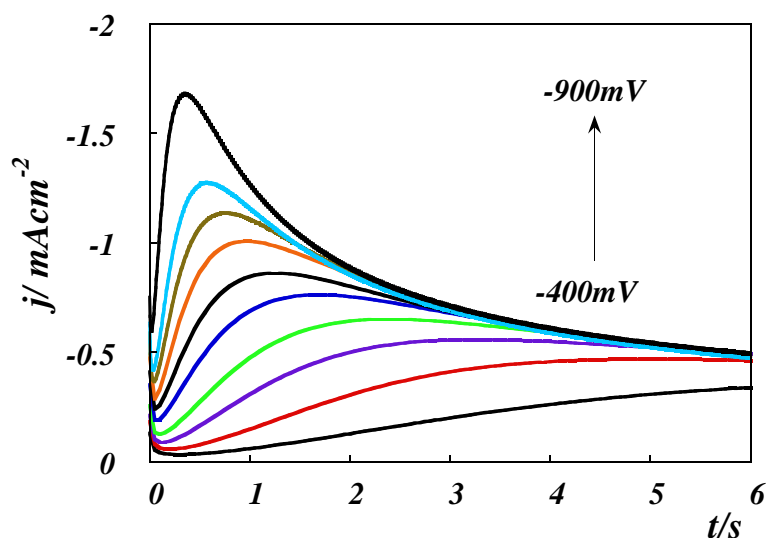


Figura A8: Transitorias $j-t$ para el depósito de Ag en carbono vítreo y en DES a 70°C , a distintos potenciales aplicados desde -400mV a -900V vs Ag/AgCl.

TRABAJO I (chapter 5, other works): *The use of CO as cleaning tool of highly active surfaces in contact with ionic liquids. Ni deposition on Pt(111) surfaces in IL media.*

En esta sección se ha tratado de buscar una metodología que permitiera pre-tratar y caracterizar un electrodo de Pt monocristalino: Pt(111), en contacto con [Emmim][Tf₂N] y con DES. Esta estrategia debe permitir, posteriormente, modificar dichos monocristales de Pt con otros metales, por ejemplo, Ni, mediante la técnica de electrodeposición metálica en LI. La estrategia que se utilizó para pre-tratar el Pt(111) fue utilizar monóxido de carbono (CO). Primero, el electrodo fue sometido al tratamiento térmico a la llama y a continuación se enfrió en atmosfera de monóxido de carbono el tiempo suficiente, hasta que la superficie quedo totalmente recubierta por una monocapa protectora de CO. Después, la monocapa de CO se eliminó potencioestáticamente en el mismo LI. En [Emmim][Tf₂N] (contenido de agua < 10ppm) se observó un pico afilado a potenciales cerca de la oxidación del disolvente y que correspondió a la oxidación de CO a CO₂. A pesar del contenido tan bajo en agua, la oxidación de CO en [Emmim][Tf₂N] tiene lugar a partir de la pequeña cantidad de agua presente en el medio. La carga involucrada en el proceso fue aproximadamente el doble del valor teórico para oxidación de una monocapa de CO, lo que sugirió dos posibilidades: adsorción de aniones al mismo

tiempo que se oxidaba el CO, o solapamiento del “stripping” de CO con la oxidación del disolvente.

Cuando la reacción de oxidación de CO se llevó a cabo en DES, (1% de agua en DES), esta reacción solapó con la oxidación del disolvente. Sin embargo, en la región de doble capa, un par cuasi-reversible de picos afilados aparecieron. Estos picos evolucionaban con sucesivos barridos cíclicos entre dos límites de potencial, hasta que finalmente desaparecieron y dejaron entrever el perfil voltamétrico del blanco Pt(111)|DES. Estos picos se atribuyeron a una transición orden desorden del CO en Pt(111) estabilizado en el medio. Estos resultados mostraron una reactividad muy diferente para la reacción de CO en Pt(111) dependiendo de la naturaleza del líquido iónico (Figura A9).

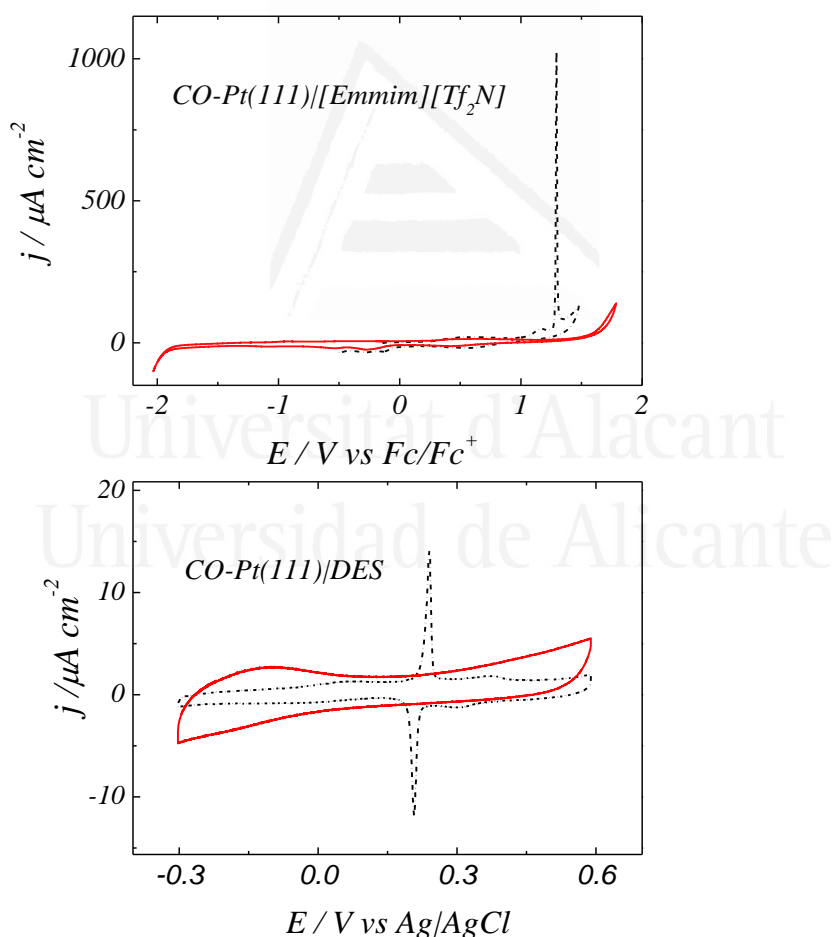


Figura A9: Voltametrías cíclicas de las superficies de CO-Pt(111)|[Emmim][Tf₂N] y CO-Pt(111)|DES a 20mV/s (línea punteada). La línea roja sólida corresponde al blanco voltamétrico (sin CO) en cada LI a 20mV/s.

A continuación, se depositó Ni en cada uno de los LIs. Mientras que la ventana de potencial en [Emmim][Tf₂N] fue suficiente para llevar a cabo el depósito de Ni en Pt(111) (3V), en DES existía solapamiento parcial con la reducción del DES. Además, el perfil voltamétrico de Pt(111)|DES mostró una serie de picos redox cerca de la reducción del LI que se atribuyó a la posible reacción de evolución de hidrogeno en DES (proton donor). En este LI, el depósito de Ni se llevó a cabo a potenciales bajos para evitar el solapamiento con la reducción del disolvente. La morfología del depósito de Ni en Pt(111) en ambos LI se analizó por FE-SEM, observándose que tamaño de nanocluster más pequeño se obtenía en [Emmim][Tf₂N] en lugar de en DES, es decir, se puede modular el crecimiento de Ni dependiendo del LI empleado. En conclusión, con este trabajo se demostró que el uso de CO es aplicable para tratamiento de los monocristales de Pt en LI, y que el depósito de Ni en Pt puede llevarse a cabo en ambos líquidos iónicos: [Emmim][Tf₂N] y DES.

PUBLICACIÓN J (chapter 4, section 4.9): Surface Sensitive Nickel deposition in Deep Eutectic Solvent.

Como en el anterior trabajo se demostró la viabilidad del DES para depositar Ni en Pt, en este trabajo se investigó, de forma más detallada, el depósito de Ni en DES sobre distintos sustratos: carbono vítreo y platino. Los objetivos de este trabajo son, por un lado, demostrar la viabilidad del DES para modificar un sustrato catalítico como Pt con un metal que es difícil de depositar en medio acuoso (el depósito de Ni solapa con la tirada de hidrógeno en medio acuoso); y, por otro lado, analizar la sensibilidad del proceso a la superficie. Para ello, en este estudio también se utilizó un monocristal de Pt: Pt(111).

En carbono vítreo, se observó que la ventana de potencial es suficientemente amplia y permite depositar Ni sin que interfiera la reducción del disolvente. A medida que la superficie de carbono vítreo es modificada con Ni, la ventana del disolvente disminuye en el límite catódico debido a que el Ni es más catalítico a la reducción del disolvente que el carbono vítreo. En cambio, la ventana de reducción sobre Pt es considerablemente menor y solapa con el depósito de Ni. A medida que el Ni deposita en Pt, la ventana se ensancha debido a que el Ni es menos catalítico a la reducción del solvente que el Pt. En ambos sustratos, el depósito de Ni a sobrepotenciales muy elevados genera distintas

especies de Ni hidroxiladas, tal como demostró el análisis XPS, causando la pasivación de la superficie. A sobrepotenciales moderados, distintas estructuras de Ni con distinta proporción de hidrogeno intersticial en la red se forman sobre Pt. Como demostró el análisis voltamétrico realizado en Pt(111), la formación de estructuras de Ni con mayor proporción de hidrógeno en la red están favorecidas a sobrepotenciales mayores. Este hecho se atribuyó al solapamiento del depósito de Ni con la HER del DES en Pt. En carbono vítreo, sin embargo, la formación de Ni hidrogenado no está favorecida debido al bajo poder catalítico del carbono vítreo a la evolución de hidrógeno.

El análisis del depósito de Ni por FE-SEM mostró que la morfología típica es la de nanoclusters de forma redondeada, de mayor tamaño en carbono vítreo, debido a una mayor difusión superficial. A sobrepotenciales moderados, se observó la presencia de agujeros de forma esférica en el sustrato de Pt, otra evidencia experimental de la posible evolución de hidrógeno en Pt.

Se investigó el mecanismo de formación de depósito electroquímico en carbono vítreo y en Pt(111), y se observó que en ambas superficies el depósito de Ni en DES sigue un mecanismo de nucleación y crecimiento en 3D controlado por difusión. En el caso de Pt(111), el enlace más favorecido entre Pt-Ni respecto de carbono vítreo sugirió la formación de varias monocapas de Ni sobre Pt que podrían preceder la nucleación y crecimiento.

Finalmente, se utilizó AFM (Atomic Force Microscopy) para analizar la influencia de la orientación del sustrato en el depósito de Ni en Pt(111), cuando se depositó pequeñas cantidades de Ni. A sobrepotenciales elevados, se observó la formación de nanopartículas esféricas de Ni sobre un sustrato de Pt(111) recubierto completamente de Ni. En cambio, a sobrepotenciales moderados, se observó la formación de agrupamientos triangulares de partículas, inducido por la orientación del sustrato, con depósito preferencial en los defectos de la superficie. Este experimento demostró la sensibilidad del proceso a la superficie.

En definitiva, se observó que el DES permitía modular el crecimiento de nanoestructuras de Ni en un sustrato altamente catalítico como Pt, abriendo la posibilidad de utilizar este LI para modificar Pt con nanoestructuras de otros metales que son difíciles de depositar en medio acuoso.

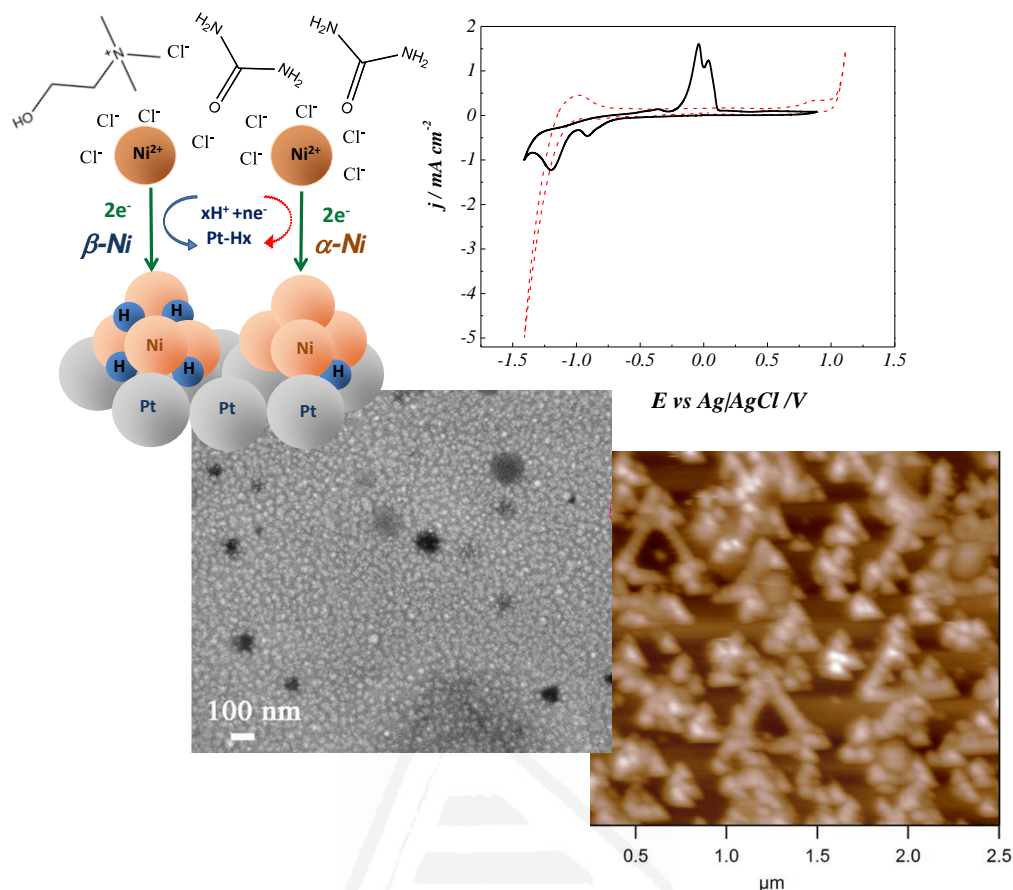


Figura A10: Voltametría cíclica del depósito de Ni en Pt(111) (línea negra) superpuesto con el blanco de Pt(111)/DES a 20mV/s. La imagen a la izquierda es un SEM del depósito de Ni a sobrepotencial alto-moderado, mostrando los agujeros debido a la formación de hidrógeno. A la derecha, el AFM del depósito a baja cobertura y sobrepotencial bajo, mostrando los agrupamientos triangulares. El esquema es una representación de la formación de distintas estructuras de Ni hidrogenadas.

C) CONCLUSIONES

En conclusión, esta tesis es un intento por describir o entender las propiedades que rigen la interfase Metal|Líquido iónico, y como estas puedan influir en el depósito metálico. A través del estudio de dos LI muy distintos pero representativos de sus respectivas familias, se muestra el potencial de estos solventes para modificar una superficie con distintos metales y de forma sencilla, a través de la técnica de formación de depósito electroquímico. Los resultados de esta tesis abren la posibilidad de utilizar estos novedosos solventes para el diseño de nuevos materiales.

ANOTHER PUBLICATIONS

- (1) **Sebastián, P.**; Vallés, E.; Gómez, E., *First stages of silver electrodeposition in a deep eutectic solvent. Comparative behavior in aqueous medium*. *Electrochimica Acta* **2013**, 112, 149-158.
- (2) Yang, J.; **Sebastian, P.**; Duca, M.; Hoogenboom, T.; Koper, M. T. M., *Ph dependence of the electroreduction of nitrate on Rh and Pt polycrystalline electrodes*. *Chemical Communications* **2014**, 50 (17), 2148-2151.
- (3) Martínez-Hincapié, R.; **Sebastián-Pascual, P.**; Climent, V.; Feliu, J. M., *Exploring the interfacial neutral ph region of Pt(111) electrodes*. *Electrochemistry Communications* **2015**, 58, 62-64.
- (4) Ledezma-Yanez, I.; Wallace, W. D. Z.; **Sebastián-Pascual, P.**; Climent, V.; Feliu, J. M.; Koper, M. T. M., *Interfacial water reorganization as a ph-dependent descriptor of the hydrogen evolution rate on platinum electrodes*. *Nature Energy* **2017**, 2 (4).
- (5) Schäfer, P.; Lalitha, A.; **Sebastian, P.**; Meena, S. K.; Feliu, J.; Sulpizi, M.; van der Veen, M. A.; Domke, K. F., *Trimesic acid on cu in ethanol: Potential-dependent transition from 2-d adsorbate to 3-d metal-organic framework*. *Journal of Electroanalytical Chemistry* **2017**, 793, 226-234.
- (6) Martínez-Hincapié, R.; **Sebastián-Pascual, P.**; Climent, V.; Feliu, J. M., *Investigating interfacial parameters with platinum single crystal electrodes*. *Russian Journal of Electrochemistry* **2017**, 53 (3), 227-236.
- (7) **Sebastián, P***; Climent, V.; Feliu, J. M.; Gómez, E., *Ionic liquids in the field of metal electrodeposition*. In Reference module in chemistry, molecular sciences and chemical engineering, Elsevier: 2017. DOI: 10.1016/B978-0-12-409547-2.13379-7.
- (8) Gonzalez-Aribas, E.; Falk, M.; Aleksejeva, O.; Bushnev, S.; **Sebastián, P.**; Feliu, J.M.; Shleev, S.; *Conventional symmetric biosupercapacitor based on rusticyanin modified gold electrodes*. *Journal of Electroanalytical Chemistry* **2018**, DOI: 10.1016/j.jelechem.2018.03.060.
- (9) Galindo, M.; **Sebastián, P.**; Cojocar, P.; Gómez, E., *Electrodeposition of aluminium from hydrophobic perfluoro-3-oxa-4,5 dichloro-pentan-sulphonate based ionic liquids*. *Journal of Electroanalytical Chemistry* **2018**, DOI: 10.1016/j.jelechem.2018.04.066.